High Temperature Polymer Electrolyte Membrane Fuel Cells - Performance and Durability Studies

Celenk, Sanser

Publication date:
2023

Document Version
Publisher's PDF, also known as Version of record

High Temperature Polymer Electrolyte Membrane Fuel Cells

- Performance and Durability Studies

Sanser Celenk

PhD Thesis

April 2023

Department of Energy Conversion and Storage

Technical University of Denmark

High Temperature Polymer Electrolyte Membrane Fuel Cells

- Performance and Durability Studies

Sanser Celenk

Principal supervisor: Professor Qingfeng Li, DTU Energy

Co-supervisor: Professor Jens Oluf Jensen, DTU Energy

Dr. Lars Nilausen Cleemann, Blue World Technologies

Section of Low Temperature Electrochemistry

Department of Energy Conversion and Storage

Technical University of Denmark

Fysikvej Building 310

2800 Kgs. Lyngby, Denmark

www.energy.dtu.dk

Preface and Acknowledgements

This thesis is submitted in candidacy for a Ph.D. degree from the Technical University of Denmark (DTU). The work herein was conducted over 3.5 years running from December 2019 to April 2023 at the Section for Low Temperature Electrochemistry at the Department of Energy Conversion and Storage (DTU Energy). The studies have been supervised by Professor Qingfeng Li, Professor Jens Oluf Jensen, and Dr. Lars Nilausen Cleemann. The PhD project was funded by the Energy Technology Development and Demonstration (EUDP) Program (COBRA-Drive, 64018-0118), Denmark.

Looking back to my way of last six years, I remember working on my graduation project during my bachelor study that involved modeling polymer electrolyte membrane fuel cells using computational fluid dynamics. Today I am in the process of submitting my Ph.D. thesis on the same topic. Call it coincidence, fate or determination, I can honestly say, it was mostly luck that my path is crossed with some people.

It has been fortunate for me to have an incredible team of supervisors. I would like to express my deep gratitude towards my main supervisor, professor Qingfeng Li. Apart from being a great academic supervisor, I am indebted him for his understanding, support and the care during the entire period of my ph.d. project, especially the last few months. I would like to thank professor Jens Oluf Jensen for his encouragement and all discussions, which sometimes last for hours.

Dr. Lars Nilausen Cleemann initialized my project at DTU and continued his guidance and support to my project after he moved to Blue World Technologies. Dr. Hans Aage Hjuler and colleagues at Blue World Technologies have hosted my visit and inspired my research. They have kindly provided MEAs of high temperature polymer fuel cells that I have tested through this project.

I am grateful to have wonderful colleagues. I appreciate Dr. Benedikt Axel Brandes and Dr. Mikkel Rykær Kraglund for their efforts to make the lab a wonderful workplace. During those three years, I have spent significant time on commissioning the fuel cell testing experimental facilities. I thank research technicians Jens Borchsenius, Jimmy Cali Hansen and Anders Vang for their always availability and all kind of help. My special thanks goes to Axel Boisen, who has spent lots of weekends with me in the laboratory.

Dr Pradipkumar Leuaa is thanked for lending me the Biologic booster when the equipment I was using was brutally murdered. I am thankful to laboratory technicians Larisa Seerup and Chao Pan for helping me for the SEM images. A special thanks also goes to my officemates Yun Xie and Dr. Amado Andrés Velázquez-Palenzuela for sharing everything.

I would like to thank the COBRA-Drive project partners, Dr. Søren Primdahl, Dr. Søren Juhl Andreasen and Dr. Samuel Simon Araya, who has created super collaborative atmosphere and made the project a great success, even though the project communication was sometime hampered during the pandemic period.

My undergraduate supervisor, Professor Mustafa Zeki Yılmazoğlu from Gazi University has my gratitude. He is the person who made me aware of the excellence of DTU and the place to pursuit my study.

Last but not least, I warmly thank my friends and family for the daily conversations and the support on the personal level.

Abstract

High temperature proton exchange membrane fuel cells based on phosphoric acid doped polybenzimidazole membranes are a technology featured by simplified construction and operation with possible integration with e.g. methanol reformers. Further improvement of the performance and durability is a key to promote the technology. The present thesis addresses these challenges by focusing on the anode performance in the presence of fuel impurities e.g. CO and catalyst degradation during dynamic potential cycling.

The small poisoning effect by up to 2% CO in pure hydrogen is verified with electrodes of high Pt loading, ca. 12 mV at 0.2 A/cm^2. This is however increased to 24 mV for electrodes of 0.3 mgPt/cm^2 and to 63 mV for electrodes of 0.15 mgPt/cm^2 . On the other hand, the hydrogen dilution by an inert gas (e.g. N_2 or Ar) in the absence of CO is found to deteriorate the anode performance. Switching from 100% to 60%H_2 leads to a lowered performance by ca. 25 – 30 mV for electrodes of Pt loadings from 0.15 to 1.3 mgPt/cm^2.

When CO is present in the diluted hydrogen steam, the combined effects of the hydrogen dilution and CO poisoning becomes substantially high especially for low Pt loading electrodes. For anodes of 0.3 $mg_{Pt}cm^{-2}$, 2.0% CO in a 40% H_2 fuel stream results in an anode voltage loss by 130 mV. This combined effect is well correlated to the ratio [CO]/[H_2], which in turn determines the Pt surface coverage by CO and hence the fraction of the active sites available for the hydrogen oxidation. A strong dependence of the anode performance loss on the [CO]/[H_2] ratio is found to be in an exponential form, which is highly related to the Pt loading of the electrode.

The hydrogen oxidation and evolution reaction kinetics is of fundamental as well as practical significance in the presence of CO, and has been studied in acidic electrolytes at temperatures of up to 80ºC. The study is extended to temperatures of up to 180 ºC in the absence and presence of carbon monoxide using acid doped polybenzimidazole electrolytes. The study is made by means of a hydrogen pumping cell with gas diffusion electrodes of ultralow Pt loadings of 1.5-6.5 μgPt/cm^2. The ultralow Pt loading allows for minimizing the mass transport and eliminating the ohmic resistance contributions to the kinetic behaviors. Fitting with the Butler–Volmer equation obtains an HOR/HER exchange current density of 200 to 500 mA/cm^2 based on the electrochemically active surface area

of platinum. These numbers are comparable to those obtained at 40-80^{o}C in perfluorosulfonic acid electrolytes. The activation energy in a temperature range from 120 to 180^{o}C is found to 49.6 kJ/mol. It is shown that the HOR, but not HER, rate is limited by the Tafel step.

In the presence of CO severely asymmetric Tafel plots for HER/HOR are observed. The strong adsorption of CO on the Pt surface hampers the HOR kinetics by further limiting the slow dissociative hydrogen adsorption. At an overpotential of 0.1 V, the HOR kinetic current density was decreased from 600 mA/cm^2 for pure hydrogen to 2.9 mA/cm^2 at the CO concentration of 0.25%. In term of exchange current densities of HOR the presence of CO at a concentration of 0.25-2.0% results in a decrease of i^o by about 2 orders of magnitude.

The performance degradation of HT-PEMFC technology is studied by potential cycling at 160oC. The membrane-electrode-assemblies are made of acid-doped polybenzimidazole membranes and PtCox catalysts on the cathode. While the upper potential limit is fixed at 0.95 V the degradation is stressed by varying the low-end potential from 0.8 to 0.65 V and hold duration from 5 to 60 sec. During the cycling tests, little degradation of the membrane, in terms of ohmic resistance and open circuit voltage is observed. A significant performance loss is attributable to the mass transport due to the degradation of electrode hydrophobicity. A major catalyst degradation mechanism is the platinum particle growth via the electrochemical Ostwald ripening. No evidence of the cathode dealloying was detected during the potential cycling. The dissolution of platinum or the surface oxides of platinum during the upper potential hold at 0.95 V is limited by the available acid in the PBI membrane. The low-end potential and the hold duration seem critical where the reduction and re-deposition of platinum occur, leading to formation of larger particles and hence loss of the active surface area.

Popular Scientific Summary

Clean energies based on renewable resources are the ultimate solution to the ever-growing concern of global warming and subsequent climate changes due to industrial combustion of fossil fuels. Green hydrogen as an energy carrier in the future energy systems has been developed for storage and conversion of renewable energies by means of electrolysers and fuel cells. Polymer electrolyte membrane fuel cells are a technology potentially for automobile, portable and stationary applications. A variant type of the technology can operates at temperatures around 160 ^{o}C with a simplified system based on methanol reformat fuels. Danish industry is committed to establish production of components, stacks and systems to accelerate sustainable transportation by developing the first-generation range extender for medium to heavy duty vehicles. This project is devoted to characterization of the core components of this type of fuel cells including impacts of fuel impurities from methanol reforming on cell performance, electrode kinetics as well as the dynamic operation with on the cell degradation. A close correlation of the fuel impurity effect is found with development of low metal loading electrodes, suggesting that the feasibility of the new electrodes should be assessed under scenarios of utilizing reformat fuels. Kinetic rates of the hydrogen oxidation in the presence of carbon monoxide impurities are found to be two orders of magnitude lower. In addition the catalyst degradation under the potential cycling via the metal dissolution-redeposition mechanism is found to be limited by the electrolyte inventory of the membrane

Publicatio ns and manuscripts during the PhD study

Three manuscripts included in the thesis

1) CO Poisoning in High Temperature Polymer Electrolyte Membrane Fuel Cells Operating with Diluted Hydrogen and Low Pt Loadings
   Sanser Celenk, Santiago Martin, Lars N. Cleemann, Qingfeng Li and Jens Oluf Jensen
2) Hydrogen Oxidation and Evolution Kinetics in the Absence and Presence of Carbon Monoxide for High Temperature Polymer Electrolyte Membrane Fuel Cells
   Sanser Celenk, Lars N. Cleemann, Jens Oluf Jensen and Qingfeng Li
3) Potential Cycling Test of High Temperature PEMFC Based on Acid Doped Polybenzimidazole Membranes
   Sanser Celenk, Lars N. Cleemann, Jens Oluf Jensen, and Qingfeng Li

Other publications not included in the thesis

1) N. Seselj, D. Aili, S. Celenk, L. N. Cleemann, H. A. Hjuler, J.O. Jensen, K. Azizi and Q. Li, CSR review, in press (2023)
2) H. A. Hjuler, K. Azizi, N. Seselj, S. Martinez Alfaro, H. R. Garcia, D. Gromadskyi, L. Hromadska, S. Primdahl, J. O. Jensen, Q. Li, S. Celenk and L. Cleemann, *ECS Trans*, 2021, 104, 403–413.

List of Abbreviations

ADL – Acid doping level

AFC – Alkaline fuel cell

ASR – Area specific resistance

AST – Accelerated stress test

BOL – Beginning of life

CL – Catalyst layer

DMAc – Dimethylacetamide

DMFC – Direct methanol fuel cell

DTA – Differential thermal analysis

ECSA – Electrochemical active surface area

EIS – Electrochemical impedance spectroscopy

EOL – End of life

GDL – Gas diffusion layer

HER – Hydrogen evolution reaction

HOR – Hydrogen oxidation reaction

HT-PEMFC – High temperature polymer electrolyte fuel cell

LT-PEMFC – Low temperature polymer electrolyte fuel cell

MCFC – Molten carbonate fuel cell

MEA – Membrane electrode assembly

MPL – Microporous layer

OCV – Open circuit voltage

ORR – Oxygen reduction reaction

PAFC – Phosphoric acid fuel cell

PA – Phosphoric acid

PBI – Polybenzimidazole

PEM – Polymer electrolyte membrane

PEMFC – Proton electrolyte membrane fuel cell

PFSA – dsa

POL – Peak of life

PPA – Polyphosphoric acid

PRU – Polymer repeating unit

PTFE –Polytetrafluoroethylene

RDE – Rotating disk electrode

RH – Relative humidity

SOA – State of art

SOFC – Solid oxide fuel cell

TPB – Three phase boundary

Contents

1. INTRODUCTION

1.1 Hydrogen and fuel cells

Energy consumption and climate change due to uses of fossil fuels are of global concern, which have stimulated worldwide research on clean, efficient, and sustainable energy technologies. Replacement of fossil fuels by clean energy resources such as bioenergy, wind and solar energy would be the long-term solution. Hydrogen and its combination with electrochemical energy conversion devices i.e. fuel cells and electrolysers, have the potential to provide a reliable, secure and clean energy technology.

Fuel cell is an electrochemical device that directly converts chemical energy from fuels (e.g. hydrogen) into electricity. It is an ideal device in terms of the high energy conversion efficiency and little release of air pollutants other than the by-product of water, compared to the present fossil fuel based power technologies for both stationary power plants and automobile applications. It is also environmentally sustainable by assuming that hydrogen as an energy carrier is potentially produced from the renewable electricity.

1.2 Principle and types of fuel cells

A fuel cell consists of a fuel electrode (anode or negative electrode), an oxidant electrode (cathode or positive electrode), separated by an ion-conducting electrolyte, as schematically represented in Figure 1.1 where a proton conducting membrane is used as electrolyte.

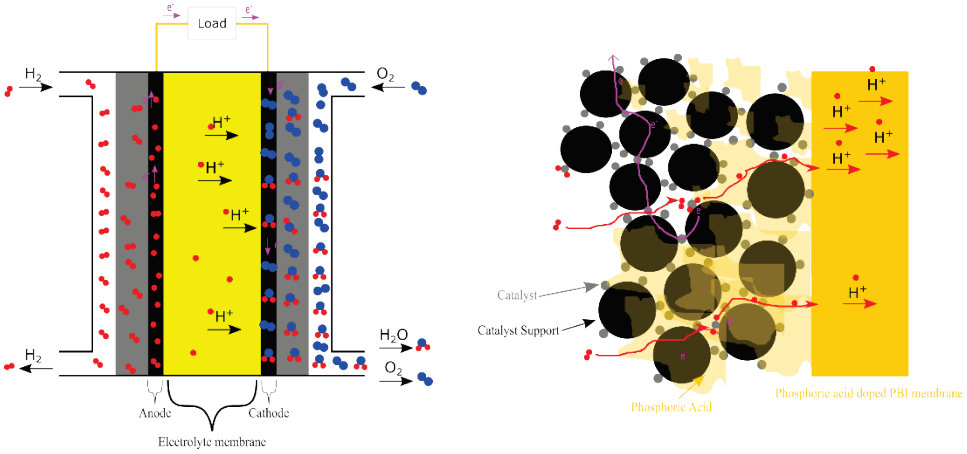

Figure 1.1 Schematic of a proton exchange membrane fuel cells. The inset is the electrode structure at the interface with membrane.

The fuel and oxidant are introduced to the cell via gas flow channels, followed by transport through the gas diffusion layers toward catalysts. No mixing of the fuel (e.g. H_2) at the anodic side and oxygen at the cathodic side occurs owing to the separation by the electrolyte. At the anode the hydrogen oxidation reaction (HOR) takes place with help of the catalysts, giving protons and electrons.

Anodic: $H_2 \rightarrow 2H^+ + 2e^-$ $E^0_{anode} = 0$ (1.1)

The electrolyte is a non-electronic conductor. Electrons produced at the anode flow to the cathode via an external circuit while protons pass through the electrolyte directly from the anode to the cathode, where oxygen reacts with the incoming electrons and protons to produce water, the so-called oxygen reduction reaction (ORR):

Cathodic : $\frac{1}{2} O_2 + 2\ e^- + 2\ H^+ \rightarrow H_2O$ $E^0_{cathode} = 1.23$ V (1.2)

The overall reaction of the fuel cell is the sum of the anode and cathode reactions, i.e. the combination of hydrogen and oxygen to produce water:

Overall: $2\ H_2 + O_2 \rightarrow 2\ H_2O$ $E^0_{cell} = 1.23$ V (1.3)

Gas diffusion layers are made on woven or non-woven carbon fibers with high porosity, on top of which a microporous layer (MPL) is often coated with carbon powders with polytetrafluoroethylene (PTFE) as the binder. The MPL smooths the carbon fiber layer and support the catalyst layers (CLs). The CL is made of platinum nanoparticles supported on high surface area carbon bonded together by an ion conductive polymer, called the ionomer. The active sites of catalysts are located in a region, called the three phase boundary (TPB), where the reactant gas, an ionic conducting phase and an electronic conductive phase exist.

Based on the electrolyte materials used, fuel cells are classified into five major types i.e. proton exchange membrane fuel cells (PEMFC), alkaline fuel cells (AFC), phosphoric acid fuel cells (PAFC), molten carbonate fuel cells (MCFC) and solid oxide fuel cells (SOFC), as listed in Table 1.1.

Table 1.1 Types of fuel cells and their technical features of operation

Fuel cell types		PEMFC	AFC	PAFC	MCFC	SOFC
Electrolyte		Ion exchange membranes	Immobilized or mobilized KOH	Immobilized liquid H_3PO_4	Immobilized molten carbonates	Ceramics
Temperatures		80ºC	65-220ºC	190-205ºC	650ºC	800-1000ºC
Charge carrier		H^+	OH^-	H^+	CO_3^{2-}	O^{2-}
Catalysts	Anode	Pt/C	Pt, AgO, NiO	Pt(Ru)	NiO	Perovskites
	Cathode	Pt(alloys)/C	Pt, Ni	Pt	Ni	Ni

Polymer electrolyte membrane fuel cells (PEMFC) are the predominant type for automobile applications, which are commercially available from several automobile companies [1]. This technology is based on perfluorosulfonic acid (PFSA) type membranes e.g., Nafion®. The membrane material has high conductivity, excellent chemical stability, mechanical strength and flexibility, and demonstrated long-term durability, however, it functions only in a highly hydrated state. Therefore, the technology is limited to operation at temperatures below 100 °C under ambient pressure in order to maintain a high-water content in the membrane. The technology is therefore often referred to as the low

temperature PEMFC (LT-PEMFC). Challenges due to the low operating temperatures include system complexities for water and thermal management as well as establishment of a hydrogen infrastructure and poor fuel or oxidant impurity tolerance.

The water management is an issue as the fuel cell temperature is close to the water boiling point and hence involves a two-phase system, i.e., water vaporizes at low humidities and condenses at high humidities. The cooling duty is defined as the ratio of generated heat of a stack to the temperature difference between the stack and the atmosphere ($Q/\Delta T$), which implies that intensive cooling is demanded when a fuel cell operates at temperatures of 60-80 °C. At this temperature any contamination of e.g. CO, NOx or sulfur containing species in either reformat fuel or the atmosphere is poisoning the catalysts. These issues as well as the kinetics for electrode reactions are expected to improve at higher temperatures.

1.3 High temperature polymer electrolyte membrane fuel cells

PEMFCs operating at temperatures above 100 ºC is desirable in several ways. The tolerance to the fuel impurities e.g. CO poisoning is significantly mitigated. As a result reformate hydrogen from e.g. a simple methanol reformer without further CO cleanup can be used as fuel. The thermal management is simplified. In fact the heat from a fuel cell stack can be utilized to preheat water and methanol in case of methanol reformer, as illustrated in Figure 1.2. The research and development activities of HT-PEMFCs have been well reviewed [2] and recently updated [3]. In the following a brief review is given to materials, components and performance of HT-PEMFCs.

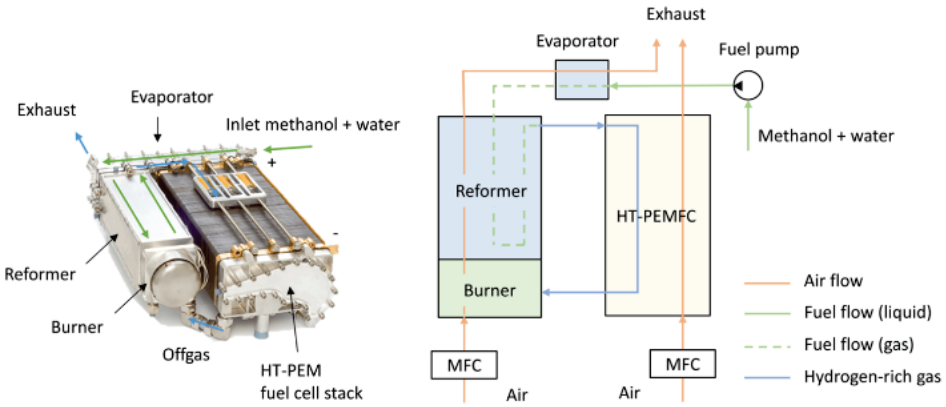

Figure 1.2 A 5 kW HT-PEMFC stack thermally integrated with a methanol reformer (left) and flow diagram for the system (right)

1.3.1 Polybenzimidazole based membranes

High Temperature polymer electrolyte membrane fuel cells (HT-PEMFCs) are based on phosphoric acid (PA) doped polymer membranes e.g. polybenzimidazole (PBI), as first reported in 1995 [4]. PBI is a class of heat-resistant heterocyclic thermoplastics [5] while PA is the dopant that combines high intrinsic proton conductivity with thermal stability and low volatility [6].

Poly-(2,2′-(m-phenylene)-5,5′-bibenzimidazole) (m-PBI, often referred to as PBI) is the most widely used polymer due to higher solubility and better processing characteristics. PBI is soluble in polar aprotic solvents such as N,N-dimethylacetamide (DMAc) into which LiCl is added as a solution stabilizer, which prevents formation of intermolecular hydrogen-bonds and the resultant polymer agglomeration [7]. By using typically DMAc as solution, polybenzimidazole films can be produced through casting on, e.g., a glass substrate by slow evaporation of the solvent at 60–120 °C. Strong interactions between the polymer and organic solvent result in high residual solvent content after drying. Washing of dry membranes in hot water is necessary to remove traces of the solvent as well as LiCl.

1.3.2 Acid doping and conductivity

Chemically, PBI is amphoteric with $pK_a = 5.23$ in its protonated form. Pure PBI in the form of dense films can absorb up to around 20% wt. of water, which is driven by the development of hydrogen bonds between the water molecules and the benzimidazole moieties. The water uptake corresponds to about 3 water molecules per polymer repeat unit.

When exposed to an acid, for example phosphoric acid, the benzimidazole units are fully protonated with formation of a polymeric salt with dihydrogen phosphate as the counter anions (Figure 1.3). This has been verified by ^{1}H NMR spectroscopic studies [8]. The acid doping level defined as the molar number of phosphoric acid to the polymer repeat unit (PRU):

$$ADL = \frac{W_{PA}/M_{PA}}{W_{PBI}/M_{PBI}} \tag{1.4}$$

where W_{PA} and M_{PA} are the mass and molar mass of PA, and W_{PBI} and M_{PBI} are the amss and molar mass of the polymer repeat unit, respectively.

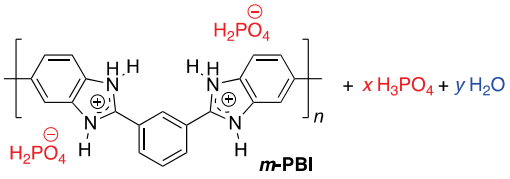

Figure 1.3 Chemical structure of poly-(2,2′-(m-phenylene)-5,5′-bibenzimidazole) (m-PBI) and the acid doping

The ADL can be controlled by varying the H_3PO_4 concentration of the doping solution. In the concentration range of up to 10-11 M, the ADL is around the 2, corresponding to about the full protonation. The typical ADL of 11-12 H_3PO_4 molecules per PRU can be achieved after equilibrating the membrane in 14.8 M (85 wt.%) H_3PO_4 at room temperature, as shown in Figure 1.4a.

The conductivity of phosphoric acid doped PBI membranes strongly depends on the acid doping level. At an acid doping level of lower than 2 where all acid molecules are likely involved in the acid-base ($BImH^+$ - $H_2PO_4^-$) interaction with the basic sites of the polymer, the membrane exhibits limited conductivity, being around 10^{-7} S/cm at room temperature. The presence of excess acid creates the acid anion chain ($H_2PO_4^-$–$H^{+\cdots}H_2PO_4^-$) as well as the acid and H_2O ($H_2PO_4^{-1}$–$H^{+\cdots}H_2O$), which significantly enhances the conductivity. At an acid doping level of 4-6 and temperatures, the conductivity reaches about 0.04-0.07 S/cm. The typical acid doping level of post-doped DMAc membranes for fuel cell uses is around 10-12, giving conductivities around 0.10-0.15 S/cm, see Figure 1.4b.

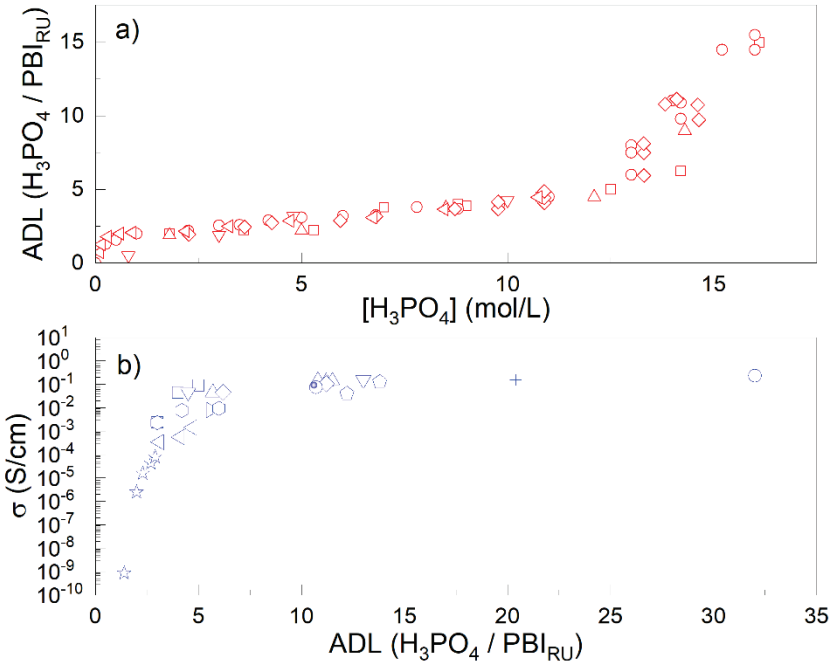

Figure 1.4 (a) Sorption isotherm for m-PBI in 85% H_3PO_4 at 25-30 °C and (b) ion conductivity at 160 °C for m-PBI as function of ADL under non-humidified conditions [9].

1.3.3 Catalysts and ORR kinetics

The start-of-the-art catalysts for HT-PEMFCs is carbon supported platinum nanoparticles. High surface area carbon blacks, e.g. Vulcan XC-72 (Cabot Corporation) with a surface

area of 250 m^2g^{-1} are the most widely used supports. Carbon as the catalyst support material is susceptible to corrosion, which is a function of temperature, potential, water partial pressure, and the electrolyte acidity. For HT-PEMFC applications the heat-treatment of carbon blacks at elevated temperatures is preferred in order to impart the character of graphite to reduce the number of structural defects where the corrosion starts. Alternatively carbon nanotubes, interestingly with a PBI wrapping layer, was found to improve the dispersion and stability of the Pt nanoparticles [10]. Commercial Pt/C catalyst products are available with the noble metal content from 10% to over 60% Pt on carbon, with typical Pt particles of 2-4 nm (see Figure 1.5).

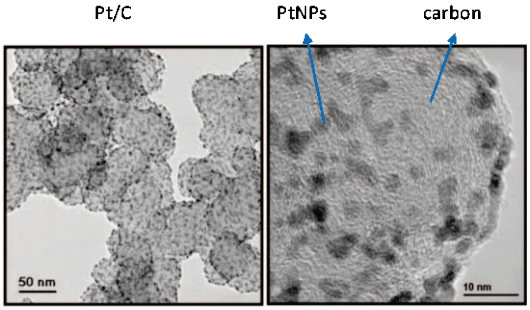

Figure 1.5 TEM images of carbon supported platinum nanocatalysts (Pt/C, 40%).

Platinum and its alloys are the state-of-the-art (SoA) catalysts for both LT-PEMFCs [11] and HT-PEMFCs. The oxygen reduction reaction (ORR) is slow in concentrated PA, even at the high operating temperature of HT-PEMFC. This is the dominant factor limiting the HT-PEMFC performance as compared to LT-PEMFC. The reported ORR exchange current density is about 2.2×10^{-9} A cm^{-2}, which is two orders of magnitude lower than the value of 2.8×10^{-7} A cm^{-2} for the ORR in LT-PEMFCs with PFSA membranes [12]. The low ORR activity of the Pt catalysts in the presence of PA is associated to the strong adsorption of the acid molecules via the formation of Pt-O bonds with acid anions ($H_2PO_4^-$) in the intermediate potential range [13]. Beside the slow ORR kinetics in PA, the oxygen solubility is low and oxygen transport slow, which further limits the HT-PEMFC performances [14,15].

A tremendous amount of work has been conducted in last decades in development of Pt alloys, primarily for LT- PEMFCs [16,17]. Concerns are the stability of the alloying metal

components as well as the carbon supports, which is apparently the main reason why only a few pieces of work have been published for HT-PEMFC [18,19] though weakening of the adsorption strength of PA by alloying with transition metals has been reported [20]. However the de-alloying is believed to form a Pt overlayer and an underneath alloy core. The underneath alloy core is still able to affect the properties of the Pt overlayer including weakened adsorption of phosphates [21].

1.3.4 Gas diffusion electrodes

While LT-PEM electrodes are optimized for easy removal of water, HT-PEMFC electrodes should facilitate the acid retention, i.e., preventing the acid loss via penetration through the MPL and GDL. It seems that cracks within the MPL provide pathways, through which phosphoric acid flows into the GDL and further to the flow plates. Gas diffusion electrodes with a crack-free and thick MPL on a GDL substrate with small pores are considered beneficial to retaining the acid inside the catalyst layer during operation [22,23].

To optimize the catalyst layer structure i.e. the triple-phase boundaries, the early HT-PEMFC effort was made to investigate the effect of the polymer binder, which attaches the catalyst particles as an integral layer on the GDL. Inert polymers as PTFE has been used as the binder to provide hydrophobicity to the catalytic layer and thus a balance between open pores and acid filled pores. PBI is another widely used binder, which assumes to absorb and stabilize the acid. It is interesting that recent attempt succeeds by complete elimination of the binder in the catalytic layer [24,25]. The proton conductivity of the catalytic layer is provided by the liquid phosphoric acid, which migrates from the membrane to the catalyst layer driven by the capillary force, as schematically represented in Figure 1.6.

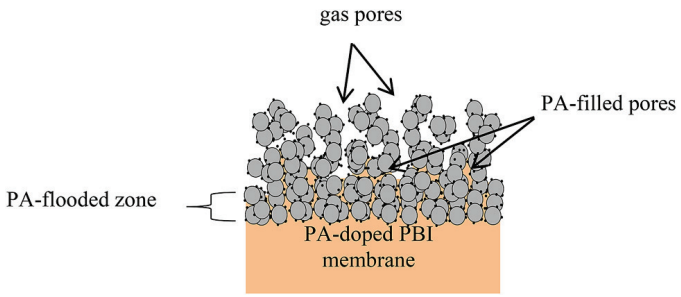

Figure 1.6 Schematic representation of a binderless catalytic layer with capillary-transferred acid from the membrane as described [3]

1.3.5 MEA fabrication

It is a common practice to assemble HT-PEM MEA by hot-pressing two electrodes onto a membrane. The resultant MEAs are easy to handle and install in the fuel cell test hardware or stack. The typical hot-press temperature is around 150 °C, which is around the operating temperature of the fuel cells. This temperature is below the glass transition temperature of the polymer as well as the binder included in catalytic layers (PBI, PTFE or PVDF), which means that there is no bonding of MEA constituents. Because of this, the role of hot pressing other than to ease the handling of electrodes during MEA fabrication is questionable. It seems that there is a practical tendency to omit the hot-pressing of MEAs in many recent studies and the assembling is made directly in the fuel cell test hardware due to clamping torque at operational cell temperature. Hot pressing can of course facilitate the transfer of free PA from PA-doped membranes to catalytic layers and probably improve the break-in of MEAs. Figure 1.7 shows an SEM image of a PBI based MEA cross section. The carbon fiber gas diffusion layers are coated with a macro porous layer of PTFE bonded carbon black. The cathode catalyst layer is thicker than the anode catalyst layer because different platinum loadings are used.

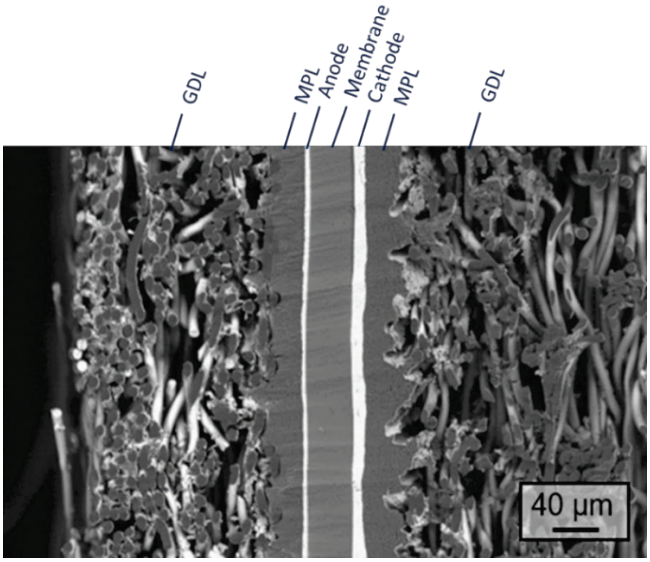

Figure 1.7 An SEM image of a HT-PEMFC MEA cross section.

1.3.6 Start-of-the-art performance and applications

The state-of-the-art PBI membranes have a pristine thickness of 40-50 µm, which after doping at an ADL 11-12 H_3PO_4/PRU have a thickness of ca. 60-80 µm. With a proton conductivity of e.g. 0.07 Scm^{-1} at 160°C the membrane would exhibit an area specific resistance (ASR) of 0.085 $\Omega \cdot cm^2$.

The Pt loading used in commercial HT-PEMFCs is around 0.7-0.8 mg_{Pt}/cm^2. Great efforts has been made during the last years to reduce the Pt loading of the electrodes while keeping a reasonable performance output. In laboratory cells electrodes with Pt loading lower than 0.3 mg_{Pt}/cm^2, sometimes even than 0.1 mg_{Pt}/cm^2, have been reported with peak power over 0.40 W/cm^2 [26]. The feasibility of such electrodes in industrial cells operating with reformate fuels has not been verified.

These commercial HT-PEMFCs are claimed to operate at up to 200 °C under ambient pressure with no humidification and can tolerate up to 3%CO at 150-200 °C. Operating with methanol reformat with typical compositions of 69.2% H_2, 22.3% CO_2, 1.4% CO and 6.9% H_2O under ambient pressure, the state-of-art performance of commercial Dapozol®

or Celtec® MEAs is reported to be about 0.67-0.70 V at 0.2 A cm^{-2} [27] or a peak power density of 0.45-0.50 Wcm^{-2} at around 1.0 A cm^{-2} [28].

Commercially HT-PEMFC membranes and MEAs are supplied by Danish Power Systems (Dapozol® membranes and MEAs), Advent (TPS® and Celtec® P1100W MEAs) and BASF (Celtec® membranes and MEAs). The stack and power unit suppliers include SerEnergy, Advent, Siqens and Blue World Technologies, among others.

Siqens GmbH supplies Ecoport 800 as well as Ecocabinet power units equipped by an HT-PEMFC stack and a methanol reformer with a maximum power output of 800 W at 24 V DC. Advent supplies two series of HT-PEMFC stacks. The Ianus series of stacks supply power in a range of 1–3 kW with liquid cooling and direct generation of steam for heating or reforming uses. The other series, Argo series in a power range from 100 to 500 W, are air-cooled for applications, e.g., as battery range extenders. SerEnergy has installed more than 1000 HT-PEMFC power units worldwide. Their current products on the market include outdoor cabinets with power outputs ranging from 5 to 15 kW at 48 V DC to methanol power systems (H3 5000) with nominal power outputs of 3.75 kW and max power outputs of 5 kW. These fuel cell stacks are integrated with methanol reformers for on-site hydrogen generation, where waste heat from fuel cell stacks is recovered and used for methanol and water evaporation in reformer systems. The cabinets are for either on-grid or off-grid applications, e.g., backup, supplemental or continuous power supply. Applications of HT-PEMFC technology as an automotive range extender is the core business of Blue World Technologies.

1.4 Scope and structure of the thesis

The present study is devoted to experimental studies of HT-PEMFc focusing on the anode performance in the presence of fuel impurities e.g. CO and potential cycling. The thesis is based on three manuscripts prepared for publication.

Chapter 1 is a general introduction to fuel cells particularly HT-PEMFC.

Chapter 2 provides a comprehensive review and detailed discussion of the mechanisms of degradation and durability results.

Chapter 3 summarizes the main results and findings of the present works based on the three manuscripts.

Chapter 4 is a brief conclusion and perspective outlook relevant to the thesis work.

Appendix 1 is a manuscript entitled CO Poisoning in High Temperature Polymer Electrolyte Membrane Fuel Cells Operating with Diluted Hydrogen and Low Pt Loading Electrodes.

Appendix 2 is a manuscript entitled Hydrogen Oxidation and Evolution Kinetics in the Absence and Presence of Carbon Monoxide for High Temperature Polymer Electrolyte Membrane Fuel Cells.

Appendix 3 is a manuscript entitled Potential Cycling Test of High Temperature PEMFC Based on Acid Doped Polybenzimidazole Membranes.

2. DURABILITY ISSUES AND DEGRADATION MECHANISMS

2.1 Introduction

During operation all fuel cell components experience a degradation in performance, which can be either reversible or irreversible, leading to a gradual decrease in power output or eventually a failure of the entire system. Chemically, fuel cell components are exposed to a very aggressive environment with strong oxidizing and reducing conditions with reactive species such as acids and radicals under practical electrochemical potentials and temperatures. Degradation of fuel cell components include dissolution and sintering of catalyst nanoparticles, corrosion of catalyst supports, oxidation of polymers, loss of the doping acid and degradation of other components and materials.

A large number of literature works have been published in the area of degradation mechanisms of LT-PEMFCs [29]. For HT-PEMFCs, the presence of PA and elevated operating temperature significantly deteriorate the degradation, as discussed by Jakobsen et al.[30] and very recently reviewed by Seselj et al. [9]. Major factors that are reducing the durability of PBI cells include the loss of doping PA, polymer oxidation and membrane thinning, and platinum nanoparticle growth and hence active surface area decrease. The following is a brief summary of the degradation mechanisms and their interactions in HT-PEMFCs. Major factors that are reducing the durability of PBI cells include the loss of doping PA, polymer oxidation and membrane thinning, and platinum nanoparticle growth and hence active surface area decrease. The following is a brief summary of the degradation mechanisms and their interactions in HT-PEMFCs.

2.1.1 Acid doping

In spite of its excellent thermal stability, phosphoric acid (PA) undergoes dehydration at elevated temperatures. The condensation products include dimers, trimers and higher polymers of PA. The vapor pressure of 85% H_3PO_4 reaches 1 bar at about 156 °C i.e. its normal boiling point. This vapor pressure decreases significantly for concentrated acids. For example, 100% H_3PO_4 possesses a water vapor pressure of ca. 60 mbar at 170 °C. The presence of PBI was found to enhance the acid condensation [31] i.e. the acid doped PBI

membrane may exhibit about 10 times higher water vapor pressure than that of pure PA [3].

The vapor over a PA solution is primarily consisting of water. The acid content in the vapor phase at fuel cell operating temperatures i.e., 150-160 °C has been estimated to be about 0.7 µbar at 160 °C and 3.7 µbar at 190 °C. Considering the fuel cell operation with a significant airflow over a period of a few years the acid loss due to PA evaporation is not negligible. At a current density of 0.2 A cm^{-2} and stoichiometries of $\lambda_{H2/air}$ = 1.2/2.0, these saturated acid vapor pressure values can be translated into an acid loss rate of 3.6 and 19 µg m^{-2} s^{-1} as 160 and 190 °C, respectively [9].

Experimentally the acid loss has been measured by collection of the trace acid carried by the anodic and cathodic off-gasses. The reported acid loss data from PBI cells in literature vary to a great extent also under much varied conditions. Under steady state operation at a typical load of 0.2 A cm^{-2} with low stoichiometry hydrogen and air flows at 150-160 °C, the acid loss data seem to be consistent in a range of a few µg m^{-2} s^{-1} [9]. This is in good agreement with the estimation from the acid vapor pressure, indicating the major mechanism of the acid loss via evaporation. This is further verified by the acid loss data at elevated temperatures, which follows the increasing trend of the acid vapor pressure [32,33]. The acid loss via the evaporation mechanism implies also the significant impact of gas stoichiometries i.e. the total gas flow as the carrier of the PA vapor. Søndergaard et al. [34] reported a significant acid loss and hence fuel cell degradation at higher gas-flow rates.

PA within the membrane is mobile. During the assembling of an MEA, the PA redistributes from the membrane into the catalyst layers, leading to establishment of the triple phase boundary at the interface [35]. It is also a common practrice that a PBI cell needs a break-in period duirng which the cell performance slowly improves to reach a steady state within a few hundred hours [36,37]. As shown by Kwon et al. [38], after the break-in about 15% of the acid in the membrane was transferred into the catalyst layers.

During operation of a fuel cell, the acid electrochemically migrates from the cathode to the anode and is balanced by the back diffusion in the opposite direction. At high current densities, e.g., 800 mA cm^{-2}, H_3PO_4 droplets were observed at the GDL [39]. By in situ

measurements of the acid transport by means of platinum microelectrodes, Becker et al. [40,41] reported an anion ($H_2PO_4^-$) transference number of up to 4% and an acid diffusion coefficient in PBI membrane of 10^{-11} m^2 s^{-1}. This suggests a fact that an acid concentration gradient will be developed across the membrane in fuel cells. The mobility of PA within the membrane is a trigger for further PA loss, resulting in higher acid loss rates at higher current densities, as reported by Søndergaard et al. [34]. With help of in-operando imaging techniques [22,42], it was observed that PA penetrated through the catalyst layer and gas diffusion layer at the anode side at higher current densities.

2.1.2 Polymer membrane degradation

Under fuel cell operating conditions, the polymer membrane experiences stressors that may ultimately result in mechanical failures, polymer oxidation and membrane thinning.

The mechanical stressing, resulting from the MEA assembling, thermal and wet swelling/shrinking during start/stop or load cycling, may cause the membrane tearing, cracking or creeping. Acid doped PBI membranes at ADL = 11-12 are mechanically soft, having an elastic modulus of only a few MPa at the fuel cell operating temperatures [43]. Mechanical failures are hence of critical concern for the durability of PBI membranes. During fuel cell operation, the humidity and therefore the membrane swelling and shrinking vary with the changes of the fuel cell load. Maier et al. [44] reported that, when the cell current density changes from 0 to 140 mA cm^{-2}, a membrane swelling of 20% was observed.

The oxidative degradation of the polymer, by hydrolysis, oxygen or radical attack, can lead to membrane thinning, pinhole and hotspot formation. As a result the increase in the hydrogen crossover, decrease in the OCV and ultimately collapse of the membrane may occur [45].

During cell operation, oxidative degradation of the membrane may happen due to oxygen radicals. Radicals, hydroxyl (·OH) and hydroperoxyl (·OOH), are generated from hydrogen peroxide formed due to the gas crossover. The radical stability of PBI is often evaluated by the so-called the Fenton test using a reagent typically composed of 3% H_2O_2 and 4 ppm Fe^{2+} at 68 °C. The results showed that the mass loss during the Fenton test showed a clear

decrease trend as the molecular weight of m-PBI increases. Crosslinked and copolymers have also better stability towards the radical oxidation [3].

Significant polymer oxidation as well as PA depletion is evidenced by membrane thinning after prolonged fuel cell operation. The membrane thinning will result in inreased crossover of hydrogen and air, and therefore a lowered OCV of fuel cells. Several studies based on cross-sectional SEM imaging of tested MEAs seem to support that membrane thinning and collapse are responsible for the faster performance degradation in the later period of the fuel cell lifetime. One example is given in Figure 2.1 from Oono et. al. [46].

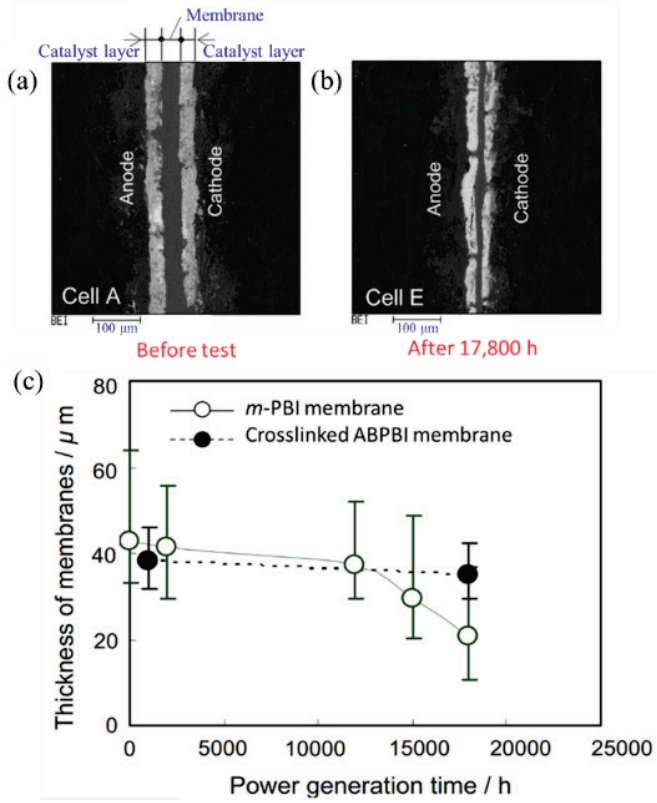

Figure 2.1 (a) Cross-sectional MEA images with m-PBI membranes (a) before test and (b) after 17,800 h operation at 0.2 A cm^{-2} and 150 °C. (c) Membrane thinning during the durability test for m-PBI and cross-linked ABPBI [46].

For cells based on a linear PBI membrane that had been operated at 150 °C and 0.2 A cm^{-2} for 17,800 h. A cell based on a crosslinked AB-PBI membrane was operated in parallel. For the cell based on the linear PBI, a significant reduction of the thickness was observed after 13,000 h of operation and the end of life (EoL) thickness of the membrane was about half of the initial value. For the crosslinked AB-PBI membranes, a much smaller decrease in the thickness occurred after 17,500 h, indicating the suppression of the polymer degradation by chemical crosslinking.

2.1.3 Catalyst degradation

The loss of the electrochemical surface area of Pt catalysts attributes to significant degradation of fuel cell performance. Several mechanisms have been proposed to cause the Pt particle growth and hence the loss of the active Pt surface area, as illustrated in Figure 2.2. One is the catalyst coarsening due to the migration of particles i.e., agglomeration or sintering of the metal particles. This mechanism involves movement of Pt adatoms between neighboring particles on the carbon support surface from small particles to large ones, known as the Ostwald ripening [47].

The electrochemical dissolution of Pt can be a direct dissolution of the metal:

$$Pt \rightleftarrows Pt_2 + 2e^- \qquad E(V) = 1.19\ V + 0.029\ V \cdot \log[Pt^{2+}] \tag{2.1}$$

At high potentials, an oxide layer is formed on the metal surface. The formation and dissolution of this depends on the electrolyte pH and electrode potential:

$$Pt + H_2O \rightleftarrows PtO + 2H^+ + 2e^- \qquad E(V) = 0.98\ V - 0.59\ V \cdot pH \tag{2.2}$$

The formed oxides are unstable in acidic electrolytes and can dissolve either chemically or electrochemically with the equilibria as follows:

$$PtO + 2H+ \rightleftarrows Pt2+ + H_2O \tag{2.3}$$

$$PtO_2 + 4H^+ + 2e^- \rightleftarrows Pt^{2+} + H_2O \tag{2.4}$$

The solubility of Pt changes with a number of factors such as the electrode potential, type and pH of electrolytes, and temperature. It depends also on the morphology of platinum e.g., nanoparticles or wires.

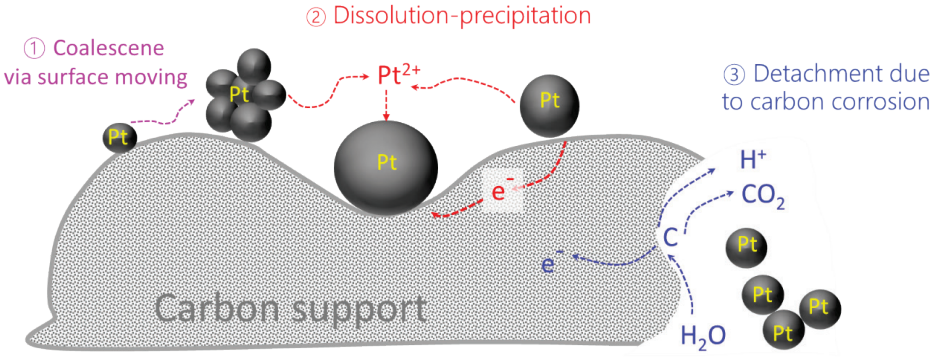

Figure 2.2 Three mechanisms for Pt particle growth in fuel cells. 1) Pt particle coalescence; 2) Pt dissolution from smaller particles and redeposition on larger particles; 3) diffusion of dissolved Pt into the conducting electrolyte where it may be reduced by hydrogen crossing over from the anode.

Furthermore the Pt ions are mobile in the electrolyte phase. When encountering electrons transported through the carbon support, they can be redeposited on larger particles. This mechanism is also called electrochemical Ostwald ripening. As Pt ions are mobile in the ionomer phase they may also encounter hydrogen permeated from the anode and reduced inside the ion conducting membrane, resulting in the formation of the so called Pt band [48]. The Pt-band formation can, in turn, result in further membrane and MEA deterioration, as revealed for LT-PEMFCs.

The stability of carbon supported Pt nanoparticles in concentrated PA has been a subject in the early year research for PAFC [49]. This phenomenon has been recently revisited by Prokop et al. [50] showing the enhancement of the particle coarsening at elevated temperatures and a combined process of agglomeration/sintering and Ostwald ripening has been proposed at potentials above 0.70 V. In concentrated PA electrolytes the solubility of platinum was reported to increase from 10^{-7} to 10^{-4} M as the electrode potential increases from 0.8 to 1.0 V vs RHE at temperatures 176 - 196 °C [51]. For PBI cells, using the PA acid inventory the dissolution of the platinum catalyst under OCV was estimated to be up to 2-5% of the total catalysts with the loading of 0.5-1.0 mg_{Pt} cm^{-2} in a cathode [3].

As the catalyst support, carbon is thermodynamically instable in HT-PEMFCs. Corrosion of carbon causes detachment of Pt particles, which triggers further agglomeration of Pt particles. Another effect of carbon corrosion is the formation of surface oxides, causing a decrease in hydrophobicity of the catalyst layer and possibly PA flooding.

Operation of HT-PEMFC modes involving exposure of electrodes to high cell voltages near the OCV will lead to significant carbon corrosion. A critical issue is the start-stop of a fuel cell, during which the transition of the H_2/air to an air/air mode generates a reverse current resulting in electrode potentials higher than the OCV [52,53]. Similar phenomena have been observed during the fuel starvation of a fuel cell. In both cases, extraordinary degradation of the electrode performance, in terms of activation loss due to the Pt particle growth and mass transport losses due to the catalyst layer thinning or even collapse would occur.

To mitigate the carbon corrosion and resultant catalyst degradation, structured carbons such as graphitized carbon blacks [54] and carbon nanotubes [55] have been innvestigated for HT-PEMFCs. Alternative catalyst supports including tungsten carbides/oxides [56], SiC [57]or SiC-TiC [58] composites have also shown improved catalyst stability.

2.2 Durability (I) – steady state operation

Of the degradation mechanisms discussed above, the electrolyte degradation in terms of acid loss and polymer oxidation is significant only under extended time scale unless under intensified stressors such as high temperatures, high current densities or/and extreme gas stoichiometries. Catalyst degradation in form of the electrochemical surface area (ECSA) losses is originated from nanoparticle agglomeration, metal dissolution and carbon support corrosion, which is responsible for the initial and steady performance degradation through the durability tests [33,59]. It seems conclusive that a low degradation rate is possible over long-term operation under the steady state mode while severe degradation would occur under the dynamic operating mode such as potentials close to OCV, high temperatures, or start/shutdown events. In the section the durability test results are categorized into static and dynamic operation.

A large number of durability tests have been performed under static operation i.e., in a continuous mode with a constant load. A summary of these works is listed in reference [9].

Most studies were conducted in a moderate range of operating conditions i.e., a current density of 0.2 A cm^{-2}, temperature of 150-160 °C, dry hydrogen and air with low stoichiometries $\lambda_{H2/Air}$ = 1.2-1.5/2.0. Under these conditions the acid loss and catalyst degradation is minimized. Several groups have performed long-term durability studies in a time frame of up to twenty thousand hours i.e., over a period of 2 years.

Oono et al. [46], tested five identical cells for periods of 150 h (as reference), 2000 h, 12,000 h, 15,000h and 17,800 h under conditions of 150 ºC, 0.2 A cm^{-2} and hydrogen and air. Until 14,000 h a gradual decline of the cell performance was observed at a rate about 3.6 μVh^{-1}. In the following time a more rapid decrease occurred. The performance decay of 10% of its peak value was attributed to the steady loss of the catalyst active surface area due to the nanoparticle agglomeration, while the rapid performance decrease was suggested to correlate with the acid loss and polymer thinning. Another study by the same author group was based on cross-linked AB-PBI membranes for a period of 17,500 h, showing an average degradation rate of 1.9 $\mu V\ h^{-1}$, compared to 3.8 $\mu V\ h^{-1}$ for PBI membranes.

The work by Søndergaard et al. [60], used a thermally cross-linked polybenzimidazole membrane. The test was conducted at 160 °C and 0.2 A cm^{-2} for periods of up to 13,000 h. Attempt was made to avoid as much disturbance as possible with in-line diagnostics only via electrochemical impedance spectroscopy (EIS). The cell showed an average degradation rate of 0.5 $\mu V\ h^{-1}$ within the first 9,200 h and of 1.4 $\mu V\ h^{-1}$ for the full test period of 13,000 h. As a comparison a membrane based on linear PBI (i.e., with no crosslinking) was used as a reference, which showed degradation rates of 2.6 $\mu V\ h^{-1}$ and 4.6 $\mu V\ h^{-1}$ within the respective time span. Another interesting study was done by Pingitore et al. [61] based on directly cast meta/para-PBI copolymer membranes. They reported a voltage decay of 0.69 $\mu V\ h^{-1}$ over a time frame of up to 17,500 h. Such low degradation rates of a few $\mu V\ h^{-1}$ have also been verified by several other groups, for example, Rastedt et al. [62] reported an average degradation rate of 1.7 $\mu V\ h^{-1}$ for the first 3,000 h of operation and of 3 $\mu V\ h^{-1}$ for an operation duration of more than 9,000 h.

Operating temperature is a stressor of the HT-PEMFC degradation. Oono et al. [33] investigated the degradation in a temperature range from 150 to 190 °C. Compared to the average degradation rate of 3.6 $\mu V\ h^{-1}$ at 150 °C, operation at 170 °C and 190 °C showed 10% of the peak performance loss in a duration of 4,400 and 1,220 h, respectively,

corresponding to an average degradation rate of ca. 11 and 60 μV h^{-1}. Similarly faster degradation rates were also reported by Søndergaard and coworkers [34] and by Galbiati et al. [63] at 180ºC, and by Leader et al. [64] and by Aili et al. [65] at 200 °C.

The increased performance degradation at elevated temperatures can be attributed the carbon corrosion and platinum particle agglomeration, while the major cause is the acid loss via the evaporation mechanism. Zhang et al. [66] prepared PBI composites containing nano SiO_2, which led to an in-situ formation a conductive PA/phosphosilicate phase and hence stabilize PA and the cell performance at temperatures above 200 °C.

The current load in a range higher than the typical value of 0.2 A cm^{-2} has been shown to increase the performance degradation. In a study of cells with thermally cured membranes at 160 °C over a period of 2,000 hours Aili et al. [67] showed a degradation rate of 43 μV h^{-1} at 600 mA cm^{-2}. The results by Søndergaard et al. [34] using current densities from 200 to 800 mA cm^{-2} showed close correlation of the increased degradation rate at higher current densities via the acid loss mechanism. This is understandable since a high current density is accompanied by an increased total gas flow of both hydrogen and air, which are carriers of the evaporated acid out of the cell.

All of the durability studies discussed above were carried out using hydrogen as fuel. Reformate H_2 from methanol reforming contains CO_2, CO, H_2O as well as other trace components. The CO tolerance is primarily dependent on the volume or molar CO/H_2 ratio due to their competitive adsorption on the Pt catalyst sites, however other components have additional dilution effects that should be taken into account [68–71]. The higher degradation rates under operation with reformate fuels can be related to the higher total gas flow and higher water activity through the cell anode, leading to faster PA loss. A recent study by Hjuler et al. [72] used a synthetic reformate fuel containing 69.3% H_2, 22.3% CO_2, 6.9% H_2O and 1.4% CO at 160 ˚C. Low stoichiometries ($\lambda_{H_2/Air}$ = 1.3/2.5) were carefully controlled. At a current density of 0.4 A cm^{-2} the recorded cell voltage decay over a test period of 10,000 h is shown in Figure 2.3. The fuel cell performance at beginning of life (BOL) reached the peak of life (POL) of 0.645 V, after the break-in of 262 hour. Over the first 4,800 h, an average decay rate of only 4.8 μV h^{-1} was observed over the first 4,800 h. It increased slightly to 6.4 μV h^{-1} for the period from 4,800 to 9,000 h and then further to 9.3 μV h^{-1} for the period from 9,000 to 10,000 h.

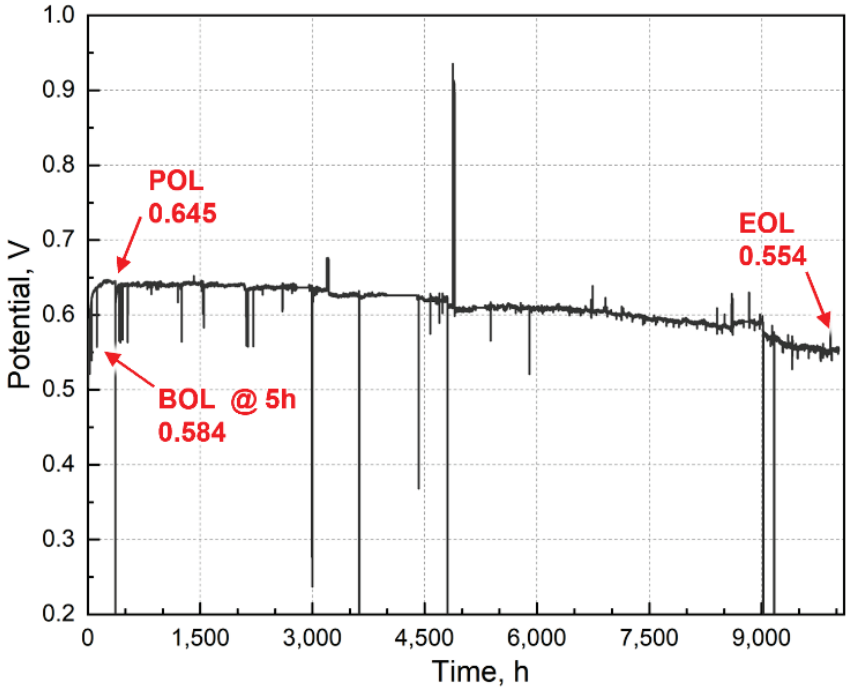

Figure 2.3 Cell voltage versus time during a steady state long-term test. The active surface area of the electrodes was 21 cm2. The fuel was synthetic reformate containing 69.3% H_2, 22.3% CO_2, 6.9% H_2O and 1.4% CO. The stoichiometries were $\lambda_{H2/Air}$=1.3/2.5. The cell was operated at 0.4 A cm^{-2} and 160 °C [72].

In summary, low degradation rates of < 2 µV h^{-1} have been repeatedly reported by several groups. After a peak performance is reached within a few hundred hours a steady initial performance degradation develops, attributable to the catalyst agglomeration as well as the PA loss. The steady membrane degradation, in terms of the conductivity due to the PA loss and polymer oxidation, reaches a critical point after a certain period of typically 10,000 h, after which a faster performance decay occurs. By defining a lifetime as 10% of the peak cell voltage loss, a degradation rate of < 2 µVh^{-1} can be translated to a lifetime 35,000 h, close to the targeted 40,000 h for stationary applications. Temperature, current density, gas stoichiometry are, however, all significant stressors of the cell lifetime.

2.3 Durability (II) – dynamic operation

Fuel cells are much more stressed when operating in dynamic modes i.e., with thermal, load or start-stop cycling. The dynamic cycling exposes the cathode to high potentials, leading to severe corrosion of carbon supports and growth of the catalysts. The thermal expansion and contraction of membranes and electrodes create stress at the interface and deteriorate the MEA integrity. In addition, the varying amount of water may change the concentration and volume of the PA in both membranes and electrodes. Moreover during start-stop processes, liquid water might be present at low temperatures, which is believed to enhance the acid leakage.

Accelerated stress test (AST) protocols often used for the dynamic durability studies include start-stop, load cycling and thermal cycling.

2.3.1 Start-stop cycling

The start-stop cycling protocols consist of cycles entailing a cell cold start, baseline operation and subsequent shutdown. The degradation of the cell voltage per single cycle is usually taken as a measure of cell durability.

Start/stop cycling instigates additional degradation mechanisms compared to the static operation mode. Reiser et al. [52] identified an accelerated degradation mechanism by the so-called reverse-current. During a start or stop event, the H_2/air front sweeps through the anode compartment and instigates a local reverse internal current and hence an electrode potential as high as 1.4-1.5 V. This high potential accelerated the carbon corrosion in the catalyst layer, which triggers the Pt particle growth and the reduction of the active surface area of the catalysts. Another consequence is the loss of the electrode hydrophobicity and hence the increase in the mass transport resistance. It also accelerates the catalyst layer thinning and eventually leads to collapse of the cathode integrity.

Another significant degradation mechanism during the start-stop is the electrolyte redistribution due to the volume change of the liquid electrolyte caused by thermal expansion and water formation. Low relative humidities and high temperatures lead to highly concentrated PA while at low temperatures and rising relative humidities the PA concentration decreases due to the hygroscopic properties of the electrolytes.

The performance degradation of HT-PEMFCs under a constant load of 0.2 A cm^{-2} with and without start/stop cycles is exemplified in Figure 2.4. Within a timeframe of 6000 h with 240 daily start cycles, a degradation rate is 0.2 mV per cycle or 11 µV h^{-1} on a time basis was observed, which should be compared to 5 µV h^{-1} for the continuous operation [59]. The cells under continuous and start/stop cycling operation exhibited similar ohmic resistance and oxygen reduction overpotential losses while the start/stop cycling led to significantly increased cathodic mass transport loss, attributable to the corrosion of the cathode catalyst support.

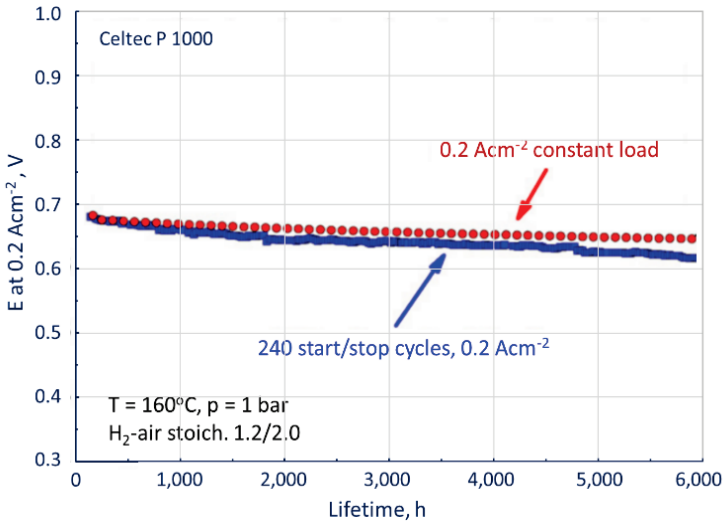

Figure 2.4 Cell voltage at 0.2 A cm^{-2} as a function of time of a constant load without (red circles) and with start/stop cycles (blue squares). $\lambda_{H2/air}$ = 1.2/2, T = 160 °C, p = 1 bara [59].

In a daily start-stop cycling test, with operation at 0.2 A cm^{-2} and 160 °C and idling at 25°C overnight, Pinar et al. [73] purged the cell with N_2/N_2 during the excursion at the cell temperature below 120 °C. They observed an overall voltage loss rate of 12.6 µV h^{-1} or 600 µV per cycle within a test duration of 115 days.

It seems that the overall performance loss caused by each start-stop cycle is generally more than 200 µV per cycle if no mitigation measures are taken. Oyarce et al. [74] studied different start-stop strategies including H_2 consumption (fuel shut off with load on), air purge of anode, O_2 consumption (air shut off with load on) and H_2 purge of cathode.

Compared to the no purge operation all these strategies showed considerably low degradation rates. While the H_2 consumption and air purge on the anode showed limited protection, the O_2 consumption and H_2 purge on the cathode showed one order of magnitude lower degradation rate.

2.3.2 Load cycling

Load cycling i.e., periodical change of the load level is a commonly used strategy to stimulate an accelerated degradation of fuel cells. The cycling exposes a cell to the severe corrosion of carbon supports and the sintering of noble metal catalysts. Platinum catalyst dissolution is also intensified during the load cycling, as the metal oxide solubility in the electrolyte is dependent on the cathode potential. The first study on HT-PEMFCs by Yu et al. [32] showed that a current density cycling led to a more than five times higher degradation rate after only 500 h compared to the constant load operation for 2,500 h.

The load cycling test can be divided into low load (0-0.2 A cm^{-2}) and high load (0.2-1.0 A cm^{-2}) levels, the former focusing on catalyst/electrode while the latter on membrane electrolyte evaluation. The low load operation often involves exposure to OCV, which is inevitable during the idling of a fuel cell.

The OCV hold is the most destructive stressor of the operating conditions. An exposure of a fuel cell to OCV was reported to exhibit a voltage degradation of over 400 µV h^{-1}, showing significant increases in both the activation and mass transport resistance as well as a reduction of the cathode elctrochemically active surface area (ECSA) Qi et al. [75] compared to the fresh cathode, an increase of the Pt nanoparticle size by more than 4 times was reported after 245 h of exposure to OCV.

Studies on the low load cycling, typically between 0 and 0.2 - 0.5 A cm^{-2} involve dwelling of fuel cell at OCV [27] Instead of OCV (0 A cm^{-2}) some authors cycled the cell with a small current density [76]. Similarly, potential cycling studies between 0.6 and 1.0 V, corresponding to the low load cycling, have also been employed [48,54]. As long as the OCV or high voltages near OCV are implicated, higher degradation rates of 100-400 µV/h are often reported, primarily due to the activation polarization loss (catalyst degradation).

Schonvogel et al.[77] seem the first performing AST under high load cycling. They conducted a load cycling between 0.6 A cm^{-2} (4 min) and 1.0 A cm^{-2} (16 min) while for every 6 h the cell was idled at OCV for 10 min. A high degradation rate of 330 μV h^{-1} was reported, which is comparable to the low load cycling between 0 and 0.3 A cm^{-2}. This is understandable because an idling of cell at OCV is involved. A high load cycling study between 0.6 and 1.0 A cm^{-2} without involving the OCV exposure was reported by Büsselmann et al. [78]. In this case the degradation rate was as low as 32 μV h^{-1} over a 500 h testing period.

Comparative studies were carried out using a triangular sweep cycling with a relatively fast sweeping rate i.e. 16 s per cycle between 0.01 Acm^{-2} and 0.5 Acm^{-2} or between OCV condition and 0.5 A cm^{-2} with a dwelling at OCV for 2 s [79,80]. Over a test period of 400 h, a degradation rate of 34 μV h^{-1} was reported for the test without dwelling at OCV. For the cycling test with dwelling at OCV for 2 s, the reported degradation rate was, however, only slightly higher (44-45 μV h^{-1}).

It should be noted that, in addition to the catalyst degradation, mechanical stressing of the membrane due to the load cycling has also been detected with e.g., the micro-computed tomography (μ-CT) images and MEA thickness sensing [77]. The acid loss varies under operation with high current densities, apparently related to the higher water production, heat generation and gas flows. The timeframe of load cycling tests is generally limited to several hundred hours, during which little effect on the membrane degradation was observed. In other words little changes in the proton conductivity or the hydrogen crossover was reported due to the acid loss or polymer degradation during the load cycling tests.

2.3.3 Thermal cycling

Thermal cycling is probably the harshest stressor for the performance degradation as it imposes mechanical stresses on the membrane, electrode and their interfaces. The high temperature end intensifies the carbon corrosion, metal dissolution and acid evaporation while temperatures lower than 100 °C causes extra PA leaching due to liquid water.

The PA loss in the low temperature region has also been a concern when water is present in the liquid state. Lim et al. [81] suggested that the interaction between PA and water is stronger than that of the PA and PBI, which makes PA molecules segregate from the

membrane in the presence of water. In a triangular thermal cycling test between 80 and 160 °C with a ramp of 10 °C min^{-1} under a constant current density of 0.15 A cm^{-2}, the cell voltage was found to decrease from 0.78 V to about 0 V after 70 cycles.

Park et al. [82] conducted a thermal cycling test between 180 °C (30 min at OCV) and 30 °C (30 min at OCV) and I-V curves were recorded every 48 cycles. An OCV decrease of 13 mV per cycle was observed for PBI membranes after 50 cycles while 2 mV per cycle for a PTFE-reinforced membranes after 150 cycles.

A start-stop test by Hjuler et al. [72] also involved the temperature cycling from 50 °C (at 0.01 A cm^{-2}), 165 °C (at 0.31 A cm^{-2}) and 175 °C (at 0.55 A cm^{-2}) and back to 50 °C. Each cycle took ca. 13.3 h and in total 240 cycles corresponded to a period of more than 4,000 h. An overall degradation rate of 480 μV per cycle at 0.31 A cm^{-2} was observed.

In summary, the load cycling test under a constant temperature is an effective stressor and often categorized into low load (0-0.2/0.5 A cm^{-2}) and high load (0.2-1.0 A cm^{-2}) levels. High decay rates of the performance are observed for low load cycle tests, primarily due to the catalyst aggregation and the carbon support corrosion caused by the high electrode potentials. As long as OCV or near OCV potentials are entailed in the load cycling tests, the performance degradation rate can be ranging from 100 to 300 μV h^{-1}.

The main mechanism for the performance degradation under high load cycling, on the other hand, is the PA loss, which eventually results in membrane degradation e.g. decreased proton conductivity. The membrane degradation, as characterized by the hydrogen crossover and/or OCV observation, is, however, not always detectable during the short timeframe of the load cycling test. The OCV exposure is one of the most destructive stressors, which may lead to a cell voltage degradation of over 400 μV h^{-1}, originating from significant increases in the activation loss due to the ECSA reduction and mass transport loss due to the carbon corrosion and catalyst layer collapse.

Start-stop and thermal cycling induce accelerated degradation because of the mechanical stressing of membranes, electrodes and their interfaces. During start-stop the hydrogen/air front over the anode chamber may cause a reverse current and therefore an excursion of the electrode potential to 1.4-1.5 V. As a result, carbon corrosion and catalyst agglomeration are the major mechanisms of the degradation. It is well documented that a

start-stop cycle, without taking any mitigation cautions, may cause a performance degradation of more than 200 μV per cycle. The high temperature tour of the thermal cycling will deteriorate the catalyst. The low temperature region, lower than 100 °C in particular, raises a new issue of the PA leaching due to the liquid water formation.

2.4 Conclusive remarks

With great advancement in the last decades, the HT-PEMFC technology approaches its maturity to applications. Long-term durability is one of the most significant barriers to the market penetration. Major issues of the material and component degradation include the loss of doping acid, oxidation and thinning of polymer membranes and platinum nanoparticle growth and resultant active surface area decrease.

The PA loss is primarily via the evaporation mechanism but supplemented by the electrochemical migration mechanism upon the passage of the current. This implies the significant impact of the operating temperature, gas stoichiometries and current densities. Under a steady state operation at a moderate current density, the acid loss rate is about a few μg m^{-2} s^{-1}, based on which the PA inventory of the MEAs seem sufficient to support the desired lifetime, but any harsh e.g. dynamic operation makes the PA inventory a critical parameter.

Polymer oxidation and the resultant membrane thinning is less of an issue for short-term applications. For long-term durability, polymer chemistry plays a central role in strengthening the membrane, improving the acid retention and oxidative resistance of the membrane. Several studies have demonstrated that the use of mechanically robust membranes allows for longer lifetimes – in fact most of observed long-term durabilities over 10,000 hours are achieved with modified or crosslinked polymer membranes.

Catalyst degradation is well understood by the steady loss of the active surface area loss via the physical as well as electrochemical Ostwald ripening of platinum nanoparticle and via deteriorated by the carbon support corrosion. Both carbon corrosion and metal dissolution are strong functions of electrode potential as well as temperature.

The technology has been well demonstrated under steady state operation. At a constant load typically at 0.2-0.4 A cm^{-2} at 150–160 °C, a voltage degradation rate of a few μV h^{-1}

has been repeatedly reported, indicating the potential in meeting the lifetime requirements of many devices. Challenges remain at higher temperatures, current densities or reactant stoichiometries. Durability under dynamic operation such as start-stop, load and thermal cycling is the most critical. Idling of the cell at OCV or operating at near OCV (low load) dramatically enhances the catalyst degradation.

3. SUMMARY OF THE THESIS

3.1 Introduction

Main experimental works and results are presented in the manuscripts. A brief introduction of the conducted studies and the key results are summarized in following.

3.2 CO poisoning and fuel diluting

3.2.1 Introduction

Carbon monoxide poisoning is a critical issue for LT-PEMFCs, which can tolerate 10-20 ppm CO at 80°C [83,84]. As a result high purity hydrogen is needed as a fuel and the technology is therefore facing challenges of the infrastructure for hydrogen distribution and supply. On board produced hydrogen from e.g. methanol reforming contains always CO and other gas components.

The CO poisoning is via the competitive adsorption on Pt surface and hence reduces the active surface site numbers available for the hydrogen oxidation, because the anodic oxidation of hydrogen is essentially determined by the rate of hydrogen dissociative chemisorption.

HT-PEMFCs operating at temperatures around 150-160°C are well known to be able to tolerate 1-3 %CO [85–87] corresponding to 10,000-30,000 ppm and can therefore be fueled by the reformat hydrogen [88,89]. Studies on the CO poisoning in HT-PEMFC have been conducted using high platinum catalyst loadings. Recent efforts are being made to lower the Pt loadings to a level ≤ 0.3 $mg_{Pt}\,cm^{-2}$ [90–92] or even down to the ultralow level of ≤ 0.1 $mg_{Pt}\,cm^{-2}$ [24,26,93–96]. The poisoning effect has, however, not been investigated for these low and ultralow Pt loading electrodes.

In addition, most of literature studies on the CO poisoning [97–100] have evaluated the CO tolerance in H_2/CO mixtures. Other gas components are also present in reformate fuels such as CO_2, N_2 and water vapor, depending on the fuel processing methods [101]. These components are often chemically inert but their diluting effect on the H_2 partial pressure

may also influence the CO poisoning as the practical H_2 concentrations in reformate fuels can vary in a wide range from 40 up to 80 vol% [102,103].

In the present work the effect of the CO poisoning in the presence of diluting gases was studied with electrodes of varied Pt loadings. Volume concentrations of H_2 from 20 to 80 vol% were investigated with an inert gas e.g. nitrogen or argon as the balancing gas. The studied CO concentrations varied from 0 up to 2.0 vol% while the electrode Pt loadings range from the industrial level of 1.3 down to 0.15 mg_{Pt}/cm^2.

3.2.2 Overview of test series

The effect on the CO tolerance was studied in four series. In Series 1, the effect of hydrogen dilution on a cell with a fixed high Pt loading at moderately high CO concentration was measured. The aim was to assess the effect of the hydrogen being diluted under typical conditions, though with a somewhat high, yet realistic CO level. Then the study was elaborated to include simultaneous variations of both hydrogen and CO concentrations in Series 2. The effect of the Pt loading on the anode was investigated in Series 3, where the Pt loading and CO concentration were varied but with no dilution of hydrogen apart from that resulting from the addition of CO. Finally, in Series 4, simultaneous variations of hydrogen and CO concentrations were investigated at a fixed low Pt loading. Table 3.1 provides an overview of the test series and the values of the three parameters.

Table 3.1 Overview of the test series and corresponding values.

	H_2 concentration (%)	CO concentration (%)	Pt loading ($mg_{Pt}cm^{-2}$)	Balancing gas
Series 1	20, 40, 60, 80, 100	1	1.3	N_2
Series 2	20, 40, 60, 80, 100	0, 0.5, 1.0, 1.5, 2.0	1.3	N_2
Series 3	Balance H_2	0.0, 0.25, 0.5, 1.0, 1.5, 2.0	0.15, 0.3, 0.6, 1.3	H_2
Series 4	80, 60, 40	0.0, 0.25, 0.5, 1.0, 1.5, 2.0	0.3	Ar

3.2.3 Effect of the platinum loading of pure H_2 performance

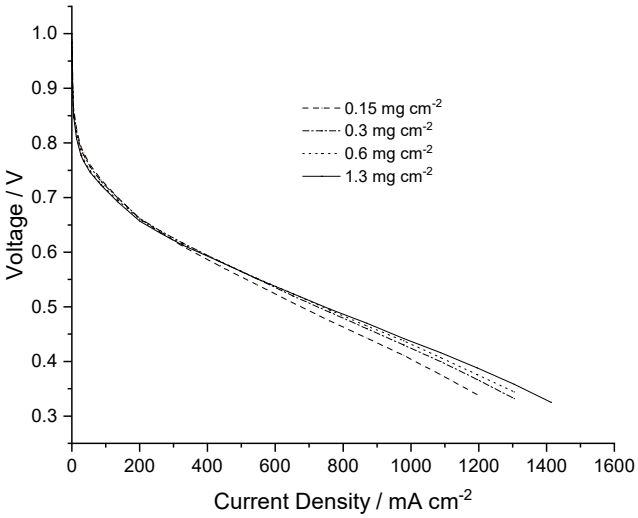

Figure 3.1 The I-V performance of HT-PEMFCs with different anode Pt loadings under operation with pure H_2 and air at 160 °C and ambient pressure

Operating with pure hydrogen, the I-V performance of HT-PEMFCs at 160°C is shown in Figure 3.1. Briefly speaking, a ten-fold reduction in the Pt loading from 1.3 to 0.15 $mg_{Pt}cm^{-2}$ does not result in any visible performance change in the practical current density of operation. This will serve as a baseline for the following study of hydrogen dilution and CO poisoning.

3.2.4 Effect of varying Pt loading on the CO poisoning

This section is devoted to a study of the CO poisoning with low Pt loading electrodes on pure hydrogen with further dilution. The studied CO contents were from 0.25 to 2.0% in H_2 and the anodes were made with Pt loadings ranging from 0.15 to 1.3 $mg_{Pt}cm^{-2}$. The as-measured I-V curves are presented in Figure S1. From the I-V curves the cell voltage values were read at a current density of 0.2 Acm^{-2} and plotted in Figure 3.2 as a function of the CO concentration.

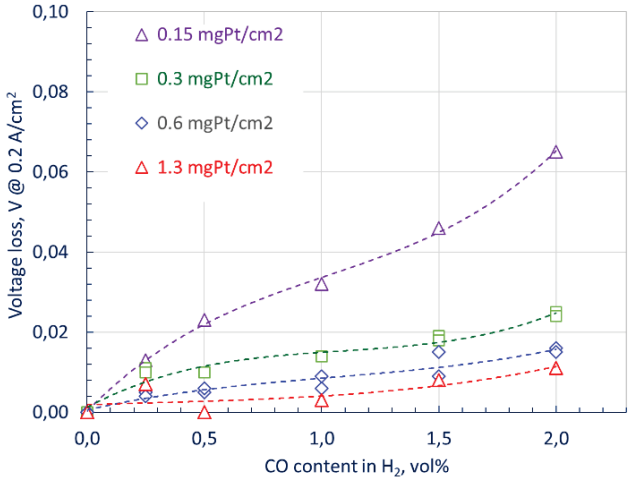

Figure 3.2 Cell voltage losses at 0.2 mA cm^{-2} due to addition of CO to pure hydrogen at varied concentrations. Data were obtained from I-V curves measured at 160°C with anodes of different Pt loadings as indicated in the figure.

It is clearly seen from the Figure 3.2 that the CO poisoning effect in the whole concentration range is enhanced as the Pt loading of the anode decreases. This seems apparent as the Pt loading of the anode is related to the total available active sites of the catalysts, though the Pt utilization, and therefore the specific e.g. mass based surface area, will be higher for the lower Pt loading electrodes. Attempt was made to normalize CO poisoning effect by multiplying the voltage loss by the Pt loading. The resultant cell voltage loss due the CO poisoning seems approximately correlated with the total active sites, as seen from Figure S2. Further study by the electrochemically active surface area, by means of CO stripping, for example, is planned.

3.2.5 Effects of hydrogen dilution on CO poisoning with low Pt loading electrodes

A low Pt loading anode of 0.3 $mg_{Pt}cm^{-2}$ was selected for the CO poisoning studies with hydrogen contents from 40, 60, 80 and 100% balanced by nitrogen. Figure 3.3 shows a set of the measurements comparing the CO poisoning in 100% and 40% H_2 (- 60% Ar) where the CO content was varied from 0 to 2.0%. Similar measurements will diluted hydrogen at 60% H_2 (- 40% Ar) and 80% H_2 (- 20% Ar) can be found in Figures S3&4.

At this low Pt loading, the anode showed a performance loss around 10 mV at current density of 200 $mAcm^{-2}$ when up to 2.0% CO is present in pure hydrogen. When hydrogen is diluted with an inert gas e.g. argon or nitrogen, the CO poisoning effect becomes much larger. As seen from the figure for 40%H_2, the presence of 0.25%CO had already a noticeable performance loss while 1.0 and 2.0% CO in 40% H_2 caused a voltage loss of 45 and 130 mV, respectively, for the low Pt loading anode with 0.3 $mg_{Pt}cm^{-2}$.

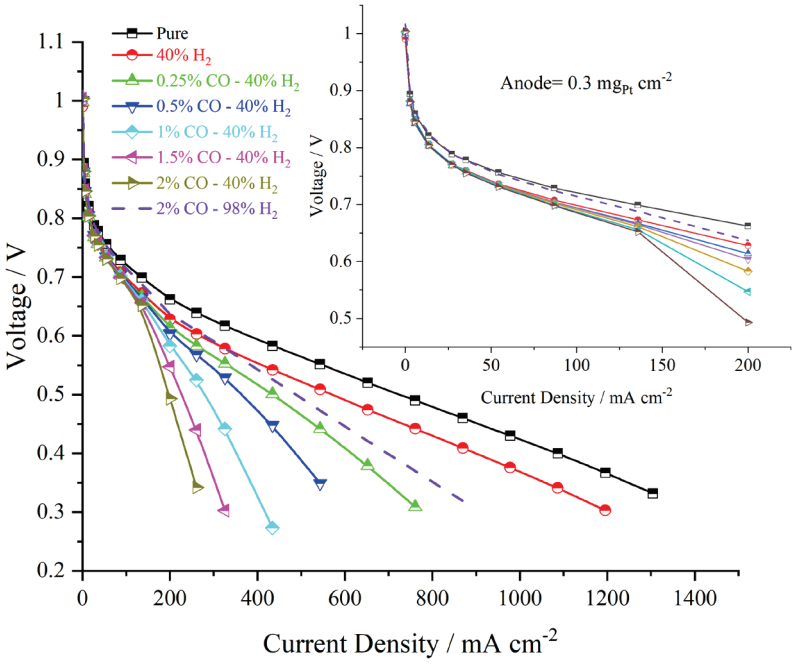

Figure 3.3 I-V curves of HT-PEMFCs with anodes of a fixed Pt loading of 0.3 mgPtcm-2. The anode feeding gas includes 100% H2 and 40%H2 with a variety of CO contents from 0.25 to 2.0%CO, as indicated in the figure. T = 160oC, λ_{H2} = 1.5 and λ_{Air} = 2.0 at current densities > 200 mA cm^{-2}.

3.2.6 Effect of hydrogen dilution

To summarize the discussion above the two effects of the hydrogen dilution and CO poisoning are significantly exaggerated when the Pt loading is lowered. Figure 3.4

summarizes the inert gas dilution effect of the anode performance of HT-PEMFCs at varied Pt loadings of the anode.

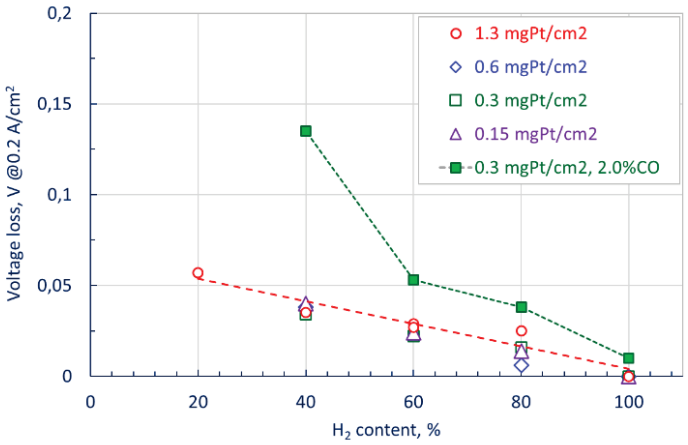

Figure 3.4 Cell voltage losses at 0.2 mA cm^{-2} due to the hydrogen dilution in the absence of CO as well as the presence of 2.0% CO. data were obtained from I-V curves measured at 160ºC with anodes of varied Pt loadings as indicated in the figure.

In the absence of CO, the hydrogen dilution by an inert gas e.g. nitrogen or argon causes anode performance losses. Switching from 100% H_2 to 60%H_2, for example, all four electrodes exhibited a lowered performance by ca. 25 – 30 mV, which is not very sensitive to the Pt loading. When CO is present in the fuel steam, the combined effects on the hydrogen dilution and CO poisoning becomes substantial for the low Pt loading electrode. For anodes of 0.3 $mg_{Pt}cm^{-2}$, 2.0% CO in a 40% H_2 fuel stream can lead to an anode voltage loss as high as 130 mV.

3.2.7 CO Poisoning with varied Pt loading electrodes

The combination of the hydrogen dilution and CO poisoning can be expressed as the ratio [CO]/[H_2], which, in turn, determines the Pt surface coverage by CO and hence the fraction of the active sites available for the hydrogen oxidation. An expression of the Pt surface coverage is, however, a complicated function involving the dissociative adsorption of hydrogen and its competition with CO and other adsorptive species such as the dissociated water (-OH_{ad}) and the acidic anion ($H2PO4^-$) [21,104], though different models have been

suggested to correlate the CO coverage on the Pt catalyst surface [105,106]. A simplified correlation of the anode performance loss with the [CO]/[H2] ratio is presented in Figure 3.5. A strong dependence of the anode performance loss can be seen on the [CO]/[H2] ratio, in an exponential form, which has also showed clear trends with the Pt loading of the anode.

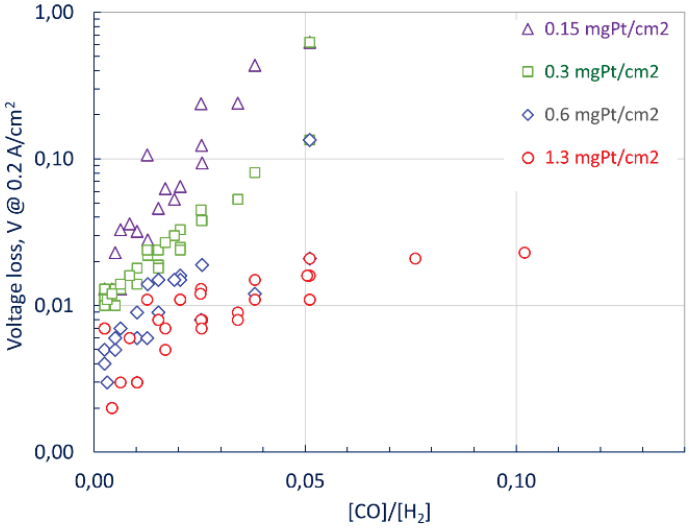

Figure 3.5 Cell voltage losses as a function of the [CO]/[H2] ratio due to the hydrogen dilution by in the absence of CO as well as presence of 2.0% CO. The data were obtained from the I-V curves at 0.2 mA cm^{-2} at 160 °C with anodes of varied Pt loadings as indicated in the figure.

3.3 Hydrogen oxidation kinetics in the absence and presence of CO

3.3.1 Introduction

The H_2 oxidation reaction (HOR) kinetics is very facile in acidic electrolytes, with Pt and Pd as the most active and stable catalysts [107]. In proton exchange membrane fuel cells (PEMFC), lowering the anode Pt loading from 0.4 to 0.05 $mg_{Pt}cm^{-2}$ was reported to give a cell voltage loss of only 5–15 mV at current density of 1.2 A/cm^2 [108] In high temperature PEMFCs based on acid doped polybenzimidazole membranes operating at 180°C, reduction of the anode Pt loading from 0.9 to 0.05 or even down further to 0.025 $mg_{Pt}cm^{-2}$ has shown negligible performance losses [93]. The author´s previous studies has shown

that anodes of platinum loading from 1.3 down to 0.15 mgPt/cm^2 leads no visible difference in the fuel cell performance.

Kinetically the HOR on Pt is assumed to proceed by either Tafel-Volmer or Heyrovsky-Volmer mechanisms. The Tafel-Volmer mechanism involves the potential-independent dissociative adsorption of hydrogen (the Tafel step) followed by the electrochemical oxidation of H ad-atoms in the Volmer step:

$$H_2 + 2Pt \leftrightarrow 2Pt\text{-}H_{ads} \qquad \text{Tafel step} \qquad (3.1)$$

$$2Pt\text{-}H_{ads} \leftrightarrow 2Pt + 2H^+ + 2e^- \qquad \text{Volmer step} \qquad (3.2)$$

The Heyrovsky-Volmer mechanism involves the electrochemical formation of adsorbed hydrogen atoms, which is also followed by the above Volmer step:

$$H_2 + 2Pt \leftrightarrow Pt\text{-}H_{ads} + H^+ + e^- \qquad \text{Heyrovsky step} \qquad (3.3)$$

Either the Tafel or the Heyrovsky step is the rate determining step while the Volmer reaction is a facile charge transfer step. Early year studies on the HOR kinetics were conducted using rotating disk electrodes (RDE) in liquid electrolytes. As a result of the extremely fast electrode kinetics, estimation of the ohmic and mass-transport contributions to the polarization is crucial for the studies. Kinetic parameters for the HOR i.e. the exchange current density (i^o in A/cm$^2_{Pt}$) and its corresponding activation energy (E_a in kJ/mol) as well as the Tafel slope, have been evaluated using on single or polycrystalline Pt electrodes [106,109–111] reporting an exchange current density of about 1 mA/cm$^2_{Pt}$ and a Tafel slope of 28–30 mV/decade. These results are however inaccurate [112–114] due to the effect of the slow hydrogen mass transport rate in liquid electrolytes.

To improve the measurements of the HOR, as well as the hydrogen evolution reaction (HER) kinetics, it is desired that the kinetic voltage losses is significant while both the ohmic and mass transport contributions are minimized. This has been achieved by using gas diffusion electrodes (GDE) with ultralow Pt loading [115,116] where the mass transport contribution is negligible. Using a hydrogen pump cells and ultralow Pt loading GDE exchange current densities for HOR on carbon supported Pt nanoparticles have been reported to be in a range of 100-800 mA/cm$^2_{Pt}$, i.e. 2-3 orders of magnitude higher than the previously report values.

The HOR studies have so far been conducted in LT-PEMFCs at temperatures of up to 80°C. In this project, the study was extended to HT-PEMFCs to a temperature range from 120 to 180°C by using phosphoric acid (PA) doped polybenzimidazole (PBI) membranes. Further studies to the HOE kinetics in the presence of carbon monoxide have also been performed.

3.3.2 Hydrogen pumping approach with asymmetric Pt loading electrodes

A key to a successful study of the HOR kinetics is to use GDE with ultralow Pt loading. In the present work the used Pt loading of the working electrode is between 1.5 to 6.5 μgPt/cm^2. In this way the emphasis was placed on the kinetic contribution to the measured polarization.

Another trick of the measurement is the hydrogen pumping approach, i.e. a cell performing hydrogen oxidation on one electrode and hydrogen evolution on the other. In this way, the kinetically sluggish oxygen reduction reaction is avoided and the kinetics of HOR and HER can be simultaneously studied by a single measurement. Without a full fuel cell reaction to take place, some humidification of the hydrogen gas is needed in order to avoid the drying out of the membrane during the study at temperatures of 120-180 °C.

Use of asymmetric Pt loading electrodes is another key. To ensure the uniform catalyst layer thickness and good catalyst dispersion, such electrodes are prepared using diluted Pt/C catalysts down to 2.3 wt% Pt/C. The used count and reference electrode has a Pt loading of 1.3 mgPt/cm2, a practical value for industrial fuel cell electrodes. This electrode exhibits negligible polarization on the count/reference electrode side, which enable the attribution of the measured electrode polarization to the working electrode. The same technique is used for the HOR kinetics study in the presence of CO.

3.3.3 Polarization curves for hydrogen pumping and Butler–Volmer fitting

A set of polarization curves obtained with a working electrode of 6.5 μgPt/cm^2 at 120-180°C is shown in Figure 3.6a. The ohmic resistance is corrected using the high frequency resistance from the impedance measurement. In order to minimize the effect of limiting current densities on the kinetic analysis, only data points with current densities of less than 10% of the corresponding limiting current density were used for fitting, which corresponds to an overvoltage range of 30-50 mV.

To describe the HOR/HER kinetics and to estimate the kinetic voltage loss for gas diffusion electrodes, a Butler–Volmer equation was used:

$$i = i^{o}_{Geo} \cdot (\exp\frac{\alpha_a F\eta}{RT} - \exp\frac{-\alpha_c F\eta}{RT}) \quad (3.4)$$

where i^o is the exchange current density based on geometric electrode surface area in A/cm^2_{Geo}, α_a and α_c are the anodic and cathodic transfer coefficients, respectively. The Tafel slope, b, is defined as b = 2,303RT/αF. A constraint for $\alpha_a+\alpha_c$ =1 is applied for the fitting, hinting an assumption that the Tafel-Volmer mechanism is predominant. Figure 3.6b shows the Tafel plots for the HER/HOR polarization curves.

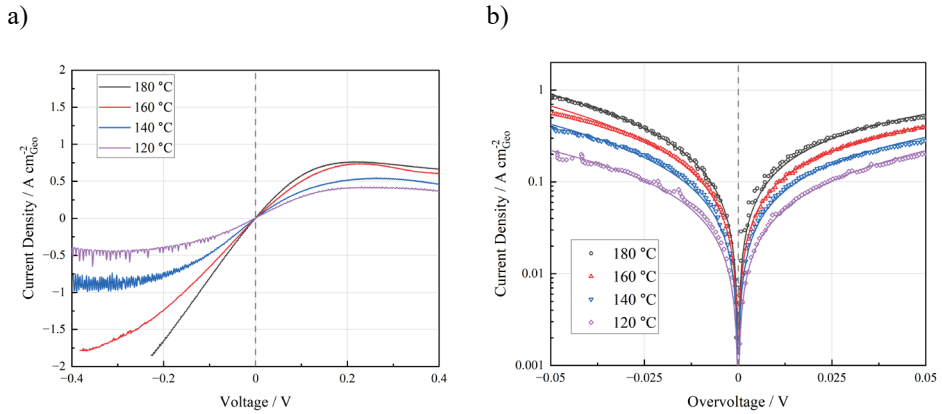

Figure 3.6 a) HOR and HER polarization curves for electrodes with 6.5 $\mu g_{Pt}/cm^2_{Geo}$ at 120-180°C; b) Tafel plots of the same sets of data and their fit to the Butler–Volmer equation (lines)

3.3.4 Arrhenius plot and activation energy

Figure 3.7 shows the Arrhenius plots of the exchange current density i^0 versus (1/T) for two electrodes of low Pt loadings. As seen from the figures the data follow straight lines in the Arrhenius plot, based on which the activation energy, E_a, was estimated over the temperatures range from 120 to 180 °C using the flowing equation:

$$\frac{\partial \log(i^o)}{\partial(1/T)} = -\frac{E_a}{2.303R} \quad (3.5)$$

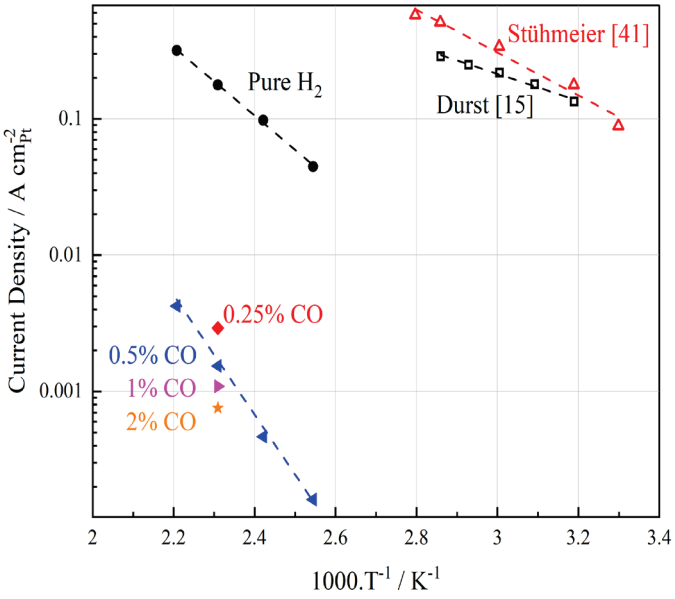

Figure 3.7 Arrhenius plots for HOR/HER exchange current densities in the absence and presence of carbon monoxide. Data were obtained in high temperature polymer electrolyte cells operating under the hydrogen pumping mode. Two sets of data from literature for pure hydrogen in the low temperature region are presented for comparison.

Table 3.2 summarizes the results. Previous studies have determined the HOR/HER kinetics by the same H_2-pump approach however, with PFSA membranes at typical temperatures of up to 80°C. It can be seen that the obtained i^0 value varied from 200 to 500 mA/cm^{2}Pt. In this comparison the results presented in this paper are slightly lower. A possible reason might be due to the electrolyte. Polymeric electrolytes based on perfluorosulfonic acid e.g. Nafion are super strong acids with pK_a of ca. -14 while phosphoric acid is mild acid with a pK_a of 2.16, The significant difference in the proton activity may affect the HOR/HER kinetics. Water vapor pressure or the atmospheric humidity in the test cell may also play a role when hydrogen is fully (100%) humidified for the low temperatures cell test while in

the present work only hydrogen on the count/reference electrode side was humidified to a water vapor partial pressure of 0.19 bar, corresponding to a relative humidity of 3 at 160°C.

Table 3.2 Summary of exchange currents densities and Tafel slopes as well as activation energy of the present study

Temperature oC	Fuel (H_2/CO)	Exchange current density i^o (mA/cm$^2_{Pt}$)	Tafel slope (mV/dec)		Activation energy E_a (kJ/mol)	Ref.
			b_{HOR}	b_{HER}		
120°C	100/0	44.6	70	65		
140°C	100/0	97.8	209	43		
160°C	100/0	177.4	186	46	49.6	
180°C	100/0	317.4	-	40		This work
160°C	99.75/0.25	2.9	1381	38		
160°C	99.5/0.5	1.5	340	42	-	
160°C	99.0/1.0	1.1	207	45		
160°C	98.0/2.0	0.76	233	44		
80°C	100 (Nafion)	200-600	-	-	-	[115]
80°C	100 (Nafion)	240	-	-	16	[113]
80°C	100 (Nafion)	520	-	-	20	[117]

3.3.5 HOR/HER kinetics in the presence of CO

Figure 3.8 shows the HER/HOR polarization curves for pure hydrogen and hydrogen containing CO from 0.25 to 2.0 % at 160°C. For pure hydrogen the polarization curves is slightly asymmetric, with an increased limiting current density for HER. In the present work the mass transport effect has not been compensated, which may lead to additional polarizations at high current densities. For HER reactions, the shielding effect of the catalyst sites by the hydrogen evolution reactions have been considered for the asymmetric behavior of the HOR/HER polarization. This might be an issue in liquid electrolytes but,

as pointed out by Durst et al. [113] probably not the case in polymer electrolytes. In the present work at temperatures of above 100ºC, this can hardly be a major reason. The most likely explanation is the change of the electrode reaction mechanism i.e. a rate limitation imposed by the Tafel reaction.

As shown by Stühmeier et al. [117] increase in the partial pressure of hydrogen from 100 to 450 kPa leads to significant improvement of the HOR kinetics while the HER kinetics improves only slightly. As a result, the Tafel plots for HER/HOR become much more symmetrical. These observations are in good agreement with the assumption of a Tafel-limitation at high overpotentials. Increase in the hydrogen partial pressure improves the dissociative adsorption of hydrogen, i.e. the Tafel step (3.6).

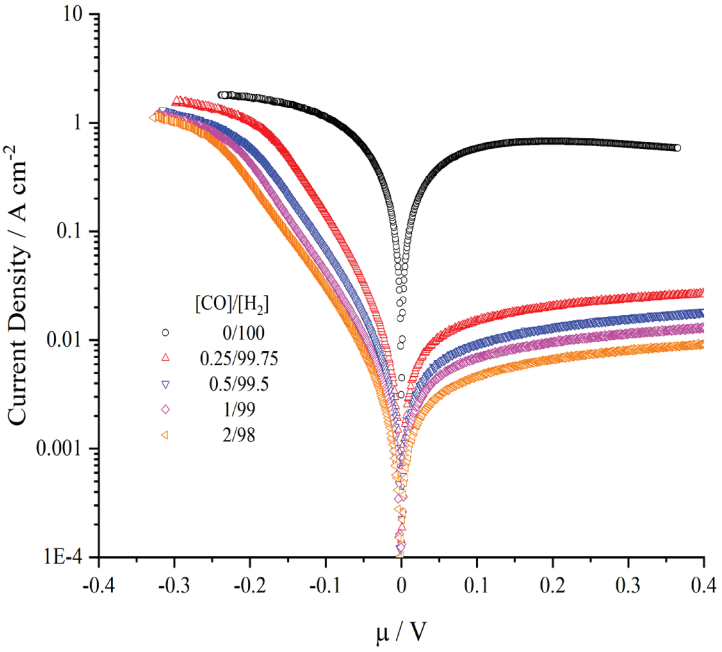

Figure 3.8 I-V curves for HOR and HER at 160ºC in the presence of CO. The CO/H_2 ratios are indicated in the figure where 0/100 was for pure hydrogen. The working electrode loading was of 6.5 μgPt cm^{-2}

In the presence of CO, the strong adsorption of CO on the surface of Pt catalysts hinders the HOR kinetics due to the limitation of slow dissociative hydrogen adsorption (Tafel step), while the associative hydrogen desorption does not seem to limit the HER in the studied potential range.

The presence of CO in the hydrogen stream results in a significant decrease in the HOR current. At an overpotential of 0.1 V, the HOR kinetic current density was decreased from 600 mA/cm^2 for pure hydrogen to 2.9 mA/cm^2 at the CO concentration of 0.25%, and further down to 1.5, 1.1 and 0.76 mA/cm^2 for 0.5, 1.0 and 2.0%CO, respectively. In term of exchange current densities of HOR the presence of CO at a concentration of 0.25-2.0% results in a decrease of i^o by about 2 orders of magnitude, as seen from Figure 3.7.

3.4 Potential Cycling Test of HT-PEMFCs

3.4.1 Introduction

The durability of HT-PEMFCs has been recognized as the most critical issue to be addressed before widespread commercialization of the technology. Major mechanisms of degradation of fuel components include the loss of doping phosphoric acid, polymer oxidation and membrane thinning and platinum nanoparticle growth and hence active surface area decrease, as recently reviewed [9].

Catalyst degradation is due to the steady loss of the active surface area by physical and electrochemical Ostwald ripening of platinum nanoparticle [47]. The electrochemical dissolution of Pt in acidic electrolytes can be a direct dissolution of the metal:

$$Pt \rightleftarrows Pt_2 + 2e^- \qquad E(V) = 1.19\ V + 0.029\ V \cdot \log[Pt^{2+}] \tag{3.7}$$

or via formation of the surface oxide:

$$Pt + H_2O \rightleftarrows PtO + 2H^+ + 2e^- \qquad E(V) = 0.98\ V - 0.59\ V \cdot pH \tag{3.8}$$

$$PtO + H_2O \rightleftarrows PtO_2 + 2H^+ + 2e^- \quad E(V) = 1.05\ V - 0.59V \cdot\ pH \tag{3.9}$$

Followed by chemical or electrochemical dissolution:

$$PtO + 2H^+ \rightleftarrows Pt^{2+} + H_2O \qquad \log\left[Pt^{2+}\right] = -7.06 - 2pH \tag{3.10}$$

$$PtO_2 + 4H^+ + 2e^- \rightleftarrows Pt^{2+} + H_2O \tag{3.11}$$

$$E(V) = 0.834\ V - 0.118\ V \cdot pH - 0.029V \cdot \log\left[Pt^{2+}\right]$$

The solubility of Pt changes with a number of factors such as the electrode potential, type and pH of electrolytes, and temperature. The dissolved Pt ions may be reduced hydrogen permeated from the anode [118] resulting in the formation of the so called Pt band [119].

In concentrated phosphoric acid at elevated temperatures, a strong dependence of the platinum surface area loss on the electrode potential, especially above 0.70 V, was observed [49], likely via combined mechanism of agglomeration/sintering and Ostwald ripening [50]. It has been reported that the Pt solubility increased by three orders of magnitude as the electrode potential is lifted from 0.8 to 1.0 V vs RHE [51] while the Pt dissolution rate increased by 9 orders of magnitude when the potential was swept from 0.6 to 1.0 V vs. RHE [120]. For PBI cells, the PA content in the membrane is limited. Using the PA inventory numbers of 20-40 $mgcm^{-2}$ it is estimated that the dissolution of the platinum catalyst under OCV can be up to 2-5% of the total catalysts with the loading of 0.5-1.0 $mg_{Pt}\ cm^{-2}$ in a cathode [3].This number may have significant impacts on the catalyst degradation particularly under the potential cycling mode.

Load cycling studies in literature can be divided into low load (0-0.4 A cm^{-2}) and high load (0.4-1.0 A cm^{-2}) levels. The high load cycling involves cell operation in the low voltage range, without exposure of the cell to OCV [121]. The main mechanism for the performance degradation under this mode is the PA loss, which eventually results in membrane degradation e.g., decreased proton conductivity. The membrane degradation, as characterized by the hydrogen crossover or OCV observation, is, however, not always detectable during the short timeframe of the load cycling test.

The low load cycling, on the other hand, involves high cell voltages. The major degradation mechanism is the catalyst or electrode degradation. At zero current, i.e. during idling of a fuel cell, the cell is exposed to OCV, where severe carbon corrosion and platinum nanoparticle aggregation occur [27,62] Platinum catalyst dissolution, more precisely, the formation and dissolution of the metal surface oxide, is intensified during the low load cycling. The OCV hold is the most destructive stressor of the operating conditions. An exposure of a fuel cell to OCV was reported to exhibit a voltage degradation of over 400 $\mu V\ h^{-1}$, showing significant increases in both the activation and mass transport resistance as well as a reduction of the cathode elctrochemically active surface area (ECSA) [75]. Compared to the fresh electrode, a significant increase of the Pt nanoparticle size of the cathode after OCV exposure was reported [68]. To avoid exposure to OCV (0 A cm^{-2}) some potential cycling studies were conducted to apply a small current density e.g., 0.04 A cm^{-2} [122]or 0.05 A cm^{-2} [123] where the exact cell voltage at the high end is unknown.

The present work is devoted to a study of the low load cycling, with well controlled yet systematically tailored voltage range. It is noted that for the low load or high potential cycling at near OCV, there is little water formation inside the fuel cell. For prolonged tests, the effect of atmospheric humidity on the PA dehydration should be taken into account.

3.4.2 Potential profile of the cycling test

Figure 3.9 shows the cell voltage profile i.e. square waves applied to the corresponding MEAs during potential cycling tests. These tests were conducted while maintaining a constant temperature of 160 °C, flow rate of gases, and an upper potential value of 0.95 V. MEAs M08-05, M07-05, and M65-05 were subjected to an investigated lower potential value of 0.8 V, 0.7 V, and 0.65 V, respectively. The cycling for these MEAs was conducted with a 5-seconds upper potential and a 5-seconds lower potential. The effect of cycling duration was studied with MEAs M07-30 and M07-60, where the lower potential limit was set to 0.7 V. The duration at potential limits was varied from 30 seconds to 1 minute.

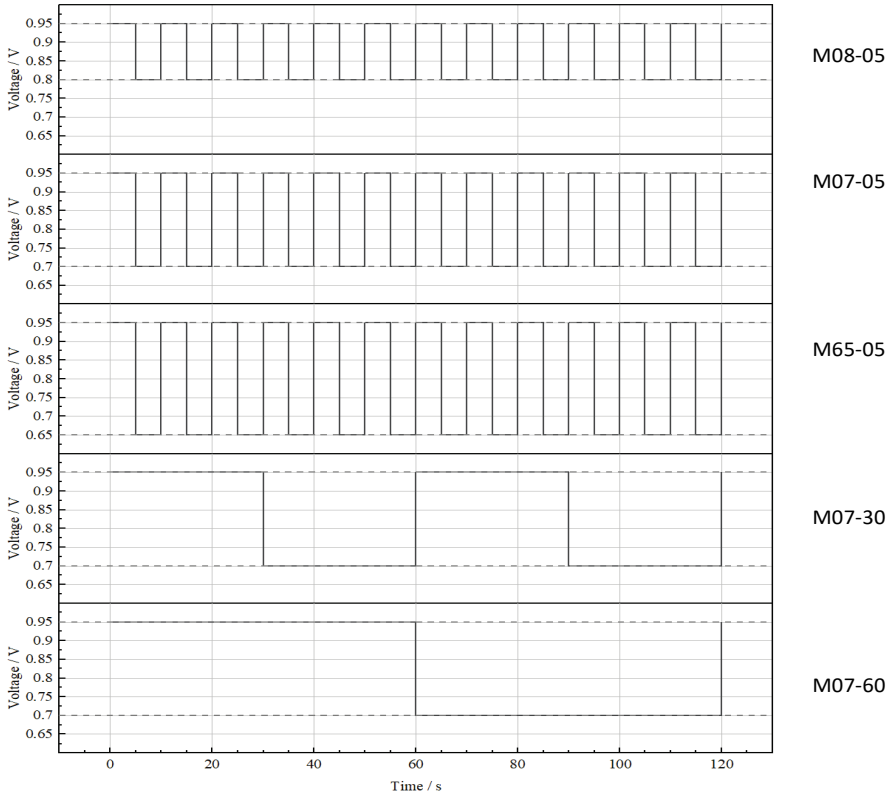

Figure 3.9 Voltage profiles for the potential cycling test with MEAs named to the right

MEAs M08-05, M07-05, and M65-05 underwent a total of 30,000 potential cycles, divided into four parts at 5,000, 10,000, 20,000, and 30,000 cycles, while MEA M07-30 underwent a total of 10,000 potential cycles, split into two parts at 5,000 and 10,000 cycles. MEA M07-60, on the other hand, underwent only one part consisting of 5,000 cycles. After each part, the MEAs were relaxed at 0.4 A cm^{-2} for an hour before recording a polarization curve. This procedure resulted in a total of 5 polarization curves for M08-05, M07-05, and M65-05, 3 polarization curves for M07-30, and 2 polarization curves for M07-60, including the BOL polarization curves. Moreover, the electrochemical impedance spectroscopy was performed on the MEAs after the each polarization curve.

3.4.3 Analysis of I-V curves and iR correction

The following equation is often used to fit experimentally obtained polarization curves for fuel cells:

$$E_{Cell} = E_{rev} - h_{ORR} - iR - \eta_{mt} \quad (3.12)$$

Here E_{rev} is the reversible cell voltage, R is the total ohmic resistance, η_{ORR} the cathode activation loss and η_{mt} the mass transport loss.

The reversible cell voltage is a function of temperature and pressures of hydrogen and oxygen and can be expressed as:

$$E_{rev} = 1.23 - 9 \cdot 10^{-4}(T - 298) + \frac{2.303\ RT}{4F} \times \log\left[P_{H_2}^2 P_{O_2}\right] \quad (3.13)$$

where $P_{H_2}^* = P_{O_2}^* = 1$ bar are the reference pressure of hydrogen and oxygen. In HT-PEMFC no humidification is applied for either hydrogen or air. At the anode side P_{H2} = 1 bar is assumed by neglecting any water diffused from the cathode chamber. At an air stoichiometry of λ_{Air} = 2.0, the water generation in the cathode chamber corresponds to a water vapor pressure of ca. 0.19 bar, which gives an oxygen partial pressure of ca. 0.17 bar. Based on these numbers and using equation (8) the reversible cell voltage of an HT-PEMFC at 160 °C is estimated to be E_{rev} = 1.1 V, as indicated in Figure 3.10a.

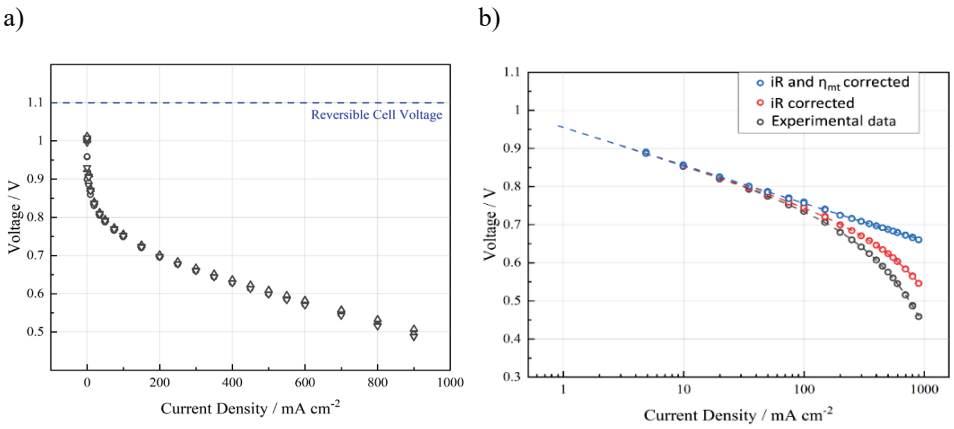

Figure 3.10 . a) Polarization curves of typical BoL performances at 160 oC operating with dry hydrogen and air under ambient pressure and stoichiometries of 1.5 and 2.5, respectively. b) Tafel plot of as measured, iR- as well as iR & η_{mt} corrected data.

As seen from the figure the measured I-V curves are in the linear region, which indicates that the mass transport overpotential, if any, has a ohmic behaviour. In the following fit it

is assumed that the mass transport overpotential is included in the Ohmic term and the following simple equation is used:

$$E_{Cell} = E_{rev} - h_{ORR} - i \cdot \sum R \quad (3.14)$$

Figure 3.10b shows the fitting results for MEA M07-05. Based on the high frequency resistance (HFR) from EIS measurements the iR-corrected I-V curve still shows deviation from the Tafel linearity at current densities above, say, 50 mA/cm^2. A significant contribution of the mass transport loss, though appearing ohmic, is obtained from the fitting. The mass transport loss is sensitive to the limiting current density, which is always poorly defined compared to the kinetic (logarithmic) and ohmic terms. It is therefore often practically determined by subtraction of the ohmic (HFR) and kinetic losses from the as measured i-V curves. As seen from Figure 4b, the contribution of the mass transport term is of the value as the ohmic loss in the low to intermediate current range and becomes significantly larger at higher current densities.

The experimental and fitting results are summarized in Table 3.3. First of all MEAs exhibit high BoL OCVs and after 30 k cycles no changes in the OCV were observed, indicating little membrane degradation has occurred. The ohmic loss term in the table was estimated from the HFR, which, in fact, has changed to a very limited extent (3-5%) during the cycling test, confirming the observed little membrane degradation. It should be noted that, during the potential cycling, the cell suffered from the membrane drying due to the fact that the very low operating current densities led to little water formation. It is therefore that, after a certain period the potential cycling was stopped at cycle numbers of 5, 10, 20 and 30 k, after which the cell was operating at a constant load (400 mA/cm^2) for an hour in order to restore the membrane performance. All the EIS measurements were conducted after the membrane wetting restoration.

Also the Table 3.3 lists the mass transport loss from fitting during the cycling period, a significant increase in the mass transport loss was observed at the EoL. Apparently the potential cycling has resulted in significant carbon corrosion or/and degradation in the electrode hydrophobicity, as to be discussed below. The cell performance in term of kinetic loss, i.e. the cell voltage after both iR and mass transport correction, is listed in the last

column of the table. In the following discussion of the catalyst degradation, cell voltage data after the ohmic and mass transport correction are used

Table 3.3 Summary of the potential cycling tests

MEAs	Cycling mode E(V)/Time (s)	OCV (V) BoL/EoL*	Ohmic loss (HFR, mΩ cm^2) Bol/EoL*	Fitting mass transport loss (mΩ cm^2) Bol/EoL*	Cell performance** E(V) @ (0.2 A/cm^2) Bol/EoL*
M08-05	0,95/5 + 0.8/5	1.01/1.020	96.2/98.9	108.8/241	0.738/721
M07-05	0,95/5 + 0.7/5	0.96/0.94	101.4/106.2	105.6/160.8	0.736/714
M65-05	0,95/5 + 0.65/5	1.01/1.03	98.1/102.1	83.9/125.9	0.738/708
M07-30	0,95/30 + 0.7/30	0.99/0.97	106.3/-	-/-	0.696/0.67
M07-60	0,95/60 + 0.7/60	1.03/1.01	99 /-	-/-	0.694/0.629

* BoL is defined as the time when break-in was completed while the EoL was after 30 k cycles.

** The cell performance was based on data after the iR and mass transport correction

3.4.4 Degradation in varied potential cycling range

Three MEAs were studied by varying the potential range of cycling from 0.9-0.8 V (M08-05), 0.9-0.7 V (M07-05) and 0.9-0.65 V (M65-05) at a fixing time frame of 5 s up and 65 s down. The cycling was stopped at 5, 10, 20 and 30 K cycles and I-V curves were recorded. After the iR and mass transport correction, the polarization curves at the Bol and Eol (30 K cycles) are shown in Figure 3.11a. A steady decrease in the cell performance was observed and the decrease was in the order of low end potentials from 0.8 to 0.65 V. Specific cell voltages at current densities of 0.2 and 0.6 A/cm^2 were collected and plotted as a function of the cycling numbers, as shown in Figure 3.11b. In the figure, the points at cycle number of zero are the performance at the Bol. The steady decrease in the cell voltage was better seen. During the first 5 K cycle the cell voltage decrease at 0.2 A/cm^2 was

observed of 12 mV for M08-05, 14 mV for M07-05 and 38 mV for M65-05, which were increased to 17, 24 and 29 mV at the end of 30 K cycles, respectively. These results will be discussed in the next section.

a) b)

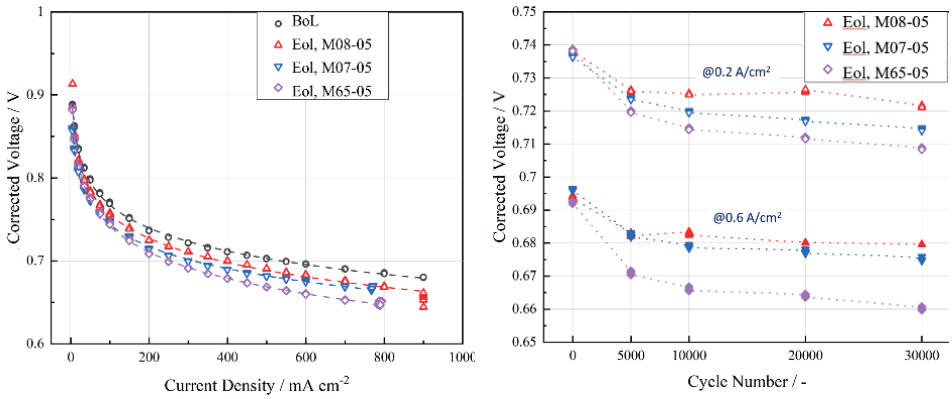

Figure 3.11 Polarization curves (a) and cell voltage at 0.2 and 0.6 A/cm2 (b) after the ohmic and mass transport correction for three cycling range of the potential as indicated in the figure.

3.4.5 Degradation in varied potential cycling range

Another test was made by fixing the potential scan range from 0.9 to 0.7 V but varying the hold during at each potential, from 5/5 (M07-05) to 30/30 (Mo7-30) to 60/60 (M07-60) sec. The ohmic and mass transport corrected cell voltages of the three MEAs are expressed in relation to their Bol performance and plotted against the cycle number and total operation time in Figure 3.12. Of the three MEAs M07-05 has been subjected to 30 K cycles while M07-30 to 10 K cycles and M07-60 to 5 K cycles. In term of the total time, M07-05 has been subjected to an operation for 80 hours while M07-30 and Mo7-60 for 160 hours. As seen from Figure 3.12a, in term of cycle numbers, the extended duration at each potential hold step led to increased performance degradation, i.e. in the order M07-60, M07-30 and M07-05. It is also seen that a sharp decrease in the cell performance (ca. 2%) in the first 5 K cycles, followed by a flat plot, particularly for M07-05.

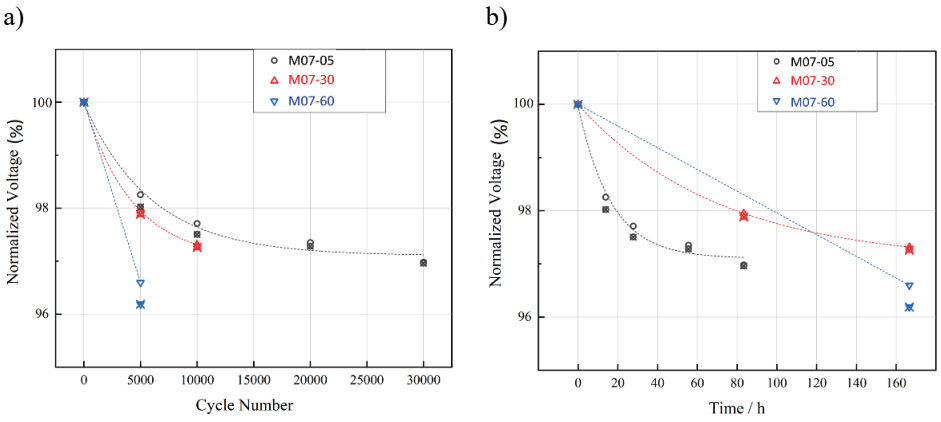

Figure 3.12 Normalized cell voltage relative to the BoL performance as a function of cycle number (a) and of operation time (b) at current density of 0.2 A/cm$^{2.}$ The voltage was corrected after the ohmic and mass transport losses. The three MEAs were subjected to potential cycling between 0.9 and 0.7 V for hold duration of 5/5 (M07-05), 30/30 (M07-30) and 60/60 (M07-60) sec.

3.4.6 Catalyst degradation mechanisms

The cycling studies of the present work has a fixed high potential end hold at 0.9 V. At this potential, carbon corrosion and platinum oxidation would occur in a similar way for the five MEAs. Carbon corrosion in concentrated phosphoric acid has been a subject of studies in connection to phosphoric acid fuel cells [124]. The work by Oh et al. [125] focused on PBI cells, showing limited carbon corrosion at cell potentials below 1.1 V for short terms. Long-term durability test for up to 18,000 hr at 150^{o}C and 0.2 A/cm^{2}, on the other hand, has observed significant thinning of the catalyst layer [33]. The SEM images of cross sections of fresh and three MEAs after 30 K cycles (Figure 3.12) show no visible thinning of the catalyst layers. On the other hand, a significant increase in the mass transport loss was observed for all the testing cells, which was therefore attributed to the degradation of the hydrophobicity of the catalyst layers.

4. CONCLUSIONS

HT-PEMFCs are a type of fuel cell that operates at temperatures above 100 °C. This technology is particularly effective in mitigating the effects of fuel impurities, such as CO poisoning, which allows for the use of reformate hydrogen from a simple methanol reformer without additional CO clean-up. The research and development efforts in the field of HT-PEMFCs have been extensive, with significant challenges still remaining in improving the cell performance and long-term durability. This thesis focused on experimental investigations of the anode performance in the presence of fuel impurities, such as CO, and catalyst degradation under dynamic potential cycling.

Experimental investigations were carried out to study the CO tolerance of HT-PEMFCs at the typical operating temperature of 160 °C. The investigation specifically focused on the effects of CO poisoning in hydrogen-rich reformate fuels, where a considerable amount of inert gas components are present, causing hydrogen dilution.

The small poisoning effect by up to 2% CO in pure hydrogen is verified with electrodes of 1.3 mg_{Pt}/cm^2, showing a voltage loss of ca. 12 mV at 0.2 A/cm^2. On the other hand, the hydrogen dilution by an inert gas (e.g. N_2 or Ar) in the absence of CO is found to deteriorate the anode performance. Switching from 100% to 60%H_2 leads to a lowered performance by ca. 25 – 30 mV. Under a constant H_2 stoichiometry (λ_{H2} = 1.5) the fuel cell performance degradation caused by 1.0% CO is found to be intensified by the hydrogen dilution in a range of 20 – 80 vol% H_2. A major contribution to the anode performance loss is found to be from the H_2 dilution. For H_2 dilution of 40 and 60 vol% an increase in the CO concentration from 0.5 up to 2.0 vol% triggered negligible voltage losses i.e. less than 1% at an operational current density of around 0.2 A/cm^2.

The study is then extended to the low Pt loading electrodes for the evaluation of the performance with reformate fuels. It is found that both the H_2 dilution by inert gas components and CO poisoning effects are significantly increased for electrodes with low Pt loadings. The number of active sites on the catalysts is reduced, which makes the low Pt loading electrode much more sensitive to CO poisoning. When using anodes with a low Pt loading of 0.3 mg_{Pt}/cm^2, 2.0% CO in a 40% H_2 fuel stream resulted in an anode voltage loss as high as 130 mV. This combined effect is well correlated to the ratio $[CO]/[H_2]$,

which in turn determines the Pt surface coverage by CO and hence the fraction of the active sites available for the hydrogen oxidation. A strong dependence of the anode performance loss on the [CO]/[H_2] ratio is found to be in an exponential form, which is highly related to the Pt loading of the electrode. The finding of increased poisoning effect by the hydrogen dilution and low Pt loading CO poisoning is of importance for the low Pt loading anodes, which should be assessed under scenarios of utilizing reformate fuels containing CO.

Also in connection to the CO poisoning effect, the hydrogen oxidation and evolution reaction kinetics was studied in a temperature region from 120 to 180 °C without and with the presence of carbon monoxide. The study was conducted in a hydrogen pumping cell mode using gas diffusion electrodes with a platinum loading of 1.5-6.5 μgPt/cm^2. Fitting with the Butler–Volmer equation obtained an HOR/HER exchange current density of 200 to 500 mA/cm^2 based on the electrochemically active surface area of platinum. These numbers are comparable to those obtained at 40-80 °C in perfluorosulfonic acid electrolytes. The activation energy in a temperature range from 120 to 180 °C is found to be 49.6 kJ/mol. It is shown that the HOR, but not the HER, rate is limited by the Tafel step.

In the presence of CO, severely asymmetric Tafel plots for HER/HOR are observed. The strong adsorption of CO on the Pt surface hampers the HOR kinetics by further limiting the slow dissociative hydrogen adsorption. The presence of CO at a concentration of 0.25-2.0% resulted in a decrease of the HOR exchange current density by about 2 orders of magnitude.

A study of the HT-PEMFC performance degradation stressed by potential cycling is carried out with fixed upper potential limit (0.95 V) but varied low end potentials (from 0.8 to 0.65 V) and hold durations (from 5 to 60 sec). In all tested cells, little degradation of the membrane, in terms of ohmic resistance and open circuit voltage was observed apparently due to the overall short time of the fuel cell operation. A significant performance loss was concluded due to the mass transport loss, attributable to the degradation of the hydrophobicity of the electrode.

A major catalyst degradation mechanism is the platinum particle growth via the electrochemical Ostwald ripening. The dissolution of Pt and surface oxides during the upper potential hold (0.95 V) is governed by the Pt solubility in phosphoric acid. An important finding is that, in HT-PEMFCs the amount of the doping acid in the electrolyte

membrane is small (ca. 20 mg/cm^2), which limits the dissolution of Pt. The ripening is proposed to be limited by the low-end potentials and the hold duration (from 5 to 60 sec) where the reduction and re-deposition of platinum onto larger particles occur.

5. REFERENCES

[1] B.G. Pollet, S.S. Kocha, I. Staffell. Current status of automotive fuel cells for sustainable transport, *Current Opinion in Electrochemistry* 16, 90–95, 2019. DOI:10.1016/j.coelec.2019.04.021.

[2] Q. Li, J.O. Jensen, R.F. Savinell, N.J. Bjerrum. High temperature proton exchange membranes based on polybenzimidazoles for fuel cells, *Progress in Polymer Science (Oxford)* 34, 449–477, 2009. DOI:10.1016/J.PROGPOLYMSCI.2008.12.003.

[3] D. Aili, D. Henkensmeier, S. Martin, B. Singh, Y. Hu, J.O. Jensen, L.N. Cleemann, Q. Li. Polybenzimidazole-Based High-Temperature Polymer Electrolyte Membrane Fuel Cells: New Insights and Recent Progress, *Electrochemical Energy Reviews* 3, 793–845, 2020. DOI:10.1007/s41918-020-00080-5.

[4] J.S. Wainright, J.-T. Wang, D. Weng, R.F. Savinell, M. Litt. Acid-Doped Polybenzimidazoles: A New Polymer Electrolyte, *Journal of The Electrochemical Society* 142, L121–L123, 1995. DOI:10.1149/1.2044337.

[5] D. Aili, J. Yang, K. Jankova, D. Henkensmeier, Q. Li. From polybenzimidazoles to polybenzimidazoliums and polybenzimidazolides, *Journal of Materials Chemistry A* 8, 12854–12886, 2020. DOI:10.1039/d0ta01788d.

[6] L. Vilčiauskas, M.E. Tuckerman, G. Bester, S.J. Paddison, K.D. Kreuer. The mechanism of proton conduction in phosphoric acid, *Nature Chemistry* 4, 461–466, 2012. DOI:10.1038/nchem.1329.

[7] A. Sannigrahi, D. Arunbabu, R. Murali Sankar, T. Jana. Aggregation behavior of polybenzimidazole in aprotic polar, *Macromolecules* 40, 2844–2851, 2007. DOI:10.1021/ma070049q.

[8] D. Zhang, L. Yan. Probing the acid-base equilibrium in acid-benzimidazole complexes by 1H NMR spectra and density functional theory calculations,

Journal of Physical Chemistry B 114, 12234–12241, 2010. DOI:10.1021/jp1054606.

[9] N. Seselj, D. Aili, S. Celenk, L.N. Cleemann, H.A. Hjuler, J.O. Jensen, K. Azizi, Q. Li. Performance Degradation and Mitigation of High Temperature Polybenzimidazole-based Polymer Electrolyte Membrane Fuel Cells, *Submitted to Chemical Society Reviews,* 2023.

[10] M. Shao, Q. Chang, J.P. Dodelet, R. Chenitz. Recent Advances in Electrocatalysts for Oxygen Reduction Reaction, *Chemical Reviews* 116, 3594–3657, 2016. DOI:10.1021/acs.chemrev.5b00462.

[11] L. Huang, S. Zaman, X. Tian, Z. Wang, W. Fang, B.Y. Xia. Advanced Platinum-Based Oxygen Reduction Electrocatalysts for Fuel Cells, *Accounts of Chemical Research* 54, 311–322, 2021. DOI:10.1021/acs.accounts.0c00488.

[12] A. Parthasarathy, S. Srinivasan, A.J. Appleby, C.R. Martin. Temperature Dependence of the Electrode Kinetics of Oxygen Reduction at the Platinum/Nafion® Interface-A Microelectrode Investigation, *Journal of The Electrochemical Society* 139, 2530–2537, 1992.

[13] S. Kaserer, K.M. Caldwell, D.E. Ramaker, C. Roth. Analyzing the influence of H3PO4 as catalyst poison in high temperature PEM fuel cells using in-operando X-ray absorption spectroscopy, *Journal of Physical Chemistry C* 117, 6210–6217, 2013. DOI:10.1021/jp311924q.

[14] S.K. Zecevic, J.S. Wainright, M.H. Litt, S. Lj Gojkovic, R.F. Savinell. Kinetics of O2 Reduction on a Pt Electrode Covered with a Thin Film of Solid Polymer Electrolyte, *Journal of The Electrochemical Society* 144, 2973–2982, 1997.

[15] Z. Liu, J.S. Wainright, R.F. Savinell. High-temperature polymer electrolytes for PEM fuel cells: Study of the oxygen reduction reaction (ORR) at a Pt-polymer electrolyte interface, in: Chem. Eng. Sci., 2004, pp. 4833–4838. DOI:10.1016/j.ces.2004.09.024.

[16] Z.-P. Wu, S. Shan, S.-Q. Zang, C.-J. Zhong. Dynamic Core–Shell and Alloy

Structures of Multimetallic Nanomaterials and Their Catalytic Synergies, *Accounts of Chemical Research* 53, 2913–2924, 2020. DOI:10.1021/acs.accounts.0c00564.

[17] C. Wei, R.R. Rao, J. Peng, B. Huang, I.E.L. Stephens, M. Risch, Z.J. Xu, Y. Shao-Horn. Recommended Practices and Benchmark Activity for Hydrogen and Oxygen Electrocatalysis in Water Splitting and Fuel Cells, *Advanced Materials* 31, 1806296–1806296, 2019. DOI:10.1002/ADMA.201806296.

[18] K.S. Lee, S.J. Yoo, D. Ahn, S.K. Kim, S.J. Hwang, Y.E. Sung, H.J. Kim, E. Cho, D. Henkensmeier, T.H. Lim, J.H. Jang. Phosphate adsorption and its effect on oxygen reduction reaction for PtxCoy alloy and Aucore-Ptshell electrocatalysts, *Electrochimica Acta* 56, 8802–8810, 2011. DOI:10.1016/j.electacta.2011.07.084.

[19] J.E. Lim, U.J. Lee, S.H. Ahn, E.A. Cho, H.J. Kim, J.H. Jang, H. Son, S.K. Kim. Oxygen reduction reaction on electrodeposited PtAu alloy catalysts in the presence of phosphoric acid, *Applied Catalysis B: Environmental* 165, 495–502, 2015. DOI:10.1016/j.apcatb.2014.10.042.

[20] H.Y. Park, D.H. Lim, S.J. Yoo, H.J. Kim, D. Henkensmeier, J.Y. Kim, H.C. Ham, J.H. Jang. Transition metal alloying effect on the phosphoric acid adsorption strength of Pt nanoparticles: An experimental and density functional theory study, *Scientific Reports* 7, 2017. DOI:10.1038/s41598-017-06812-w.

[21] Q. He, B. Shyam, M. Nishijima, D. Ramaker, S. Mukerjee. Mitigating phosphate anion poisoning of cathodic Pt/C catalysts in phosphoric acid fuel cells, *Journal of Physical Chemistry C* 117, 4877–4887, 2013. DOI:10.1021/jp309282n.

[22] S.H. Eberhardt, F. Marone, M. Stampanoni, F.N. Büchi, T.J. Schmidt. Operando X-ray Tomographic Microscopy Imaging of HT-PEFC: A Comparative Study of Phosphoric Acid Electrolyte Migration, *Journal of The Electrochemical Society* 163, F842–F847, 2016. DOI:10.1149/2.0801608jes.

[23] N. Bevilacqua, M.G. George, S. Galbiati, A. Bazylak, R. Zeis. Phosphoric Acid Invasion in High Temperature PEM Fuel Cell Gas Diffusion Layers, *Electrochimica Acta* 257, 89–98, 2017. DOI:10.1016/j.electacta.2017.10.054.

[24] S. Martin, Q. Li, T. Steenberg, J.O. Jensen. Binderless electrodes for high-temperature polymer electrolyte membrane fuel cells, *Journal of Power Sources* 272, 559–566, 2014. DOI:10.1016/j.jpowsour.2014.08.112.

[25] S. Martin, P.L. Garcia-Ybarra, J.L. Castillo. Ten-fold reduction from the state-of-the-art platinum loading of electrodes prepared by electrospraying for high temperature proton exchange membrane fuel cells, *Electrochemistry Communications* 93, 57–61, 2018. DOI:10.1016/j.elecom.2018.06.007.

[26] S. Martin, Q. Li, J.O. Jensen. Lowering the platinum loading of high temperature polymer electrolyte membrane fuel cells with acid doped polybenzimidazole membranes, *Journal of Power Sources* 293, 51–56, 2015. DOI:10.1016/j.jpowsour.2015.05.031.

[27] R. Kerr, H.R. García, M. Rastedt, P. Wagner, S.M. Alfaro, M.T. Romero, C. Terkelsen, T. Steenberg, H.A. Hjuler. Lifetime and degradation of high temperature PEM membrane electrode assemblies, in: Int. J. Hydrogen Energy, Elsevier Ltd, 2015, pp. 16860–16866. DOI:10.1016/j.ijhydene.2015.07.152.

[28] U. Reimer, B. Schumacher, W. Lehnert. Accelerated Degradation of High-Temperature Polymer Electrolyte Fuel Cells: Discussion and Empirical Modeling, *Journal of The Electrochemical Society* 162, F153–F164, 2015. DOI:10.1149/2.0961501jes.

[29] J. Zhao, X. Li. A review of polymer electrolyte membrane fuel cell durability for vehicular applications: Degradation modes and experimental techniques, *Energy Conversion and Management* 199, 2019. DOI:10.1016/j.enconman.2019.112022.

[30] M. Tonny, D. Jakobsen, J.O. Jensen, L.N. Cleemann, Q. Li. Durability Issues and Status of PBI-Based Fuel Cells 22, n.d. DOI:10.1007/978-3-319-17082-4_22.

[31] J.P. Melchior, K.D. Kreuer, J. Maier. Proton conduction mechanisms in the phosphoric acid-water system (H4P2O7-H3PO4·2H2O): A 1H, 31P and 17O PFG-NMR and conductivity study, *Physical Chemistry Chemical Physics* 19, 587–600, 2017. DOI:10.1039/c6cp04855b.

[32] S. Yu, L. Xiao, B.C. Benicewicz. Durability studies of PBI-based high temperature PEMFCs, in: Fuel Cells, 2008, pp. 165–174. DOI:10.1002/fuce.200800024.

[33] Y. Oono, T. Fukuda, A. Sounai, M. Hori. Influence of operating temperature on cell performance and endurance of high temperature proton exchange membrane fuel cells, *Journal of Power Sources* 195, 1007–1014, 2010. DOI:10.1016/J.JPOWSOUR.2009.08.097.

[34] T. Søndergaard, L.N. Cleemann, H. Becker, T. Steenberg, H.A. Hjuler, L. Seerup, Q. Li, J.O. Jensen. Long-Term Durability of PBI-Based HT-PEM Fuel Cells: Effect of Operating Parameters, *Journal of The Electrochemical Society* 165, F3053–F3062, 2018. DOI:10.1149/2.0081806jes.

[35] C. Wannek, I. Konradi, J. Mergel, W. Lehnert. Redistribution of phosphoric acid in membrane electrode assemblies for high-temperature polymer electrolyte fuel cells, *International Journal of Hydrogen Energy* 34, 9479–9485, 2009. DOI:10.1016/J.IJHYDENE.2009.09.076.

[36] S. Chevalier, M. Fazeli, F. Mack, S. Galbiati, I. Manke, A. Bazylak, R. Zeis. Role of the microporous layer in the redistribution of phosphoric acid in high temperature PEM fuel cell gas diffusion electrodes, *Electrochimica Acta* 212, 187–194, 2016. DOI:10.1016/J.ELECTACTA.2016.06.121.

[37] T. Tingelöf, J.K. Ihonen. A rapid break-in procedure for PBI fuel cells, *International Journal of Hydrogen Energy* 34, 6452–6456, 2009. DOI:10.1016/j.ijhydene.2009.05.003.

[38] K. Kwon, T.Y. Kim, D.Y. Yoo, S.G. Hong, J.O. Park. Maximization of high-temperature proton exchange membrane fuel cell performance with the optimum distribution of phosphoric acid, *Journal of Power Sources* 188, 463–467, 2009. DOI:10.1016/j.jpowsour.2008.11.104.

[39] S.H. Eberhardt, M. Toulec, F. Marone, M. Stampanoni, F.N. Büchi, T.J. Schmidt. Dynamic Operation of HT-PEFC: In-Operando Imaging of Phosphoric Acid Profiles and (Re)distribution, *Journal of The Electrochemical Society* 162, F310–

F316, 2015. DOI:10.1149/2.0751503jes.

[40] H. Becker, L.N. Cleemann, D. Aili, J.O. Jensen, Q. Li. Probing phosphoric acid redistribution and anion migration in polybenzimidazole membranes, *Electrochemistry Communications* 82, 21–24, 2017. DOI:10.1016/j.elecom.2017.07.005.

[41] H. Becker, U. Reimer, D. Aili, L.N. Cleemann, J.O. Jensen, W. Lehnert, Q. Li. Determination of Anion Transference Number and Phosphoric Acid Diffusion Coefficient in High Temperature Polymer Electrolyte Membranes, *Journal of The Electrochemical Society* 165, F863–F869, 2018. DOI:10.1149/2.1201810jes.

[42] A. Tobias, M. Wiebke, C. Tötzke, C. Wannek, H. Markötter, F. Wieder, J. Banhart, W. Lehnert, I. Manke. Synchrotron X-ray radioscopic in situ study of high-temperature polymer electrolyte fuel cells - Effect of operation conditions on structure of membrane, *Journal of Power Sources* 246, 290–298, 2014. DOI:10.1016/j.jpowsour.2013.07.094.

[43] J. Yang, Q. Li, L.N. Cleemann, J.O. Jensen, C. Pan, N.J. Bjerrum, R. He. Crosslinked hexafluoropropylidene polybenzimidazole membranes with chloromethyl polysulfone for fuel cell applications, *Advanced Energy Materials* 3, 622–630, 2013. DOI:10.1002/aenm.201200710.

[44] W. Maier, T. Arlt, C. Wannek, I. Manke, H. Riesemeier, P. Krüger, J. Scholta, W. Lehnert, J. Banhart, D. Stolten. In-situ synchrotron X-ray radiography on high temperature polymer electrolyte fuel cells, *Electrochemistry Communications* 12, 1436–1438, 2010. DOI:10.1016/j.elecom.2010.08.002.

[45] Y. Oono, A. Sounai, M. Hori. Long-term cell degradation mechanism in high-temperature proton exchange membrane fuel cells, *Journal of Power Sources* 210, 366–373, 2012. DOI:10.1016/J.JPOWSOUR.2012.02.098.

[46] Y. Oono, A. Sounai, M. Hori. Prolongation of lifetime of high temperature proton exchange membrane fuel cells, *Journal of Power Sources* 241, 87–93, 2013. DOI:10.1016/J.JPOWSOUR.2013.03.122.

[47] F. Ruiz-Zepeda, M. Gatalo, A. Pavlišič, G. Dražić, P. Jovanovič, M. Bele, M. Gaberšček, N. Hodnik. Atomically Resolved Anisotropic Electrochemical Shaping of Nano-electrocatalyst, *Nano Letters* 19, 4919–4927, 2019. DOI:10.1021/acs.nanolett.9b00918.

[48] T. Søndergaard, L.N. Cleemann, L. Zhong, H. Becker, T. Steenberg, H.A. Hjuler, L. Seerup, Q. Li, J.O. Jensen. Catalyst Degradation Under Potential Cycling as an Accelerated Stress Test for PBI-Based High-Temperature PEM Fuel Cells—Effect of Humidification, *Electrocatalysis* 9, 302–313, 2018. DOI:10.1007/s12678-017-0427-1.

[49] A. Honji, T. Mori, K. Tamura, Y. Hishinuma. Agglomeration of Platinum Particles Supported on Carbon in Phosphoric Acid, *Journal of The Electrochemical Society* 135, 355–359, 1988. DOI:10.1149/1.2095614.

[50] M. Prokop, T. Bystron, P. Belsky, O. Tucek, R. Kodym, M. Paidar, K. Bouzek. Degradation kinetics of Pt during high-temperature PEM fuel cell operation Part III: Voltage-dependent Pt degradation rate in single-cell experiments, *Electrochimica Acta* 363, 2020. DOI:10.1016/j.electacta.2020.137165.

[51] P. Bindra, S.J. Clouser, E. Yeager. Platinum Dissolution in Concentrated Phosphoric Acid, *Journal of The Electrochemical Society* 126, 1631–1632, 1979. DOI:10.1149/1.2129345.

[52] C.A. Reiser, L. Bregoli, T.W. Patterson, J.S. Yi, J.D. Yang, M.L. Perry, T.D. Jarvi. A Reverse-Current Decay Mechanism for Fuel Cells, *Electrochemical and Solid-State Letters* 8, A273, 2005. DOI:10.1149/1.1896466.

[53] W. Gu, R.N. Carter, P.T. Yu, H.A. Gasteiger. Start/Stop and Local H2 Starvation Mechanisms of Carbon Corrosion: Model vs. Experiment, *ECS Transactions* 11, 963–973, 2007. DOI:10.1149/1.2781008.

[54] L.N. Cleemann, F. Buazar, Q. Li, J.O. Jensen, C. Pan, T. Steenberg, S. Dai, N.J. Bjerrum. Catalyst degradation in high temperature proton exchange membrane fuel cells based on acid doped polybenzimidazole membranes, *Fuel Cells* 13, 822–831, 2013. DOI:10.1002/fuce.201200186.

[55] M. Okamoto, T. Fujigaya, N. Nakashima. Design of an assembly of poly(benzimidazole), carbon nanotubes, and Pt nanoparticles for a fuel-cell electrocatalyst with an ideal interfacial nanostructure, *Small* 5, 735–740, 2009. DOI:10.1002/smll.200801742.

[56] M. Perchthaler, T. Ossiander, V. Juhart, J. Mitzel, C. Heinzl, C. Scheu, V. Hacker. Tungsten materials as durable catalyst supports for fuel cell electrodes, *Journal of Power Sources* 243, 472–480, 2013. DOI:10.1016/j.jpowsour.2013.06.022.

[57] J. Lobato, H. Zamora, J. Plaza, P. Cañizares, M.A. Rodrigo. Enhancement of high temperature PEMFC stability using catalysts based on Pt supported on SiC based materials, *Applied Catalysis B: Environmental* 198, 516–524, 2016. DOI:10.1016/j.apcatb.2016.06.011.

[58] M. Millán, H. Zamora, M.A. Rodrigo, J. Lobato. Enhancement of Electrode Stability Using Platinum-Cobalt Nanocrystals on a Novel Composite SiCTiC Support, *ACS Applied Materials and Interfaces* 9, 5927–5936, 2017. DOI:10.1021/acsami.6b13071.

[59] T.J. Schmidt, J. Baurmeister. Properties of high-temperature PEFC Celtec®-P 1000 MEAs in start/stop operation mode, *Journal of Power Sources* 176, 428–434, 2008. DOI:10.1016/j.jpowsour.2007.08.055.

[60] T. Søndergaard, L.N. Cleemann, H. Becker, D. Aili, T. Steenberg, H.A. Hjuler, L. Seerup, Q. Li, J.O. Jensen. Long-term durability of HT-PEM fuel cells based on thermally cross-linked polybenzimidazole, *Journal of Power Sources* 342, 570–578, 2017. DOI:10.1016/j.jpowsour.2016.12.075.

[61] A.T. Pingitore, F. Huang, G. Qian, B.C. Benicewicz. Durable High Polymer Content m/ p-Polybenzimidazole Membranes for Extended Lifetime Electrochemical Devices, *ACS Applied Energy Materials* 2, 1720–1726, 2019. DOI:10.1021/acsaem.8b01820.

[62] M. Rastedt, F.J. Pinar, N. Pilinski, A. Dyck, P. Wagner. Effect of Operation Strategies on Phosphoric Acid Loss in HT-PEM Fuel Cells, *ECS Transactions*

75, 455–469, 2016. DOI:10.1149/07514.0455ecst.

[63] S. Galbiati, A. Baricci, A. Casalegno, R. Marchesi. Degradation in phosphoric acid doped polymer fuel cells: A 6000 h parametric investigation, *International Journal of Hydrogen Energy* 38, 6469–6480, 2013. DOI:10.1016/J.IJHYDENE.2013.03.012.

[64] J.O. Leader, Y. Yue, M.R. Walluk, T.A. Trabold. Voltage degradation of high-temperature PEM fuel cells operating at 200 °C under constant load and start-stop conditions, *International Journal of Hydrogen Energy* 47, 18820–18830, 2022. DOI:10.1016/J.IJHYDENE.2022.04.067.

[65] D. Aili, J. Zhang, M.T. Dalsgaard Jakobsen, H. Zhu, T. Yang, J. Liu, M. Forsyth, C. Pan, J.O. Jensen, L.N. Cleemann, S.P. Jiang, Q. Li. Exceptional durability enhancement of PA/PBI based polymer electrolyte membrane fuel cells for high temperature operation at 200°C, *Journal of Materials Chemistry A* 4, 4019–4024, 2016. DOI:10.1039/c6ta01562j.

[66] J. Zhang, D. Aili, J. Bradley, H. Kuang, C. Pan, R. De Marco, Q. Li, S.P. Jiang. In Situ Formed Phosphoric Acid/Phosphosilicate Nanoclusters in the Exceptional Enhancement of Durability of Polybenzimidazole Membrane Fuel Cells at Elevated High Temperatures, *Journal of The Electrochemical Society* 164, F1615–F1625, 2017. DOI:10.1149/2.1051714jes.

[67] D. Aili, L.N. Cleemann, Q. Li, J.O. Jensen, E. Christensen, N.J. Bjerrum. Thermal curing of PBI membranes for high temperature PEM fuel cells, *Journal of Materials Chemistry* 22, 5444–5453, 2012. DOI:10.1039/c2jm14774b.

[68] F.J. Pinar, N. Pilinski, P. Wagner, W.O. Library. Long-Term Testing of a High Temperature Polymer Electrolyte Membrane Fuel Cell: The Effect of Reactant Gases, *American Institute of Chemical Engineers AIChE J* 62, 217–227, 2015. DOI:10.1002/aic.15044.

[69] F.J. Pinar, M. Rastedt, N. Pilinski, P. Wagner, A. Dyck. Demonstrating feasibility of a high temperature polymer electrolyte membrane fuel cell operation with natural gas reformate composition, *International Journal of Hydrogen Energy* 42,

13860–13875, 2017. DOI:10.1016/J.IJHYDENE.2017.03.161.

[70] F. Zhou, S.J. Andreasen, S.K. Kær, J.O. Park. Experimental investigation of carbon monoxide poisoning effect on a PBI/H3PO4 high temperature polymer electrolyte membrane fuel cell: Influence of anode humidification and carbon dioxide, *International Journal of Hydrogen Energy* 40, 14932–14941, 2015. DOI:10.1016/J.IJHYDENE.2015.09.056.

[71] T.J. Schmidt, J. Baurmeister. Durability and Reliability in High-Temperature Reformed Hydrogen PEFCs, *ECS Transactions* 3, 861–869, 2006. DOI:10.1149/1.2356204.

[72] H.A. Hjuler, K. Azizi, N. Seselj, S. Martinez Alfaro, H.R. Garcia, D. Gromadskyi, L. Hromadska, S. Primdahl, J.O. Jensen, Q. Li, S. Celenk, L. Cleemann. Durability Studies on PBI Based High Temperature PEMFC, *ECS Transactions* 104, 403–413, 2021. DOI:10.1149/10408.0403ecst.

[73] F. Javier Pinar, M. Rastedt, N. Pilinski, P. Wagner. Effect of idling temperature on high temperature polymer electrolyte membrane fuel cell degradation under simulated start/stop cycling conditions, *International Journal of Hydrogen Energy* 41, 19463–19474, 2016. DOI:10.1016/J.IJHYDENE.2016.05.091.

[74] A. Oyarce, E. Zakrisson, M. Ivity, C. Lagergren, A.B. Ofstad, A. Bodén, G. Lindbergh. Comparing shut-down strategies for proton exchange membrane fuel cells, *Journal of Power Sources* 254, 232–240, 2014. DOI:10.1016/J.JPOWSOUR.2013.12.058.

[75] Z. Qi, S. Buelte. Effect of open circuit voltage on performance and degradation of high temperature PBI-H3PO4 fuel cells, *Journal of Power Sources* 161, 1126–1132, 2006. DOI:10.1016/J.JPOWSOUR.2006.06.020.

[76] S. Liu, M. Rasinski, Y. Rahim, S. Zhang, K. Wippermann, U. Reimer, W. Lehnert. Influence of operating conditions on the degradation mechanism in high-temperature polymer electrolyte fuel cells, *Journal of Power Sources* 439, 2019. DOI:10.1016/j.jpowsour.2019.227090.

[77] D. Schonvogel, M. Rastedt, P. Wagner, M. Wark, A. Dyck. Impact of Accelerated Stress Tests on High Temperature PEMFC Degradation, *Fuel Cells* 16, 480–489, 2016. DOI:10.1002/fuce.201500160.

[78] J. Büsselmann, M. Rastedt, V. Tullius, K. Yezerska, A. Dyck, P. Wagner. Evaluation of HT-PEM MEAs: Load cycling versus start/stop cycling, *International Journal of Hydrogen Energy* 19384–19394, 2019. DOI:10.1016/j.ijhydene.2018.07.181.

[79] R. Taccani, T. Chinese, M. Boaro. Effect of accelerated ageing tests on PBI HTPEM fuel cells performance degradation, *International Journal of Hydrogen Energy* 42, 1875–1883, 2017. DOI:10.1016/J.IJHYDENE.2016.09.164.

[80] F. Valle, N. Zuliani, B. Marmiroli, H. Amenitsch, R. Taccani. SAXS analysis of catalyst degradation in high temperature PEM fuel cells subjected to accelerated ageing tests, *Fuel Cells* 14, 938–944, 2014. DOI:10.1002/fuce.201300221.

[81] K.H. Lim, A.S. Lee, V. Atanasov, J. Kerres, E.J. Park, S. Adhikari, S. Maurya, L.D. Manriquez, J. Jung, C. Fujimoto, I. Matanovic, J. Jankovic, Z. Hu, H. Jia, Y.S. Kim. Protonated phosphonic acid electrodes for high power heavy-duty vehicle fuel cells, *Nature Energy* 7, 248–259, 2022. DOI:10.1038/s41560-021-00971-x.

[82] J. Park, L. Wang, S.G. Advani, A.K. Prasad. Mechanical stability of H3PO4-Doped PBI/Hydrophilic-Pretreated PTFE membranes for high temperature PEMFCs, *Electrochimica Acta* 120, 30–38, 2014. DOI:10.1016/j.electacta.2013.12.030.

[83] T.E. Springer, T. Rockward, T.A. Zawodzinski, S. Gottesfeld. Model for Polymer Electrolyte Fuel Cell Operation on Reformate Feed: Effects of CO, H[sub 2] Dilution, and High Fuel Utilization, *Journal of The Electrochemical Society* 148, A11, 2001. DOI:10.1149/1.1344516.

[84] S. Jiménez, J. Soler, R.X. Valenzuela, L. Daza. Assessment of the performance of a PEMFC in the presence of CO, in: J. Power Sources, Elsevier, 2005, pp. 69–73. DOI:10.1016/j.jpowsour.2005.02.049.

[85] Q. Li, R. He, J.-A. Gao, J.O. Jensen, N.J. Bjerrum. The CO Poisoning Effect in PEMFCs Operational at Temperatures up to 200°C, *Journal of The Electrochemical Society* 150, A1599, 2003. DOI:10.1149/1.1619984.

[86] J. Zhang, Z. Xie, J. Zhang, Y. Tang, C. Song, T. Navessin, Z. Shi, D. Song, H. Wang, D.P. Wilkinson, Z.S. Liu, S. Holdcroft. High temperature PEM fuel cells, *Journal of Power Sources* 160, 872–891, 2006. DOI:10.1016/j.jpowsour.2006.05.034.

[87] Q. Li, R. He, J.O. Jensen, N.J. Bjerrum. PBI-Based Polymer Membranes for High Temperature Fuel Cells ± Preparation, Characterization and Fuel Cell Demonstration, n.d. DOI:10.1002/fuce.200400020.

[88] S.K. Das, A. Reis, K.J. Berry. Experimental evaluation of CO poisoning on the performance of a high temperature proton exchange membrane fuel cell, *Journal of Power Sources* 193, 691–698, 2009. DOI:10.1016/J.JPOWSOUR.2009.04.021.

[89] P. Krishnan, J.S. Park, C.S. Kim. Performance of a poly(2,5-benzimidazole) membrane based high temperature PEM fuel cell in the presence of carbon monoxide, *Journal of Power Sources* 159, 817–823, 2006. DOI:10.1016/j.jpowsour.2005.11.071.

[90] H. Liang, H. Su, B.G. Pollet, V. Linkov, S. Pasupathi. Membrane electrode assembly with enhanced platinum utilization for high temperature proton exchange membrane fuel cell prepared by catalyst coating membrane method, *Journal of Power Sources* 266, 107–113, 2014. DOI:10.1016/J.JPOWSOUR.2014.05.014.

[91] F. Liu, S. Mohajeri, Y. Di, K. Wippermann, W. Lehnert. Influence of the Interaction between Phosphoric Acid and Catalyst Layers on the Properties of HT-PEFCs, in: Fuel Cells, 2014, pp. 750–757. DOI:10.1002/fuce.201300272.

[92] D. Yao, W. Zhang, Q. Ma, Q. Xu, S. Pasupathi, H. Su. Achieving high Pt utilization and superior performance of high temperature polymer electrolyte membrane fuel cell by employing low-Pt-content catalyst and microporous layer

free electrode design, *Journal of Power Sources* 426, 124–133, 2019. DOI:10.1016/J.JPOWSOUR.2019.04.045.

[93] S. Martin, J.O. Jensen, Q. Li, P.L. Garcia-Ybarra, J.L. Castillo. Feasibility of ultra-low Pt loading electrodes for high temperature proton exchange membrane fuel cells based in phosphoric acid-doped membrane, *International Journal of Hydrogen Energy* 44, 28273–28282, 2019. DOI:10.1016/J.IJHYDENE.2019.09.073.

[94] S. Martin, P.L. Garcia-Ybarra, J.L. Castillo. Ten-fold reduction from the state-of-the-art platinum loading of electrodes prepared by electrospraying for high temperature proton exchange membrane fuel cells, *Electrochemistry Communications* 93, 57–61, 2018. DOI:10.1016/J.ELECOM.2018.06.007.

[95] D. Úbeda, P. Cañizares, P. Ferreira-Aparicio, A.M. Chaparro, J. Lobato, M.A. Rodrigo. Life test of a high temperature PEM fuel cell prepared by electrospray, *International Journal of Hydrogen Energy* 41, 20294–20304, 2016. DOI:10.1016/J.IJHYDENE.2016.09.109.

[96] H. Liang, H. Su, B.G. Pollet, S. Pasupathi. Development of membrane electrode assembly for high temperature proton exchange membrane fuel cell by catalyst coating membrane method, *Journal of Power Sources* 288, 121–127, 2015. DOI:10.1016/J.JPOWSOUR.2015.04.123.

[97] K. Kwon, D.Y. Yoo, J.O. Park. Experimental factors that influence carbon monoxide tolerance of high-temperature proton-exchange membrane fuel cells, *Journal of Power Sources* 185, 202–206, 2008. DOI:10.1016/J.JPOWSOUR.2008.06.053.

[98] A. Bergmann, D. Gerteisen, T. Kurz. Modelling of CO poisoning and its dynamics in HTPEM fuel cells, in: Fuel Cells, 2010, pp. 278–287. DOI:10.1002/fuce.200900128.

[99] J.J. Linares, C. Sanches, V.A. Paganin, E.R. Gonzalez. Performance of a poly(2,5-benzimidazole)-based polymer electrolyte membrane fuel cell, *International Journal of Hydrogen Energy* 37, 7212–7220, 2012.

DOI:10.1016/J.IJHYDENE.2011.12.030.

[100] A.D. Modestov, M.R. Tarasevich, V.Y. Filimonov, E.S. Davydova. CO tolerance and CO oxidation at Pt and Pt-Ru anode catalysts in fuel cell with polybenzimidazole-H3PO4 membrane, *Electrochimica Acta* 55, 6073–6080, 2010. DOI:10.1016/J.ELECTACTA.2010.05.068.

[101] S. Ahmed, M. Krumpelt. Hydrogen from hydrocarbon fuels for fuel cells, *International Journal of Hydrogen Energy* 26, 291–301, 2001. DOI:10.1016/S0360-3199(00)00097-5.

[102] Q. Ming, T. Healey, L. Allen, P. Irving. Steam reforming of hydrocarbon fuels, in: Catal. Today, 2002, pp. 51–64. DOI:10.1016/S0920-5861(02)00232-8.

[103] T.A. Semelsberger, R.L. Borup. Fuel effects on start-up energy and efficiency for automotive PEM fuel cell systems, *International Journal of Hydrogen Energy* 30, 425–435, 2005. DOI:10.1016/j.ijhydene.2004.11.007.

[104] K.M. Caldwell, S. Kaserer, C. Roth, D.E. Ramaker. Following Adsorbate Coverage on Anodes of High-Temperature Polymer ElectrolyteMembrane Fuel Cells in the Presence of CO and H 2 Ob yu sing In Operando X-ray Absorption Spectroscopy, n.d. DOI:10.1002/celc.201500228.

[105] H. Igarashi, T. Fujino, M. Watanabe. Hydrogen electro-oxidation on platinum catalysts in the presence of trace carbon monoxide, *Journal of Electroanalytical Chemistry* 391, 119–123, 1995. DOI:10.1016/0022-0728(95)03914-3.

[106] W. Vogel, L. Lundquist, P. Ross, P. Stonehart. Reaction pathways and poisons-II. The rate controlling step for electrochemical oxidation of hydrogen on Pt in acid and poisoning of the reaction by CO, *Electrochimica Acta* 20, 79–93, 1975. DOI:10.1016/0013-4686(75)85048-1.

[107] J. Durst, A. Siebel, C. Simon, F. Hasché, J. Herranz, H.A. Gasteiger. New insights into the electrochemical hydrogen oxidation and evolution reaction mechanism, *Energy and Environmental Science* 7, 2255–2260, 2014. DOI:10.1039/c4ee00440j.

[108] H.A. Gasteiger, J.E. Panels, S.G. Yan. Dependence of PEM fuel cell performance on catalyst loading, *Journal of Power Sources* 127, 162–171, 2004. DOI:10.1016/J.JPOWSOUR.2003.09.013.

[109] J.O. Bockris, J. McBreen, L. Nanis. The Hydrogen Evolution Kinetics and Hydrogen Entry into a-Iron, *Journal of The Electrochemical Society* 112, 1025, 1965. DOI:10.1149/1.2423335.

[110] J.O. Bockris, E.C. Potter. The Mechanism of Hydrogen Evolution at Nickel Cathodes in Aqueous Solutions, *The Journal of Chemical Physics* 20, 614–628, 2004. DOI:10.1063/1.1700503.

[111] B.E. Conway, J.O. Bockris. Electrolytic Hydrogen Evolution Kinetics and Its Relation to the Electronic and Adsorptive Properties of the Metal, *The Journal of Chemical Physics* 26, 532–541, 2004. DOI:10.1063/1.1743339.

[112] W. Sheng, Z. Zhuang, M. Gao, J. Zheng, J.G. Chen, Y. Yan. Correlating hydrogen oxidation and evolution activity on platinum at different pH with measured hydrogen binding energy, *Nature Communications* 6, 2015. DOI:10.1038/ncomms6848.

[113] J. Durst, C. Simon, F. Hasché, H.A. Gasteiger. Hydrogen Oxidation and Evolution Reaction Kinetics on Carbon Supported Pt, Ir, Rh, and Pd Electrocatalysts in Acidic Media, *Journal of The Electrochemical Society* 162, F190–F203, 2015. DOI:10.1149/2.0981501jes.

[114] W. Sheng, H.A. Gasteiger, Y. Shao-Horn. Hydrogen Oxidation and Evolution Reaction Kinetics on Platinum: Acid vs Alkaline Electrolytes, *Journal of The Electrochemical Society* 157, B1529, 2010. DOI:10.1149/1.3483106.

[115] K.C. Neyerlin, W. Gu, J. Jorne, H.A. Gasteiger. Study of the Exchange Current Density for the Hydrogen Oxidation and Evolution Reactions, *Journal of The Electrochemical Society* 154, B631, 2007. DOI:10.1149/1.2733987.

[116] C. Song, Y. Tang, J.L. Zhang, J. Zhang, H. Wang, J. Shen, S. McDermid, J. Li, P. Kozak. PEM fuel cell reaction kinetics in the temperature range of 23-120 °C,

Electrochimica Acta 52, 2552–2561, 2007. DOI:10.1016/J.ELECTACTA.2006.09.008.

[117] B.M. Stühmeier, M.R. Pietsch, J.N. Schwämmlein, H.A. Gasteiger. Pressure and Temperature Dependence of the Hydrogen Oxidation and Evolution Reaction Kinetics on Pt Electrocatalysts via PEMFC-based Hydrogen-Pump Measurements, *Journal of The Electrochemical Society* 168, 064516, 2021. DOI:10.1149/1945-7111/ac099c.

[118] P. Schneider, M. Batool, A.O. Godoy, R. Singh, D. Gerteisen, J. Jankovic, N. Zamel. Impact of Platinum Loading and Layer Thickness on Cathode Catalyst Degradation in PEM Fuel Cells, *Journal of The Electrochemical Society* 170, 024506, 2023. DOI:10.1149/1945-7111/acb8df.

[119] M. Rau, A. Niedergesäß, C. Cremers, S. Alfaro, T. Steenberg, H.A. Hjuler. Characterization of Membrane Electrode Assemblies for High-Temperature PEM Fuel Cells, *Fuel Cells* 16, 577–583, 2016. DOI:10.1002/fuce.201500105.

[120] J. Aragane, H. Urushibata, T. Murahashi. Effect of operational potential on performance decay rate in a phosphoric acid fuel cell, *Journal of Applied Electrochemistry* 26, 147–152, 1996. DOI:10.1007/BF00364064.

[121] J. Büsselmann, M. Rastedt, V. Tullius, K. Yezerska, A. Dyck, P. Wagner. Evaluation of HT-PEM MEAs: Load cycling versus start/stop cycling, *International Journal of Hydrogen Energy* 19384–19394, 2019. DOI:10.1016/J.IJHYDENE.2018.07.181.

[122] J. Li, L. Yang, Z. Wang, H. Sun, G. Sun. Degradation study of high temperature proton exchange membrane fuel cell under start/stop and load cycling conditions, *International Journal of Hydrogen Energy* 46, 24353–24365, 2021. DOI:10.1016/j.ijhydene.2021.05.010.

[123] S. Liu, M. Rasinski, Y. Rahim, S. Zhang, K. Wippermann, U. Reimer, W. Lehnert. Influence of operating conditions on the degradation mechanism in high-temperature polymer electrolyte fuel cells, *Journal of Power Sources* 439, 227090, 2019. DOI:10.1016/j.jpowsour.2019.227090.

[124] K. Kinoshita, J.A.S. Bett. Determination of carbon surface oxides on platinum-catalyzed carbon, *Carbon* 12, 525–533, 1974. DOI:10.1016/0008-6223(74)90054-2.

[125] H.S. Oh, J.H. Lee, H. Kim. Electrochemical carbon corrosion in high temperature proton exchange membrane fuel cells, *International Journal of Hydrogen Energy* 37, 10844–10849, 2012. DOI:10.1016/J.IJHYDENE.2012.04.095.

6. APPENDED MANUSCRIPT

MANUSCRIPT 1

CO Poisoning in High Temperature Polymer Electrolyte Membrane Fuel Cells Operating with Diluted Hydrogen and Low Pt Loadings

Sanser Celenk, Santiago Martin, Lars N. Cleemann, Qingfeng Li and Jens Oluf Jensen

Received 00th January 20xx,
Accepted 00th January 20xx

DOI: 10.1039/x0xx00000x

CO Poisoning in High Temperature Polymer Electrolyte Membrane Fuel Cells Operating with Diluted Hydrogen and Low Pt Loading

Sanser Celenk,[1] Santiago Martin,[1,2] Lars N. Cleemann,[3] Qingfeng Li[1] and Jens Oluf Jensen*,[1]

Abstract

The CO poisoning of platinum based catalsysts at temperatures below 100°C has long been recognized an issue while the signifciant tolerance by high temperature polymer electrolyte polymer fuel cells has been well demonstarted. The subject is now revisited by focusing on the combinated effects of the hydrogen dilution and low Pt load anode. Under a constant H_2 stoichiometry the fuel cell performance degradation caused by the CO poisoning is found to be notably increased by using diluted hydrogen with inert components. A major contribution to the anode performance loss is found to be from the H_2 dilution but not the CO poisoning. Both the hydrogen diluting and CO poisoning effects are significantly intensified for electrodes of low Pt loadings, which limit the overall available active sites of the catalysts and hence the sensitivity towards the strong CO adsorption.

Keywords: CO poisoning, polybenzimidazole (PBI), high temperature polymer fuel cell, fuel dilution.

1. Introduction

Low temperature polymer electrolyte membrane fuel cells (PEMFCs) has been recognized as one of the most promising type of fuel cells for a future clean power generation. Among its more prominent features are the high power density, high energy efficiency and fast response to the load transition as well as startup, making the technology practical for automobiles as well as portable applications.[1] The most widely used membrane electrolyte is the perfluorosulfonic acid (PFSA). The membrane material has high conductivity, excellent chemical stability, mechanical strength and flexibility as well as well demonstrated long-term durability. However, it functions only in a highly hydrated state. As a result, the technology is limited to operation at temperatures up to around 80 °C under ambient pressure in order to maintain a high-water content in the membrane. The technology is based on platinum catalysts for both cathode and anode and the high cost and resource limitation constitutes a barriers against the large scale commercialization of the technology.[2]

Another critical issue is the establishment of an infrastructure for production and supply of hydrogen as fuel, The need for the high purity hydrogen is associated with the noble metal catalysts, which are highly sensitive towards the poison of fuel impurities, in particular carbon monoxide. At typical operating temperatures around 80 °C, the Pt-based anode can tolerate a CO content in the range of only 10-20 ppm [3,4]. Pure H_2 can be obtained from water electrolysis via renewable energy but the infrastructure for H_2 distribution and storage is still lacking. Hydrogen can be on board produced from other carriers such as hydrocarbons and alcohols by means of fuel reforming. The reformate gas, although rich in H_2, always contains CO and other components. The CO removal down to the 10 ppm level increases the complexity of the subsequent purification of the reformate gas i.e., preferential oxidation, membrane separation or methanation, which negatively affects to the cost and the overall efficiency of the fuel processing.

The CO poisoning is via the competitive adsorption on Pt surface and hence reduces the active surface site numbers available for the hydrogen oxidation, because the anodic oxidation of hydrogen is essentially determined by the rate of hydrogen dissociative chemisorption. Electrochemically, the adsorbed CO can also be oxidized, however at the electrode potential where the oxygen-containing species are formed at the platinum surface, *i.e.*, corresponding to an anode potential around 0.5 V *vs.* the reversible hydrogen electrode (RHE). Under working conditions for fuel cells, the anode

1. *Department of Energy Storage and Conversion, Technical University of Denmark, Fysikvej B310, 2800 Lyngby, Denmark.*
2. *Blue World Technologies, Egeskovvej 6C, 3490 Kvistgård, Denmark.*

* *Correspondance: kaz@blue.world; qfli@dtu.dk*

operates in a potential region between 0 and 0.1 V *vs.* RHE. In this potential range, CO is hence an inert adsorbate on the platinum catalyst surface. Thermodynamically the adsorption of CO on Pt presents a highly negative value of the standard free Gibbs energy and hence the greater the temperature the lower the CO adsorption.[5] Therefore, operating a fuel cell at high temperatures is crucial to alleviate the CO poisoning allowing a simplified and less costly fuel processing.

High temperature PEMFCs based in H_3PO_4-doped polybenzimidazole membranes operate at temperatures from 120 to 200 °C and have demonstrated great fuel flexibilities as an alternative technology for use with CO-containing fuels [6,7]. Li et al.[8] reported a tolerance of 3 vol% CO in H_2 at current densities up to 0.8 A cm^{-2} at 200 °C and a Pt loading of 0.5 $mg_{Pt}cm^{-2}$, with the CO tolerance defined as a voltage loss < 10 mV with respect to the pure H_2 fed. Krishnan et al. [9] observed no voltage decay at 1 vol% CO in H_2 at 210 °C with an anode catalyst loading of 0.5 $mg_{Pt}cm^{-2}$. Das et al.[10] used an anode Pt loading of 0.75 $mg_{Pt}cm^{-2}$ and showed no voltage drop for current densities up to 200 mA cm^{-2} at 180 °C when feeding the anode with 2 and 5 vol% CO in H_2.

These studies have been conducted using high platinum catalyst loadings. Recent efforts are being made to lower the Pt loadings to a level below 0.3 mg_{Pt} cm^{-2} [11-13] or even down to the ultralow level of 0.1 mg_{Pt} cm^{-2} [14-19]. It is expected that the CO poisoning will be strongly dependent on the Pt loading of the electrodes. The poisoning effect has, however, not been investigated for these low and ultralow Pt loading electrodes.

In addition, most of literature studies on the CO poisoning [20-23] have evaluated the CO tolerance in H_2/CO gas mixtures. Other gas components are also present in reformate fuels such as CO_2, N_2 and water vapor, depending on the fuel processing methods.[24] These components are often chemically inert but their diluting effect on the H_2 partial pressure may also influence the CO poisoning as the practical H_2 concentrations in reformate fuels can vary in a wide range from 40 up to 80 vol%.[25,26]

In the present work the effect of the CO poisoning in the presence of diluting gases is studied with electrodes of varied Pt loadings. Thus, volume concentrations of H_2 from 20 up to 80 vol% were investigated with an inert gas e.g., nitrogen or argon as the balancing gas. The studied CO concentrations vary from 0 up to 2.0 vol% while the electrode Pt loadings range from the industrial level of 1.3 down to 0.15 mg_{Pt}/cm^2.

2. Experimental

2.1. Preparation of Electrodes

Catalytic inks with no polymeric binder, as previously described [16,17] were prepared by mixing the catalyst powder (60 wt.% Pt/C, Hispec 9100 from Johnson Matthey) and the solvent (ethanol, 96 vol.%). Dispersions were ultra-sonicated at least 1 hour to achieve good dispersion of the catalyst. After the sonication, the ink was sprayed onto quadratic gas diffusion layers (Freudenberg H2315C2) using an ultrasonic spraying machine (SonoTek ExactaCoat, 120 kHz). A Pt loading of 1.3 mg cm^{-2} was chosen as a reference and used exclusively for both anode and cathode in the first experimental series. For the series with varying catalyst loadings of the anode, individual inks were prepared for anodes 0.15, 0.3, 0.6 and 1.3 mg cm^{-2} keeping the amount of carbon and thus the resulting thickness of the catalyst layer constant, regardless of the Pt loading. The Pt loading of the cathode was kept constant at 1.3 mg cm^{-2} in all experiments.

2.2. Preparation of membrane electrode assemblies

For preparation of membrane electrode assemblies (MEA), commercially available PBI membranes were used (Dapozol® M40, Danish Power Systems, 40 µm). Pieces of PBI membranes were doped in 85 vol.% ortho phosphoric acid aqueous solutions. The membranes were doped for at least 1 week at room temperature resulting in an acid doping level of ca. 10 (mole H_3PO_4 per mole of polymer repeating unit of PBI). For some tests, the membranes were doped for one hour at 40 °C, resulting in a similar acid doping level. MEAs were assembled from two electrodes and a membrane without hot pressing before insertion in the test cell. Kapton sub-gaskets were applied as external membrane enforcement around the electrode edges, which has an active electrode are to 23 cm^2.

2.3. Cell testing

The testing of the MEAs was done in a commercial fuel cell hardware (Baltic Fuel cells qCf FC25/100) connected to an electronic load (Hocher & Hackl ZS506). The test cells were made of machined graphite plates with serpentine flow patterns and gold-plated copper current collectors. The cathode side of the cell was fed with air while the anode feed was changing between pure H_2, H_2+CO and H_2+CO+N_2 depending on the experiment. Gas mixtures for the anode feed were obtained by using pure H_2, pure N_2 and 10% vol. CO in H_2. The three anode gas streams were connected by using a 1/4 ID inch union tee connector. To create a homogeneous gas mixture, approximately 4 meter long 1/16 ID inch steel tube was coiled and connected between the union tee and the main anode flow pipe. Since nearly all of the mass flow controllers were default calibrated for N_2, we further calibrated each mass flow controller with a flow calibration device (Bios Definer 220 from MesaLabs) by using their corresponding gases. Gas flows were controlled by a number of mass flow controllers (Brooks Instrument) each calibrated for the respective gas. All gas control was at ambient pressure and temperature. No external humidification was applied.

2.4. Experimental Procedure

All experiments were conducted at ambient pressure and a fuel cell temperature of 160 °C. Inlet H_2 and air stoichiometry were kept constant (λ_{H2} = 1.5 and λ_{Air} = 2) at current densities greater than or equal to 200 mA cm^{-2}. For cell tests with current loads lower than 200 mA cm^{-2} a constant gas flow rate

was used, corresponding to the above stated stoichiometries at 200 mA cm^{-2}.

Before recording polarization curves, the cells were subjected to 16 hours of break-in at 200 mA cm^{-2} to get stable cell voltage. Polarization curves were then recorded in galvanostatic mode. Data acquisition was started from zero current and continued with stepwise increased current. At each current density step, the value of the cell voltage was captured after 2.5 minutes. After each polarization curve, the cell was returned to the 200 mA cm^{-2} condition to check if the previous cell performance was recovered, after which the fuel mixtures in the anode feed were changed for the next measurements. The CO concentration in the anode feed was changing from 0.25% to 2% while the hydrogen partial pressure was controlled between 20% and 100%.

2.5 Overview of test series

The effect on the CO tolerance was studied in four series. In Series 1, the effect of hydrogen dilution on a cell with a fixed high Pt loading at moderately high CO concentration was measured. The aim was to assess the effect of hydrogen being diluted under typical conditions, though with a somewhat high, yet realistic CO level. Then the study was elaborated to include simultaneous variations of both hydrogen and CO concentrations in Series 2. The effect of the Pt loading on the anode was investigated in Series 3, where the Pt loading and CO concentration were varied, but with no dilution of hydrogen apart from that resulting from the addition of CO. Finally, in Series 4, simultaneous variations of hydrogen and CO concentrations were investigated at a fixed low Pt loading. Table 1 provides an overview of the test series and the values of the three parameters.

Table 1. Overview of the variables in the four experimental series.Overview of the variables in the four experimental series.

	H_2 concentration (%)	CO concentration (%)	Pt loading ($mg_{Pt}cm^{-2}$)	Balancing gas
Series 1	20, 40, 60, 80, 100	1	1.3	N_2
Series 2	20, 40, 60, 80, 100	0, 0.5, 1.0, 1.5, 2.0	1.3	N_2
Series 3	Balance H_2	0.0, 0.25, 0.5, 1.0, 1.5, 2.0	0.15, 0.3, 0.6, 1.3	H_2
Series 4	80, 60, 40	0.0, 0.25, 0.5, 1.0, 1.5, 2.0	0.3	Ar

3. Result and Discussion

3.1 Effect of dilution of hydrogen at 1% CO

A set of polarization curves is displayed in Figure 1. All cells were first calibrated by measuring I-V curves for H_2-Air, which were used as a baseline performance. The typical performance was 0.66 - 0.67 V at a current density of about 200 mA cm^{-2} and a peak power density of 450-500 mW cm^{-2}. It should be noted that the all cells were operated at constant stoichiometry (λ_{H2} = 1.5) i.e., the H_2 flow rate was fixed the same for all the concentrations used (equals to lambda times the stoichiometric H_2 flow rate), which determines the total volume flow rate for each of the concentrations (as the inverse of H_2 volume concentration times H_2 volume flow rate).

When 1% CO was added to pure hydrogen (solid triangle symbols for all four MEAs), a decrease in the cell voltage by 15-17 mV was observed at a current density of 217 $mAcm^{-2}$. A CO concentration of 1.0 % was selected since it represents a reasonable value of the reformate hydrogen after the water gas shift reactor without subsequent extra purification of the gas.[26]

In the following, the hydrogen steam was diluted before introducing CO. The balancing gas. N_2, was a typical inert component in e.g., partial oxidation and used representing the other inert gas components such as CO_2 or methane in case of other types of reformat fuels. The concentration of these inert gases may vary to a great extent in either the inlet or outlet fuel steams. In the present work, a wide range of H_2 dilution (20 – 60 vol%) was studied for considering these possible cases. Every set of measurements was carried out with a new MEA and all the MEAs were prepared in the same way.way.

In Figure 1 the solid squares represent the performance with 1% CO in the H_2-N_2 mixture stream of 20% (Figure 1a), 40% (Figure 1b), 60% (Figure 1c) and 80% (Figure 1d) H_2, in comparison to 100% H_2 (solid triangles). Increased CO poisoning effects are clearly seen from the figure.

The dilution of H_2 is made by addition of N_2. As the N_2 content increases, the partial pressure of hydrogen decreases, which weakens the adsorption of hydrogen on the platinum surface. When 1% CO is added, the effective volume or molar ratio of $[CO]/[H_2]$ is increased and the CO poisoning is therefore enhanced. Thus, compared to the measurement with pure

hydrogen (i.e., 1 vol% CO + 99 vol% H_2) the voltage loss by adding 1% CO to H_2-N_2 mixtures is increased. For example, in Figure 1a for the 20%H_2-80%N_2 mixture fuel, 1 vol% CO corresponds to 4.8 vol% CO in H_2. On the other hand, in addition to the CO poisoning, the dilution of H_2 by N_2 should impart its own negative effect in the polarization curves of Figure 1 due to the decrease in the H_2 partial pressure, an effect overlapped to the CO poisoning.

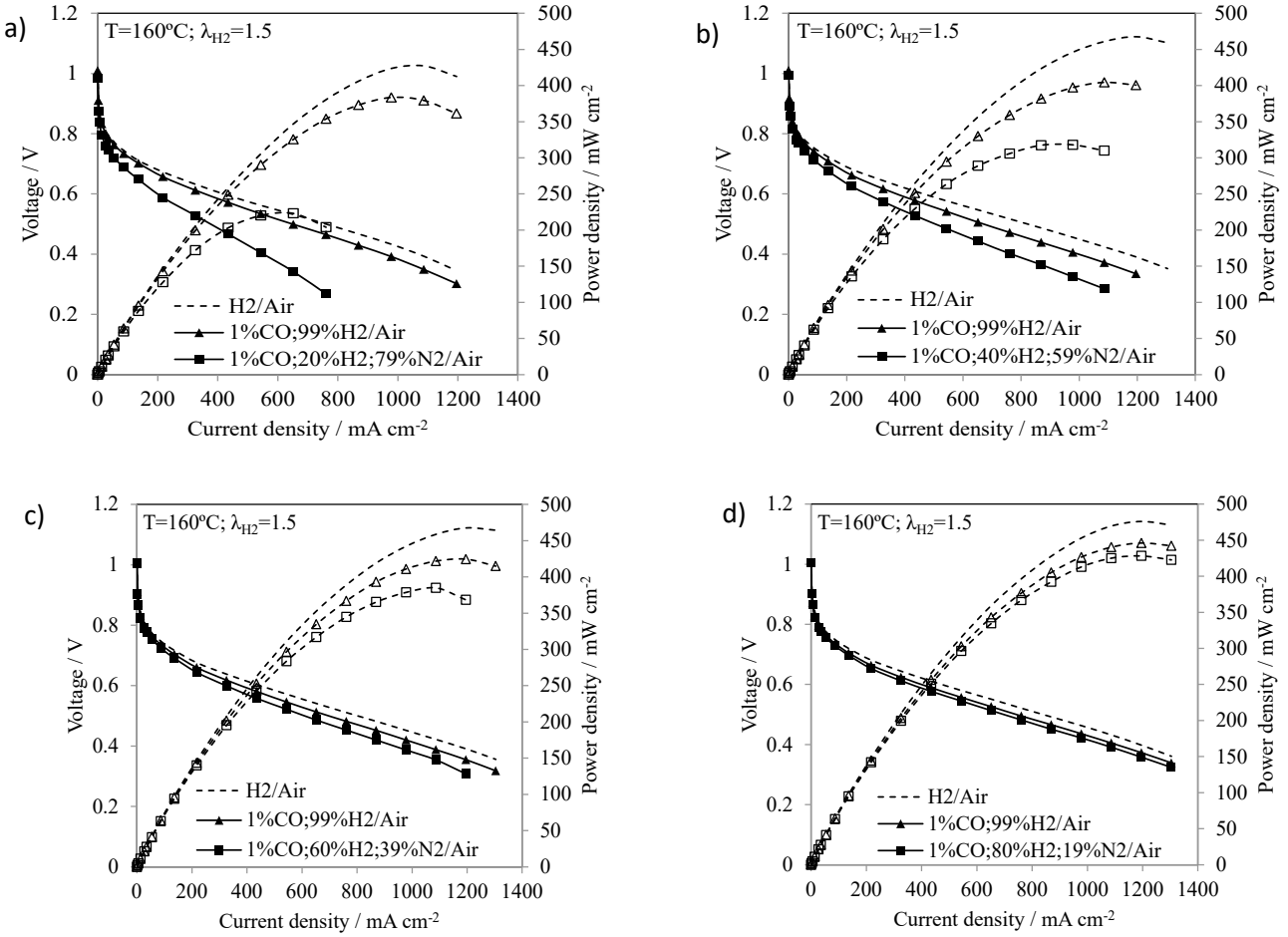

Figure 1. Polarization and power density curves of MEAs when the cathode is supplied with air and the anode is fueled from 1 vol% CO + 99 vol% H_2 and 1 vol% CO + H_2 concentrations of a) 20 vol%; b) 40 vol%; c) 60 vol% and d) 80 vol%, all balanced with N_2. The performance on pure H_2 is included as a base case. All the measurements were performed at 160°C, constant stoichiometries (λ_{H2}=1.5, λ_{O2}=2) and ambient pressure.

In Figure 2 the contribution of two effects, the N_2 dilution and CO poisoning, is evaluated in terms of the cell voltage loss. The voltage profile in the figure starts with a steady state voltage after 24 hours of operation (only 40 minutes are shown) at 200 mA cm^{-2} with pure H_2 and λ_{H2}=1.5, exhibiting a cell voltage of 0.658 V. The fuel is then diluted with N_2 according to the composition of 40 vol% H_2 and 60% N_2 for 120 minutes, where the cell voltage is decreased to 0.638 V, i.e., lowered by 20 mV. During this period the hydrogen stoichiometry (flow rate) was increased from 1.5 to 2.5 and 4.0, which had been shown to have little effect on the cell voltage. After that, the initial condition of pure H_2 was recovered and maintained for another 40 minutes, followed by the CO poisoning at a concentration of 1 % CO in pure (99% CO) for 120 minutes. The feeding of a [CO]/[H_2] = 1/99 mixture fuel led to a small voltage loss of only 6 mV, compared to the performance of pure (100% H_2), that is restored during the period from 320-360 minutes. The next is the CO poisoning in N_2 diluted H_2 in compositions of 1 vol% CO, 40 vol.% H_2 and 59% N_2, showing a total voltage loss of 31 mV with pure (100% H_2) as a reference or only 9 mV in comparison with the 40% H_2 - 60% N_2 mixture without CO addition. Again changes in the hydrogen stoichiometry from 1.5, 2.5 to 4.0 has shown little effect on the measured cell voltage. Finally the cell performance with pure hydrogen was recovered.

The dilution of H_2 by the N_2 addition causes a substantial voltage loss with respect to pure H_2 feeding, despite the same

H_2 volume flow rate was supplied in both cases. The reason behind this behavior is the decrease on the H_2 partial pressure. Kinetically the hydrogen oxidation reaction (HOR) on Pt involves the dissociative adsorption of hydrogen (called the Tafel step):

$$H_2 + 2Pt \rightleftarrows 2Pt\text{-}H_{ads} \quad \text{Tafel step} \quad (1)$$

The adsorption is the slow and rate-determining step, which is followed by the facile electrochemical oxidation of H ad-atoms (the Volmer step):

$$2Pt\text{-}H_{ads} \rightleftarrows 2Pt + 2H^+ + 2e^- \quad \text{Volmer step} \quad (2)$$

The reduced partial pressure of hydrogen hinders the dissociative hydrogen adsorption on platinum and hence the hydrogen oxidation kinetics. The competitive adsorption of CO under the reduced partial pressure of hydrogen will apparently further decelerate the HOR.

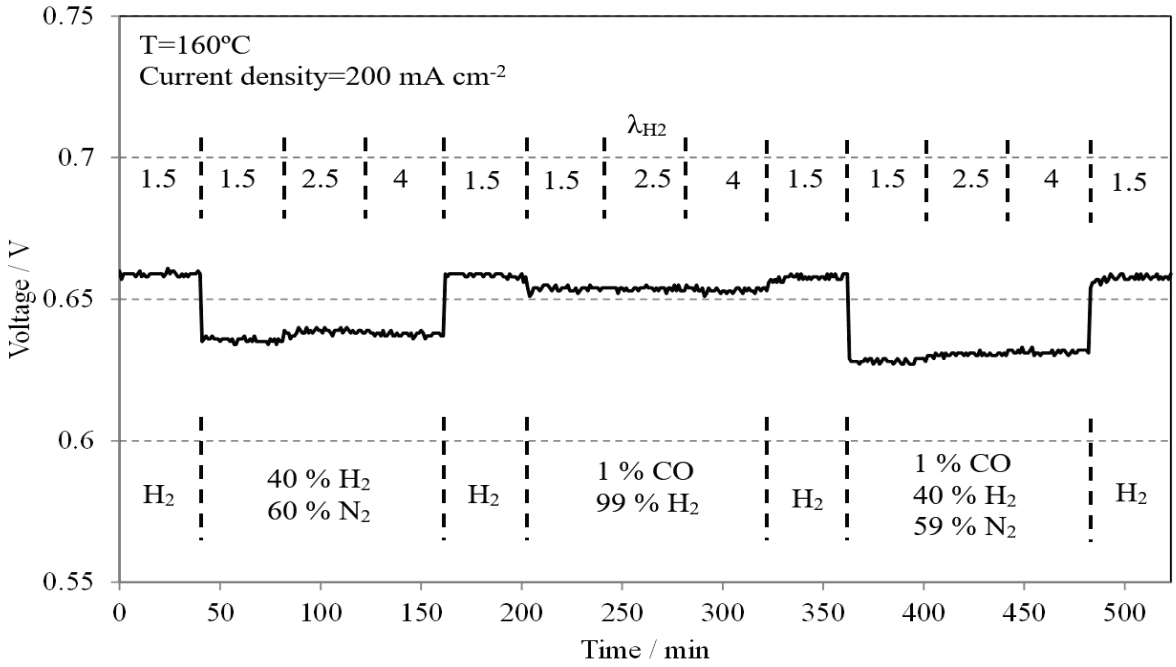

Figure 2. Evolution of the cell voltage at a constant current density of 200 mA cm^{-2} when varying the composition and the stoichiometry of the fuel as indicated in the figure legends. The measurements were performed at 160 ºC, ambient pressure and air as oxidant (λ_{O2} = 2).

It is worth highlighting that the fast recovery of the cell voltage when switching back to pure H_2 after steps of H_2 dilution and CO poisoning seems indicating the physical nature of the hydrogen as well as CO adsorption on Pt at elevated temperatures. Additionally, the catalytic layer was constructed from bare Pt/C particles, as no polymeric or ionomeric binder was used in the catalyst layer where the ionic conductivity is achieved by the phosphoric acid diffused from the PBI membrane. Therefore, the diffusion of the gases through the catalytic layer should be enhanced for a binderless catalytic layer, which is assumed to facilitate the CO and N_2 removal leading to a quicker transient voltage. The same reason is given for the fast voltage drop observed in Figure 2 when other fuel compositions are changed from pure H_2.

3.2 Effect of dilution of hydrogen at varied CO contents

Up to now only one CO poisoning level i.e., 1% CO has been discussed in combination with several H_2 dilutions i.e. 20 – 80 vol% H_2. A variety of CO concentrations and H_2 dilution by other gas components in reformate fuels are to be considered in this section. A wide range of CO contents is studied, as shown in Figure 3, where polarization curves of MEAs fed with fuels with CO contents from 0 up to 2.0% in combination with the H_2 dilution between 20 and 60% are presented. Again, a new MEA was built for each set of measurements in this series of measurements.

The results show that a major contribution to the voltage loss, as compared with pure H_2 fueling, is the hydrogen dilution, so are the CO poisoning effects from concentrations from 0.5 – 2.0% CO in the fuel streams containing 20% H_2 (Figure 3a), 40% H_2 (Figure 3b) and 60% H_2 (Figure 3c). The measurements were performed at 160 ºC, constant stoichiometries (λ_{H2} = 1.5, λ_{O2} = 2) and ambient pressure.

Thus, the higher the H_2 dilution or the lower the H_2 volume concentration the greater the voltage loss with respect to the pure H_2 performance. In the study of the CO poisoning, the CO

volume concentration range was selected the same, i.e., from 0.5 to 2.0%, for all H_2 dilution levels. As a consequence of the H_2 dilution, it is the [CO]/[H_2] volume ratio that governs the CO poisoning, which changes significantly when increasing the H_2 dilution i.e., lowering the H_2 volume concentration. Thus, for the H_2 dilution of 20%, the [CO]/[H_2] volume ratio corresponding to the range of 0.5 – 2.0% CO is from 0.5/20 – 2/20. For the H_2 dilution corresponding to 60% H_2, this [CO]/[H_2] ratio diminishes significantly to 0.5/60 – 2/60 for the same range of 0.5 – 2% CO. In other words, for 20 and 60% H_2, the range 0.5 – 2% CO referred to the total volume of the mixture of gases is equivalent to 2.4 – 9.1 and 0.8 – 3.2% CO when referred to CO in pure H_2, respectively. This explains the different tolerance towards CO observed at high and low H_2 dilutions for the same range of CO volume concentration.

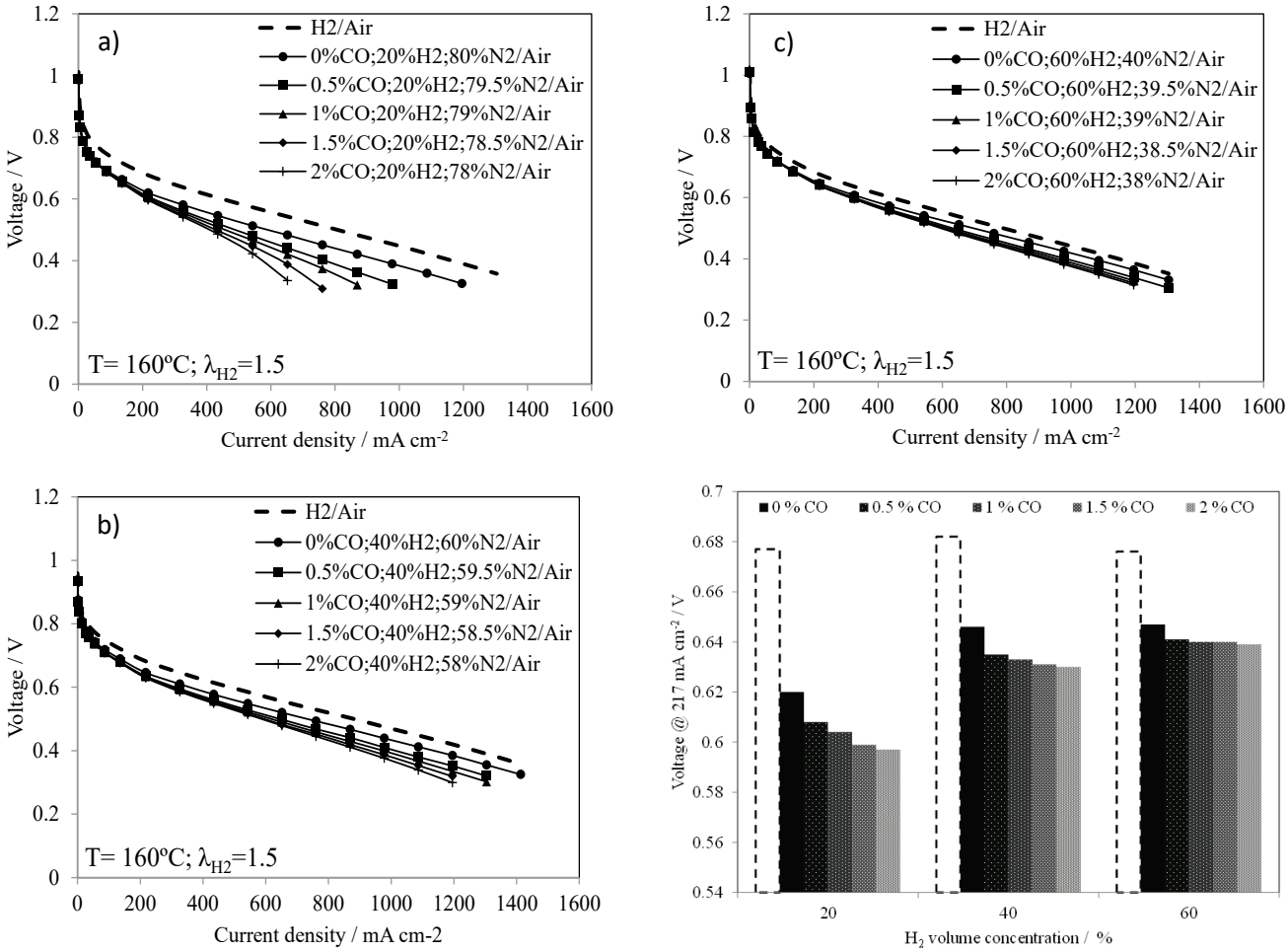

Figure 3. Polarization curves of MEAs when the cathode was supplied with air and the anode was fueled with CO concentrations ranging from 0.5 – 2 vol% CO and H_2 concentrations of a) 20 vol%, b) 40 vol% and c) 60 vol%, all balanced with N_2. The measurements were performed at 160ºC, constant stoichiometries (λ_{H2} = 1.5, λ_{O2} = 2), ambient pressure and the anode Pt loading of 1.3 $mg_{Pt}cm^{-2}$.

Figure 3d summarizes the cell voltage loss due to the fuel dilution and CO poisoning at a current density of 217 mA cm^{-2}, compared to the voltage of pure hydrogen operation. The hollow bars with dashed line represent the cell voltage for pure H_2 feeding, which were ranging from 0.677-0.681 V. It can be seen from the figure that a noticeable voltage drop associated to the dilution of H_2 by N_2 (at 0% CO) accounts for about 8 % of voltage decrease at high H_2 dilution (20% H_2) and 4 % at low hydrogen dilution (60% H_2).

In the figure, it can also be seen that the voltage drop was associated to the CO poisoning at different concentrations from 0.5 to 2.0 vol% CO. For the fuel dilution of 60% H_2, increasing the CO content from 0.5 up to 2.0 % has practically a negligible effect, as the cell voltage decreases from 0.641 to 0.639 V i.e., only 0.3 % of the voltage loss. In the case of 40% H_2, the decrease in voltage is also very low, decreasing from 0.635 V down to 0.630 V i.e., 0.8 % of the voltage loss when the CO volume concentration increases from 0.5 up to 2.0 %. It is of note that these cell voltage values for the MEAs of the present work are quite high, compared to literature works as recently reviewed by Aili et al.[27] A stronger CO poisoning effect is observed at 20% H_2 where the [CO]/[H_2] ratio increases from 0.5/20 (equivalent to 2.4% CO in pure H_2) up

to 2/20 (equivalent to 9.1% CO in pure H_2). This high effective CO content causes a voltage drop by nearly 2% i.e., from 0.608 to 0.597 V in the concentration range of 0.5 – 2.0% CO.

In the light of these results, it can be concluded that the CO poisoning in the range of 0.5 – 2.0% has demonstrated a negligible effect compared to the voltage drop associated to the H_2 dilution. Thus, for the lower H_2 dilution scenario (60% H_2), only 0.3% of voltage loss is observed when increasing the CO volume concentration from 0.5 up to 2.0 %, which should be compared to about 4% of the voltage loss caused by the hydrogen dilution, as discussed above.

3.3 Effect of the platinum loading on pure H_2 performance

The state-of-the-art anode platinum loading for HT-PMFCs is relatively high, typically above 0.7 mg_{Pt}/cm^2 and great efforts are being made to reduce the Pt loading down to levels of ≤ 0.3 $mg_{Pt}cm^{-2}$ or even ≤ 0.1 mg_{Pt} cm^{-2}.[27] Low Pt loading electrodes covering a range from 0.15 to 1.3 $mg_{Pt}cm^{-2}$ were prepared and evaluated for the anode performance with pure hydrogen, diluted hydrogen and CO poisoning.

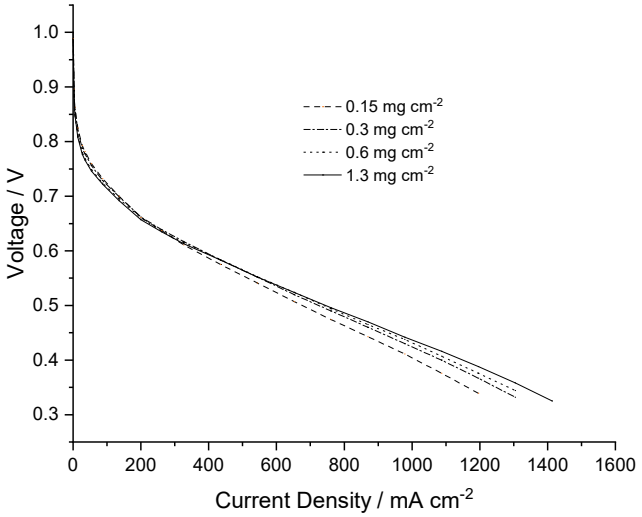

Figure 4. The I-V performance of HT-PEMFCs with different anode Pt loadings under operation with pure H_2 and air at 160 °C and ambient pressure.

Operating with pure hydrogen, the I-V performance of HT-PEMFCs at 160°C is shown in Figure 4. Briefly speaking, a ten-fold reduction in the Pt loading from 1.3 to 0.15 $mg_{Pt}cm^{-2}$ does not result in any visible performance change in the practical current density of operation. This will serve as a baseline for the following study of hydrogen dilution and CO poisoning.

3.4 Effect of varying Pt loading on the CO poisoning

This section is devoted to a study of the CO poisoning with low Pt loading electrodes on pure hydrogen with further dilution. The studied CO contents were from 0.25 to 2.0% in H_2 and the anodes were made with Pt loadings ranging from 0.15 to 1.3 $mg_{Pt}cm^{-2}$. The as-measured I-V curves are presented in Figure S1 in the Supplementary Information. From the I-V curves, the cell voltage values were read at a current density of 0.2 A cm^{-2} and plotted in Figure 5 as a function of the CO concentration.

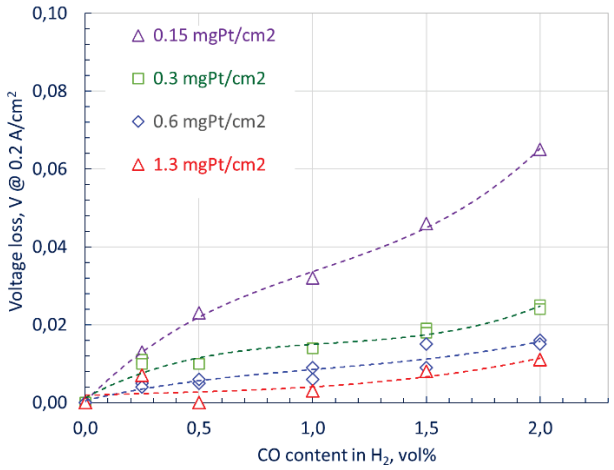

Figure 5. Cell voltage losses at 0.2 $mAcm^2$ due to addition of CO to pure hydrogen at varied concentrations. Data were obtained from I-V curves measured at 160°C with anodes of different Pt loadings as indicated in the figure.

It is clearly seen from the figure that the CO poisoning effect in the whole concentration range is enhanced as the Pt loading of the anode decreases. This seems apparent as the Pt loading of the anode is related to the total available active sites of the catalysts, though the Pt utilization, and therefore the specific e.g., mass based surface area, will be higher for the lower Pt loading electrodes. Attempt was made to normalize the CO poisoning effect by multiplying the voltage loss by the Pt loading. The resultant cell voltage loss due the CO poisoning seems approximately correlated with the total active sites, as seen from Figure S2. Further study by the electrochemically active surface area, by means of CO stripping, for example, is planned.

3.5 Effects of hydrogen dilution on CO poisoning with low Pt loading electrodes

A low Pt loading of 0.3 $mg_{Pt}cm^{-2}$ at the anode was selected for the CO poisoning studies with hydrogen contents from 40, 60, 80 and 100% balanced by argon. Figure 6 shows a set of the measurements comparing the CO poisoning in 100% and 40% H_2 where the CO content was varied from 0 to 2.0%. Similar measurements will diluted hydrogen at 60% H_2 and 80% H_2 can be found in Figures S3&4 .

At this low Pt loading, the anode showed a performance loss around 10 mV at current density of 200 $mAcm^{-2}$ when up to 2.0% CO is present in pure hydrogen. When hydrogen is diluted with an inert gas e.g., argon or nitrogen, the CO poisoning effect becomes much larger. As seen from the figure for 40% H_2, the presence of 0.25% CO had already a noticeable performance loss while 1.0 and 2.0% CO in 40% H_2 caused a voltage loss of 45 and 130 mV, respectively, for the low Pt loading anode with 0.3 $mg_{Pt}cm^{-2}$.

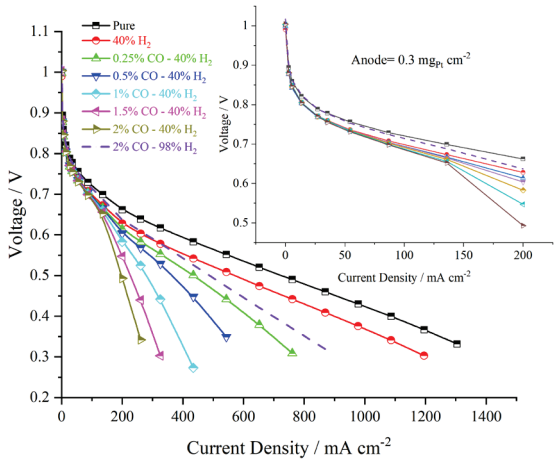

Figure 6. I-V curves of HT-PEMFCs with anodes of a fixed Pt loading of 0.3 $mg_{Pt}cm^{-2}$. The anode feeding gas includes 100% H_2 and 40%H_2 with a variety of CO contents from 0.25 to 2.0%CO, as indicated in the figure. T = 160°C, λ_{H2} = 1.5 and λ_{Air} = 2.0 at current densities > 200 mA cm^{-2}.

3.6 Further discussion of the results

To summarize the discussion above, the two effects of the hydrogen dilution and CO poisoning are significantly exaggerated when the Pt loading is lowered. Figure 7 summarizes the inert gas dilution effect of the anode performance of HT-PEMFCs at varied Pt loadings of the anode.

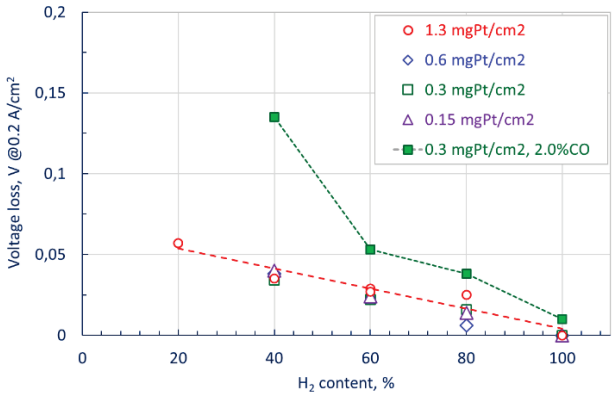

Figure 7 Cell voltage losses at 0.2 $mAcm^2$ due to the hydrogen dilution in the absence of CO as well as the presence of 2.0% CO. data were obtained from I-V curves measured at 160°C with anodes of varied Pt loadings as indicated in the figure.

In the absence of CO, the hydrogen dilution by an inert gas e.g., nitrogen or argon causes anode performance losses. Switching from 100% H_2 to 60% H_2, for example, all four electrodes exhibited a lowered performance by ca. 25 – 30 mV, which is not very sensitive to the Pt loading. When CO is present in the fuel steam, the combined effects on the hydrogen dilution and CO poisoning becomes substantial for the low Pt loading electrode. For anodes of 0.3 $mg_{Pt}cm^{-2}$, 2.0% CO in a 40% H_2 fuel stream can lead to an anode voltage loss as high as 130 mV.

The combination of the hydrogen dilution and CO poisoning can be expressed as the ratio [CO]/[H_2], which, in turn, determines the Pt surface coverage by CO and hence the fraction of the active sites available for the hydrogen oxidation. An expression of the Pt surface coverage is, however, a complicated function involving the dissociative adsorption of hydrogen and its competition with CO and other adsorptive species such as the dissociated water (-OH_{ad}) and the acidic anion ($H_2PO_4^-$) [28,29], though different models have been suggested to correlate the CO coverage on the Pt catalyst surface.[30, 31]. A simplified correlation of the anode performance loss with the [CO]/[H_2] ratio is presented in Figure 8. A strong dependence of the anode performance loss can be seen on the [CO]/[H_2] ratio, in an exponential form,which has also showed clear trends with the Pt loading of the anode.

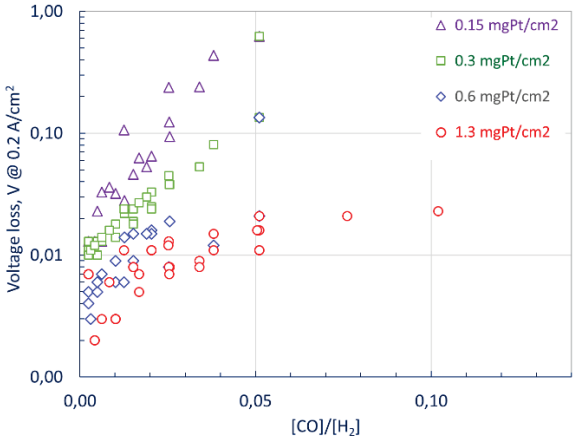

Figure 8. Cell voltage losses as a function of the [CO]/[H_2] ratio due to the hydrogen dilution by in the absence of CO as well as presence of 2.0% CO. The data were obtained from the I-V curves at 0.2 $mAcm^2$ at 160 °C with anodes of varied Pt loadings as indicated in the figure.

4. Conclusions

The CO tolerance in high-temperature polymer electrolyte membrane fuel cells has been experimentally investigated at 160 °C, the typical operating temperature of the technology. The investigation focuses on the CO poisoning in hydrogen-rich reformat fuels where a significant amount of inert gas components is present causing the hydrogen dilution. Another concern is the recent development of low Pt loading electrodes and their tolerance towards fuel impurities.

Under a constant H_2 stoichiometry (λ_{H2} = 1.5) the fuel cell performance degradation caused by 1.0% CO is found to be intensified by the hydrogen dilution in a range of 20 – 80 vol% H_2. The CO tolerance was evaluated in a wide range of 0.5 – 2.0 vol% CO together with different levels of H_2 dilution (20 – 60 vol%). A major contribution to the anode performance loss is found to be from the H_2 dilution. For H_2 dilution of 40 and

60 vol%, an increase in the CO concentration from 0.5 up to 2.0 vol%, on the other hand, triggered negligible further voltage losses i.e. less than 1% at an operational current density of around 200 $mAcm^{-2}$.

Both the hydrogen diluting and CO poisoning effects are significantly exaggerated for electrodes of low Pt loadings, which limit the overall available active sites of the catalysts and hence the sensitivity towards the strong CO adsorption. Technological feasibility of the low Pt loading anodes, currently under active development, should be assessed under scenarios of utilizing reformat fuels containing CO.

Acknowledgement

This work was financially supported by Energy Technology Development and Demonstration (EUDP) Program (COBRA-Drive, 64018-0118), Denmark**.**

References

1. B. G. Pollet, S. S. Kocha and I. Staffell, Curr Opin Electrochem, 16 (2019), 90–95.
2. Y. Wang, D. F. Ruiz Diaz, K. S. Chen, Z. Wang and X. C. Adroher, Materials Today, 32 (2020), 178–203.
3. T.E. Springer, T. Rockward, T. Zawodzinski, S. Gottesfeld, J. Electrochem. Soc. 148 (2001) A11-A23.
4. S. Jimenez, J. Soler, R.X. Valenzuela, L. Daza, J. Power Sources 151 (2005) 69-73.
5. H.P. Dhar, L.G. Christner, A.K. Kush, H.C. Maru, J. Electrochem. Soc. 133 (1986) 1574-1582.
6. Q. Li, R. He, J.O. Jensen, N.J. Bjerrum, Fuel Cells 4 (2004) 147-159.
7. J. Zhang, Z. Xie, J. Zhang,Y. Tang, C. Song, T. Navessin, Z. Shi, D. Song, H. Wang, D.P. Wilkinson, Z.-S. Liu, S. Holdcroft, J. Power Sources 160 (2006) 872-891.
8. Q. Li, R. He, J.-A. Gao, J.O. Jensen, N.J. Bjerrum, J. Electrochem. Soc. 150 (2003) A1599-A1605.
9. P. Krishnan, J.-S. Park, C.-S. Kim, J. Power Sources 159 (2006) 817-823.
10. S.K. Das, A. Reis, K.J. Berry, J. Power Sources 193 (2009) 691-698.
11. Yao, D., Zhang, W., Ma, Q., Xu, Q., Pasupathi, S., Su, H. J. Power Sources 426 (2019), 124-133
12. Liu, F., Mohajeri, S., Di, Y., Wippermann, K., Lehnert, W. Fuel Cells 14(2014), 750-757
13. Liang, H., Su, H., Pollet, B.G., Linkov, V., Pasupathi, S. J. Power Sources 266 (2014), 107-113
14. Liang, H., Su, H., Pollet, B.G., Pasupathi, S. J. Power Sources 288(2015), 121-127
15. Úbeda, D., Cañizares, P., Ferreira-Aparicio, P., Chaparro, A.M., Lobato, J., Rodrigo, M.A. Int. J. Hydrogen Energy 41 (2016), 20294-20304
16. S. Martin, Q. Li, T. Steenberg, J.O. Jensen, J. Power Sources 272 (2014) 559-566.
17. Martin, S., Garcia-Ybarra, P.L., Castillo, J.L.: Electrochem. Commun. 93(2018), 57-61
18. Martin, S., Jensen, J.O., Li, Q., Garcia-Ybarra, P.L., Castillo, J.L.: Int. J. Hydrogen Energy 44(2019), 28273-28282
19. Martin, S., Li, Q., Jensen, J.O. J. Power Sources 293(2015), 51-56
20. A.D. Modestov, M.R. Tarasevich, V.Y. Filimonov, E.S. Davydova, Electrochim. Acta 55 (2010) 6073-6080.
21. J.J. Linares, C. Sanches, V.A. Paganin, E.R. Gonzalez, Int. J. Hydrogen Energy 37 (2012) 7212-7220.
22. A. Bergmann, D. Gesteisen, T. Kurz, Fuel Cells 10 (2010) 278-287.
23. K. Kwon, D.Y. Yoo, J.O. Park, J. Power Sources 185 (2008) 202-206.
24. S. Ahmed, M. Krumpelt, Int. J. Hydrogen Energy 26 (2001) 291-301.
25. T.A. Semelsberger, R.L. Borup, Int. J. Hydrogen Energy 30 (2005) 425-435
26. Q. Ming, T. Healey, L. Allen, P. Irving, Catal. Today 77 (2002) 51-64.
27. D. Aili, D. Henkensmeier and S. Martin et al. Electrochemical Energy Reviews 3(2020), 793–845
28. He, Q.G., Shyam, B., Nishijima, M., Ramaker, D., Mukerjee, S. J. Phys. Chem. C 117 (2013), 4877-4887
29. Kaserer, S., Caldwell, K.M., Ramaker, D.E., Roth, C. J. Phys. Chem. C117 (2013), 6210-6217
30. H. Igarashi, T. Fujino, and M. Watanabe, J. Electroanal. Chem., 391 (1995), 119.
31. W. Vogel, J. Lundquist, P. Ross, and P. Stonehart, Electrochim. Acta, 20 (1975), 79.

CO Poisoning in High Temperature Polymer Electrolyte Membrane Fuel Cells Operating with Diluted Hydrogen and Low Pt Loading Electrodes

Sanser Celenk,[1] Santiago Martin,[1,2] Lars N. Cleemann,[3] Jens Oluf Jensen[1] and Qingfeng Li*,[1]

Supporting information

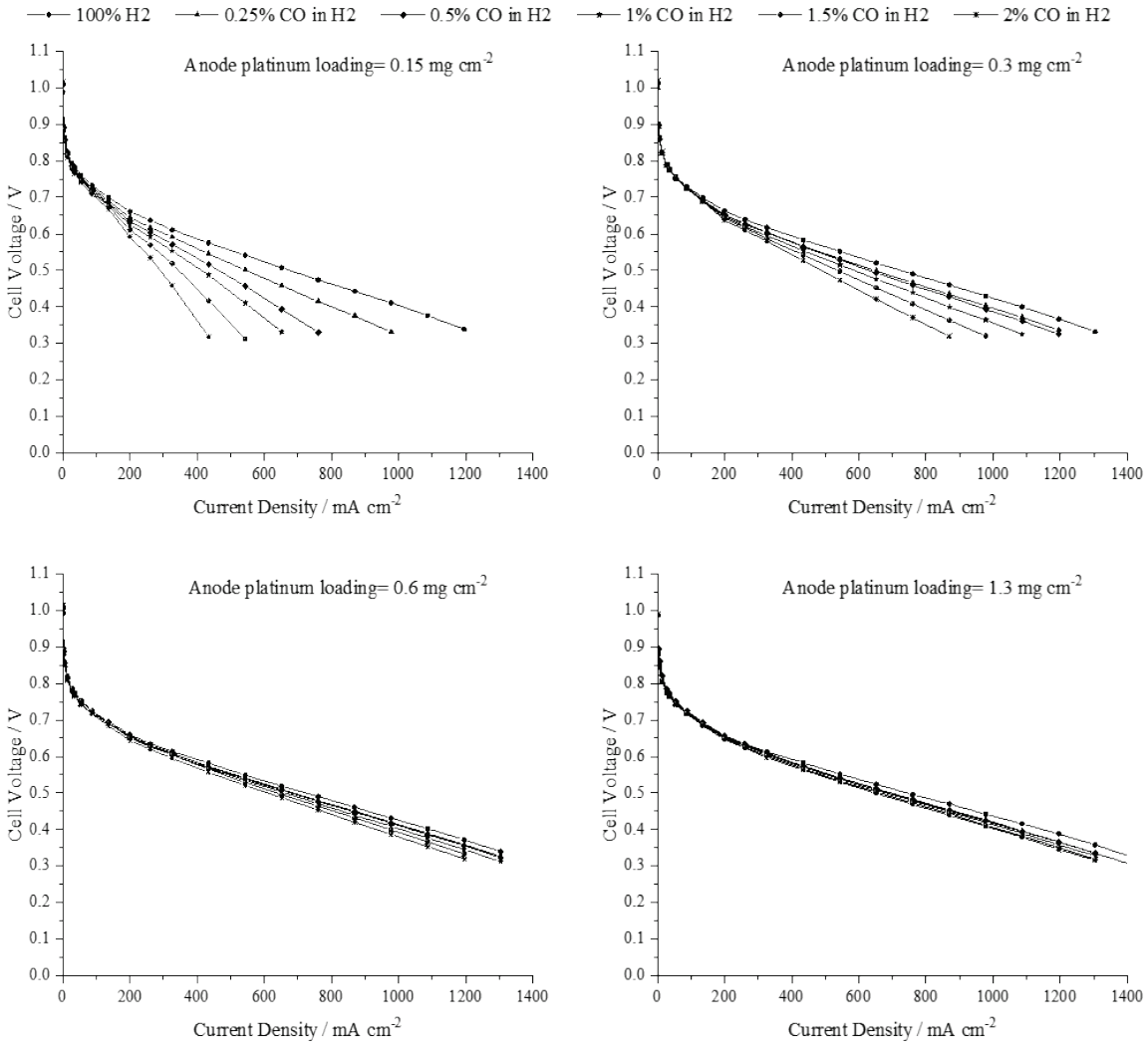

Figure S1. Polarization curves of MEAs when the anode was prepared with varied Pt loadings a) 0.15 mg_{Pt}/cm^2; b) 0.3 mg_{Pt}/cm^2; c) 0.6 mg_{Pt}/cm^2; d) 1.3 mg_{Pt}/cm^2. The anode fed fuels are indicated in the figure.

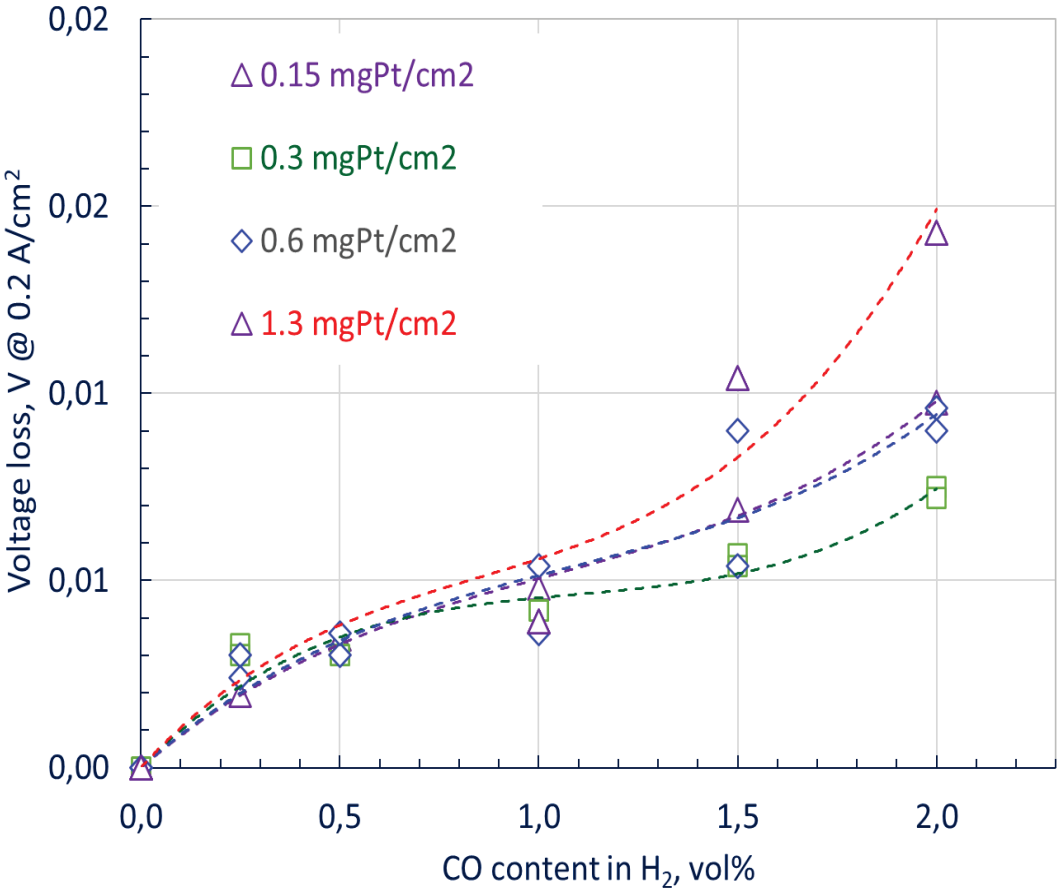

Figure S2. Pt-loading normalized cell voltage losses at 0.2 $mAcm^2$ due to addition of CO to pure hydrogen at varied concentrations. Data were obtained from I-V curves measured at 160°C with anodes of different Pt loadings as indicated in the figure.

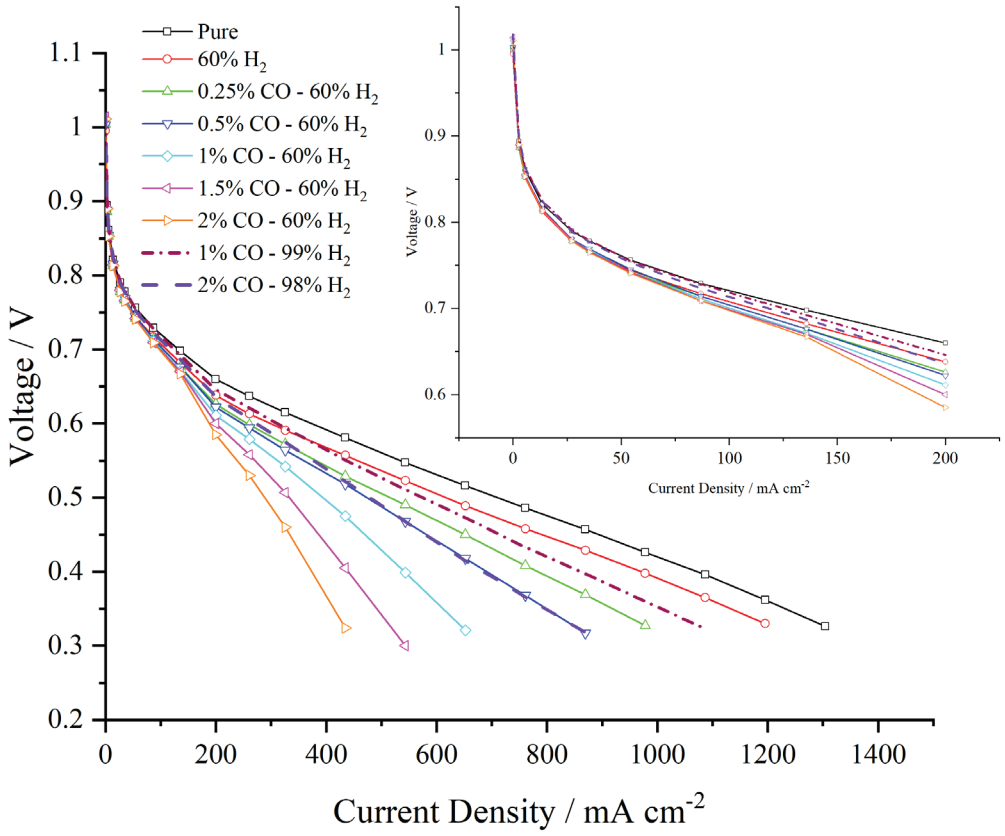

Figure S3. Impacts of hydrogen dilution and CO poisoning in 60%H_2 on the fuel cell I-V curves when the anode Pt loading was fixed at 0.3 mg_{Pt}/cm^2. Inset graphs show the low current density region from 0 to 200 mA/cm^2.

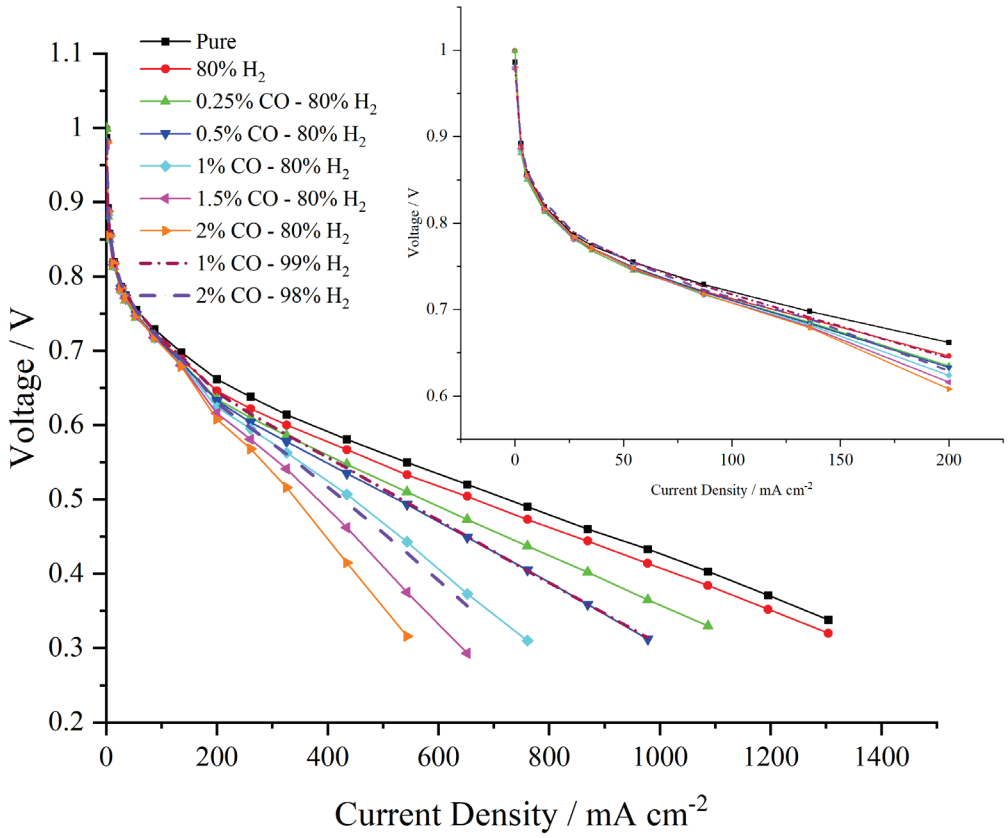

Figure S4. Impacts of hydrogen dilution and CO poisoning in 80%H_2 on the fuel cell I-V curves when the anode Pt loading was fixed at 0.3 mg_{Pt}/cm^2. Inset graphs show the low current density region from 0 to 200 mA/cm^2.

MANUSCRIPT 2

[redacted]

Hydrogen Oxidation and Evolution Kinetics in the Absenceand Presence of Carbon Monoxide for High Temperature Polymer Electrolyte Membrane Fuel Cells

Sanser Celenk, Lars N. Cleemann, Jens Oluf Jensen and Qingfeng Li

Received 00th January 20xx,
Accepted 00th January 20xx

DOI: 10.1039/x0xx00000x

Hydrogen Oxidation and Evolution Kinetics in the Absence and Presence of Carbon Monoxide for High Temperature Polymer Electrolyte Membrane Fuel Cells

Sanser Celenk,[1] Lars N. Cleemann,[2] Jens Oluf Jensen[1] and Qingfeng Li*,[1]

Abstract

The hydrogen oxidation and evolution reaction behavior on Pt/C electrodes is studied in phosphoric acid doped polybenzimidazole electrolytes at temperatures from 120 to 180 °C in the absence and presence of carbon monoxide. Ultralow Pt loading electrodes of 1.5-6.5 $\mu gPt/cm^2_{Geo}$ are used in hydrogen pumping cells for the study, allowing for minimizing the mass transport and eliminating the ohmic resistance contributions to the kinetic behaviors. Fitting with the Butler–Volmer equation kinetic parameters including exchange current density, transfer coefficient and activation energies are obtained, showing that the HOR, but not HER, rate is limited by the Tafel step. In the presence of CO severely asymmetric Tafel plots for HER/HOR are observed. The strong adsorption of CO on the Pt surface hampers the HOR kinetics by further limiting the slow dissociative hydrogen adsorption.

1. Introduction

The H_2 oxidation reaction (HOR) kinetics is very facile in acidic electrolytes, with Pt and Pd as the most active and stable catalysts.[1] In proton exchange membrane fuel cells (PEMFC), lowering the anode Pt loading from 0.4 to 0.05 $mg_{Pt}cm^{-2}$ was reported to give a cell voltage loss of only 5–15 mV at current density of 1.2 A/cm^2.[2] In high temperature PEMFCs based on acid doped polybenzimidazole membranes operating at 180°C, reduction of the anode Pt loading from 0.9 to 0.05 or even down further to 0.025 $mg_{Pt}cm^{-2}$ has shown negligible performance losses.[3]

Kinetically the HOR on Pt is assumed to proceed by either Tafel-Volmer or Heyrovsky-Volmer mechanisms. The Tafel-Volmer mechanism involves the potential-independent dissociative adsorption of hydrogen (the Tafel step) followed by the electrochemical oxidation of H ad-atoms in the Volmer step:

$$H_2 + 2Pt \rightleftharpoons 2Pt\text{-}H_{ads} \qquad \text{Tafel step} \qquad (1)$$

$$2Pt\text{-}H_{ads} \rightleftharpoons 2Pt + 2H^+ + 2e^- \qquad \text{Volmer step} \qquad (2)$$

The Heyrovsky-Volmer mechanism involves the electrochemical formation of adsorbed hydrogen atoms, which is also followed by the above Volmer step:

$$H_2 + 2Pt \rightleftharpoons Pt\text{-}H_{ads} + H^+ + e^- \qquad \text{Heyrovsky step} \qquad (3)$$

Either the Tafel or the Heyrovsky step is the rate determining step while the Volmer reaction is a facile charge transfer step.

Early studies on HOR kinetics were conducted using rotating disk electrodes (RDE) in liquid electrolytes. Due to the extremely fast HOR kinetics, the estimation of ohmic and mass-transport resistances is essential for the studies. Kinetic parameters for the HOR i.e. the exchange current density (i^o in A/cm^2_{Pt}) and its corresponding activation energy (E_a in kJ/mol) as well as the Tafel slope, have been evaluated. The early year work [4-7] on single or polycrystalline Pt electrodes reported an exchange current density of about 1 mA/cm^2_{Pt} and a Tafel slope of 28–30 mV/decade. This number of the exchange current density is about 6-7 orders of magnitude higher than that for the oxygen reduction reactions (ORR), and have been widely used in later or even recent studies [8-13].

These results based on RDE in liquid electrolytes were however inaccurate [14 - 16] due to the effect of H_2 mass transport rates. To improve the measurements of the HOR, as well as the hydrogen evolution reaction (HER) kinetics, it is desired that the kinetic voltage losses are significant while both the ohmic and mass transport contributions are limited. This can be achieved by using gas diffusion electrodes (GDE) with ultralow Pt loadingds [17-20] where the mass-transport contribution is negligible.

Neyerlin et al.[19] used membrane-electrolyte-assemblies (MEAs) for PEMFCs with asymmetric Pt loadings of the electrodes to measure current-voltage curves in a hydrogen pumping cell. The low Pt loading (0.003 $mgPt/cm^2$) electrode

1. Department of Energy Storage and Conversion, Technical University of Denmark, Fysikvej B310, 2800 Lyngby, Denmark.
2. Blue World Technologies, Egeskovvej 6C, 3490 Kvistgård, Denmark.

* Correspondance: kaz@blue.world; qfli@dtu.dk

was used as the working electrode while the high Pt loading (0.4 mgPt/cm^2) electrode as the counter and reference electrode. The kinetic losses at the high Pt-loading electrode was assumed, and experimentally proved, to be negligible in the small voltage or current density range of the study. The measured voltage is hence the overpotential of either HOR or HER on the working electrode.

With this type of hydrogen pump cells using low Pt loading GDE [15-20] or similar electrodes [21,22,23,24], exchange current densities for HOR on carbon supported Pt nanoparticles have been measured to be in a range of 100-800 mA/cm$^2_{Pt}$, which is about two orders of magnitude higher than the results obtained using single or polycrystalline Pt electrodes in liquid electrolytes.

Mechanisms of the CO poisoning on HOR electrodes is that CO preferably adsorbs on the platinum surface under normal anode operating potentials, with an adsorption enthalpy of 134 kJ mol^{-1}, compared to 87.9 kJmol^{-1} for hydrogen.[25] The CO adsorption occurs via either linear or bridge site bonding depending on the CO coverage. The bridge bonding prevails at a surface coverage of less than 50% while the linear bonding at higher surface coverage.[28] When the CO coverage increases to a certain (threshold) extent, the electro-oxidation of CO may take place:

$$CO + H_2O \rightarrow CO_2 + 2H^+ + 2e^- \qquad E^o = -0.10\ V \qquad (3)$$

For pure platinum electrodes, however, any significant electro-oxidation of CO would need an overvoltage of at least 0.5 V [26].

A significant amount of work has been done for HOR, HER and CO poisoning on Pt/C catalysts in acidic electrolytes, however, at temperatures up to 80°C based on perfluorinated sulfonic acid e.g. Nafion membranes. The temperature range of the study can be extended to above 100°C in high temperature polymer electrolyte membrane fuel cells (HT-PEMFCs) using phosphoric acid doped PBI membranes. HT-PEMFCs operate at around 150-160°C [27] with methanol reformate as fuel. A major advantage of HT-PEMFCs is the enhanced catalyst tolerance toward fuel impurities e.g. CO [28], allowing direct use of methanol reformate, typically consisting of H_2, CO_2, H_2O and about 1% CO.[29] Studies with fuel streams containing CO of varied concentrations [30- 33] have been reported. In addition to the CO poisoning, the dilution effect of H_2 by CO_2, water vapor and other inert impurities [34,35] as well as combinations of them [36,37] have also been investigated. This work is devoted to a study of the HOR kinetics in the presence of CO in HT-PEMFC in a temperature range from 120 to 180 °C.

2. Experimental

2.1 Electrodes

Gas diffusion electrodes of varied Pt loadings have been prepared from Pt/C catalysts without using any binders, where the proton conductivity of the catalytic layers can be provided by liquid phosphoric acid diffusing from the membranes, as described previously.[38,39] The high (1.3 and 0.68 mgPt/cm^2) loading electrodes were made from 60 wt% Pt/C catalysts (HiSPEC 9100) and the medium (64 µgPt/cm^2) loaded electrode were prepared by 10% wt. Pt/C (HiSPEC 2000) supplied by Johnson Matthey. Low (6.5 and 1.5 µgPt/cm^2) Pt loading electrodes were prepared by diluting the catalyst (5% wt. Pt/C, Fuel Cell Store) with carbon black (Vulcan XC72R) in order to ensure the Pt catalyst dispersion over a certain thick layer. The catalysts were dispersed in 96% ethanol and had varying ink concentrations (mg$_{solid}$/mL). The catalytic inks were sonicated for up to 2 hours until they were stable. Once stable, the inks were sprayed onto a 5 cm x 5 cm gas diffusion layer (H23C2 Freudenberg), using an ultrasonic spraying robot (SonoTEK ExactaCoat, 120 kHz). The nozzle power was about 2 kW enough to atomize all of the inks. The spraying speed for the two electrodes with the highest loading was 0.25 mL/min^{-1}, while for the other electrodes, the deposition rate was 0.1 mL/min^{-1}. The gas diffusion layers (GDLs) were placed on a slightly heated plate at 40°C during spraying to allow the ethanol to evaporate slowly.

2.2 MEA preparation, cell assembling and test setup

The membranes used in this study were *m*-PBI membranes (Dapozol® 40 µm). To dope the PBI membranes, pieces were placed in 85% H_3PO_4 for at least one week at room temperature. Acid-doped membranes were then covered with polyimide sub-gaskets (Kapton®) with an opening area of 23 cm^2. MEAs were prepared on-site without hot-pressing, and 150 µm PTFE gaskets were used to prevent over-compression of the MEA.

A single cell was assembled using custom-made graphite flow plates with a serpentine flow field, gold coated copper current collectors and aluminum end plates. The assembly process involved using 12 pieces of M-8 steel bolts, which were gradually tensioned by applying torque in 7 steps. The final applied torque was 1.2 Nm.

2.3 Hydrogen pumping test

Prior to any kinetic measurements, MEAs were conditioned with break-in procedure at 160°C to reach a stable performance. In the fuel cell mode, the cathode loading was 1.3 mg cm^{-2}, same for all MEAs. Those highest loading cathode electrodes were serving as both a reference and a counter electrode in subsequent kinetic measurements. The other electrode was serving as the working electrode in the fuel cell mode. Except MEAs with ultra-low loaded (≈1.5–6.5 µgPt/cm^2) electrodes, MEAs were activated at a current density of 0.2 A cm^{-2} with a H_2 stoichiometry of 1.5 and air stoichiometry of 2 for 16 hours. For the MEAs with ultralow Pt loading anodes, a modified break-in procedure was used. These MEAs were activated with a potentiostatic break-in at a voltage of 0.65 V,

with the same flow rates, temperature and duration as the standard break-in procedure. The voltage of 0.65 V corresponds to an average cell voltage in our standard break-in procedure. After the activation of MEAs, potentiodynamic polarizarition curves were recorded from OCV to 0.4 V with a rate of 1 mV s^{-1}. The I-V curves were recorded with constant H_2 and air flow rates of 800 ml min^{-1}.

For comparison, electrodes with other Pt loadings (0.68-0.064 mg cm^{-2}) were also tested as working electrodes. During the kinetic measurements, a mixture of H_2 and water vapor was supplied to the reference electrode. The flow rate of H_2 was kept constant at 800 ml min^{-1}. The reference feed was humidified with water vapor at a water vapor partial pressure of 0.16 atm to prevent drying of the membrane. A partial pressure of 0.16 atm approximately corresponds to fuel cell operation at 0.2 A cm^{-2} with an air stoichiometry of 2. The reference electrodes were supplied with 2000 ml min^{-1} of H_2.

The HOR/HER kinetic measurements were performed at temperatures ranging from 120 to 180 °C. Anodic and cathodic voltammograms with a sweep rate of 2 mV s^{-1} were recorded between H_2 pump voltage of -0.4 and 0.4 V. After conducting an anodic scan from OCV to 0.4 V, the H_2 pump was relaxed at OCV for around 5 minutes, then a further cathodic scan from OCV to -0.4 V was recorded. Some of the scans were repeated with a reference electrode flow rate of 400 ml min^{-1} to ensure reproducible results. In the following, the H_2 pump cell voltage will be specified as V vs. RHE.

2.4 HOR/HER in the presence of CO

CO poisoning measurements were conducted after the kinetic measurements with pure H_2. The H_2 flow rate was kept constant at 400 ml min^{-1}, while the flow rate of CO was adjusted based on the CO content in H_2. The amount of CO in the reference electrode was investigated at concentrations of 0.25%, 0.5%, 1%, and 2% CO. CO and H_2 were mixed by using a gas mixing chamber (Bronkhorst®). Before taking measurements at any poisoning level, the cell relaxed at OCV for minimum of 15 minutes for the CO poisoning equilibrium. The same measurement procedure was utilized as in the pure H_2 part. Moreover, all measurements with CO were conducted twice to confirm CO poisoning equilibrium.

2.3 Electrochemical active surface area determination by CO stripping

In order to estimate the real surface of the electrodes, the voltammetric CO stripping was utilized at 40 °C. During the voltammetry, the counter/reference electrode was fed by pure H_2 while the working electrode was fed by 10 Vol% CO in N_2. The cell voltage was kept at 0.15 V for about 20 minutes. It was followed by 10 minutes of N_2 purging in order to get rid of the unadsorbed CO from the system. After the purging, the potential was scanned between 0.15 V to 1 V with a scan rate of 20 mV s^{-1}. The second anodic scan was served as a baseline. The CO desorption peak in the first anodic scan integrated with respect to the second anodic scan.

2.4 Electrochemical impedance spectroscopy

Electrochemical impedance spectroscopy (EIS) was used in order to estimate and keep track of the cell resistance. EIS was conducted before and after a potential scan. The high frequency resistance (HFR) value from the spectra assumed as the total cell resistance. This value was later used to correct the I-V curve for the kinetic measurements.

3. Results and Discussion

3.1 HOR kinetics

3.1.1 Electrochemical active surface area normalization

The electrochemical active surface area (ECSA) of platinum is often determined from cyclic voltammetry (CV) by hydrogen underpotential deposition. For HT-PEMFCs, however, this measurement is interfered by the strong adsorption of acid anions in the vicinity of the hydrogen adsorption potential as well as the enhanced faradaic current of hydrogen evolution at elevated temperatures. Alternatively the CO stripping approach is preferred as it involves the electrooxidation of adsorbed CO at higher potentials than that of acid anion adsorption.[40] Side reactions such as the surface carbon oxidation and possible acid decomposition is compensated by subtraction of a reference CV e.g. the second cycle after the CO stripping, as shown in Figure 1.

It is assumed that a full coverage of a monolayer of adsorbed CO is achieved at 40 °C. The total charge for the oxidation of adsorbed CO is calculated by

$$Q_{CO} = \frac{1}{2\cdot\nu}\int_{0.4}^{1.0}(i_{1st} - i_{2nd}) \times dE \qquad (4)$$

where i_{1st} is the CO stripping current and i_{2nd} is the background current measured in the subsequent scan. Based on the Q_{CO} value the ECSA of platinum (A_{Pt}) can be estimated from the catalyst loading (L_{Pt}, mg_{Pt}/cm^2) and the geometric area of the electrode (A_{geo}) :

$$A_{Pt}\left(m^2_{Pt}/g_{Pt}\right) = \frac{0.1\cdot Q_{CO}\ (\mu C)}{420\left(\mu C/cm^2_{Pt}\right)\times L_{Pt}\left(mg_{Pt}/cm^2\right)\times A\ (cm^2)} \qquad (5)$$

Using this mass specific surface area (A_{Pt}, m^2_{Pt}/g_{Pt}) of platinum catalysts, the current density can be translated into the Pt surface area based value:

$$i_{Pt} = \frac{i_{Geo}}{10\cdot A_{Pt}\cdot L_{Pt}}$$

The ratio of A_{Pt}/A_{Geo} is also called the roughness factor of the gas diffusion electrode.

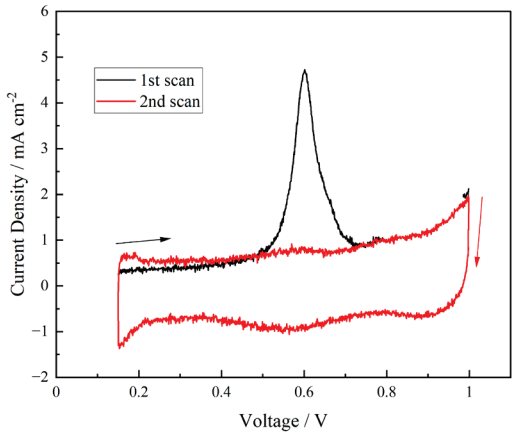

Figure 1. Cyclic voltammograms of CO stripping for determination of the active surface area. The CV was obtained at 40°C. The 1st scan was made after purging 10% CO in H_2 for 20 minutes when the cell voltage was held at 0. 15 V and the 2nd scan was subsequently made after the 1st.

3.1.2. Polarization curves for hydrogen pumping

A set of as-measured cell voltages for H_2 pumping is shown in Figure 2 for four electrodes of varied Pt loadings. In brief, the Tafel-Volmer mechanism is assumed i.e. involving a dissociative adsorption of hydrogen onto the platinum surface of the catalyst (Tafel reaction), followed by an electrochemical oxidation of the adsorbed hydrogen species (Volmer reaction). The reaction rate follows the Butler-Volmer kinetics expression at low HOR/HER overpotentials.

The cell voltage can be expressed as

$$E_{cell} = E_{rev} + iR_{total} + |\eta_{HER}| + |\eta_{HOR}| \quad (6)$$

where E_{Rev} is the reversible cell voltage and the ohmic voltage loss (iR_{total}) covers resistances primarily from the electrolyte membrane as well as the electrode catalyst layer due to the ion (proton) conductivity.

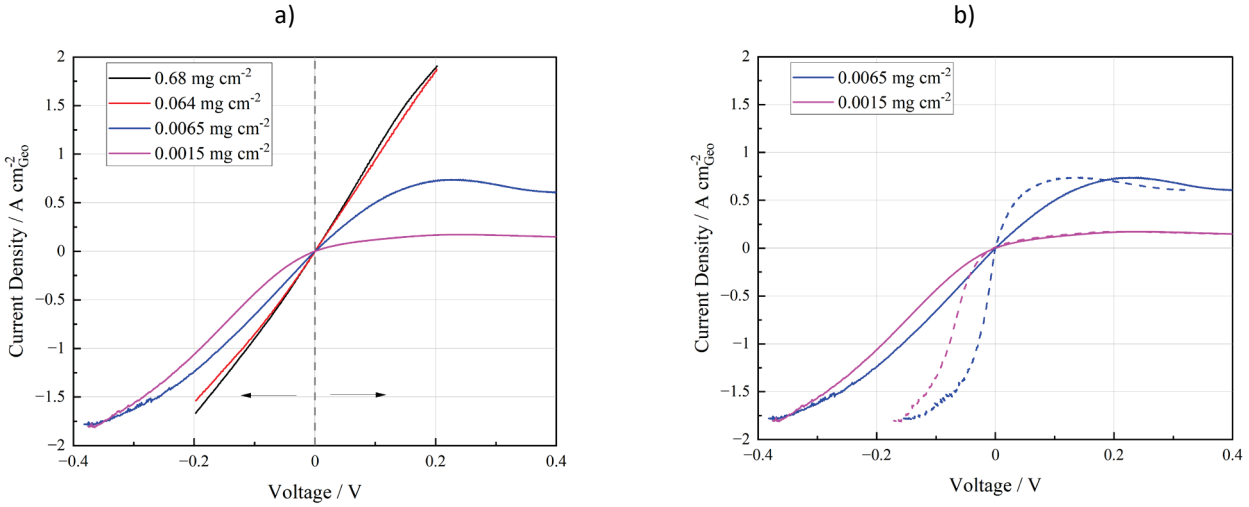

Figure 2. a) Polarization curves of hydrogen pumping with electrodes of varied Pt loadings at 160°C. The scan rate was 2 mV/s. b) iR-corrected polarization curves of low Pt-loading electrodes.

The reversible voltage of a hydrogen pumping cell is a function of the partial pressure of hydrogen in the cathode ($p^W_{H_2}$) and anode ($p^R_{H_2}$) chambers. For the present study, a hydrogen flow at rate of 2000 ml/min was supplied to the working electrode. To the reference electrode the hydrogen flow is 800 ml/min humidified with a water vapor partial pressure of 0.16 atm, which gives an open circuit voltage of ca. -3 mV, which was often observed during the measurements:

$$E_{Rev} = \frac{RT}{2F}\ln\left(\frac{p^W_{H_2}}{p^R_{H_2}}\right) = -0.003\ V \quad (7)$$

For cells with two electrodes of high Pt loadings (0.68 and 0.064 mg_{Pt}/cm^2_{Geo}), nearly identical cell voltages were obtained as seen from Figure 2a, indicating the nearly same overpotentials for both HOR and HER at these Pt loadings. In these measurements the opposite (counter and reference) electrode had always a Pt loading of 1.3 mg_{Pt}/cm^2_{Geo}, which contributes negligible overpotentials to the measurements. For the low Pt loading working electrode it is therefore assumed that:

$$\eta_{HOR} \approx E_{Cell} + iR_{total} \quad \text{or} \quad \eta_{HER} \approx -E_{Cell} - iR_{total} \quad (8)$$

i.e. for the low Pt loading electrodes, the overpotentials for the HOR or HER can be calculated from the measured cell voltage and the total ohmic resistance. 7

3.1.3. EIS and IR-compensation

The ohmic resistance of the hydrogen pumping cells was determined by EIS measurements. For LT-PEMFCs attempts were made to estimate the ionic (protonic) resistance of the catalyst layers using the ionomer fraction and overall electrode thickness, concluding that its contribution is negligible [20]. In the present study the high frequency resistance (HFR) from EIS measured was used as R_{total} which was within a range of 0.12 to 0.16 Ohmcm^2 at temperatures between 180 and 120 °C. Figure 2b illustrates the iR-corrected polarization curves for the two low Pt loading electrodes.
It has been reported that a strong dependence of the HFR on the polarization, i.e. the HFR was increasing from the OCV to either HER or HOR polarizations.[19] It is therefore proposed that use of the individual HFR to correct the overpotential at each current density is important for interpretation of the HOR/HER kinetics especially ay high polarizations. In the present study, the HFR at each temperature was found to be constant during the polarization test and hence the HFR obtained at OCV is used for the correction of overvoltage.

3.1.4. Limiting current

As also seen from Figure 2, for low Pt loading electrodes, the measured overvoltage deviates from the linear I-V behavior, showing a distinct limiting current density. On the anodic (HOR) side, this limiting current is more pronounced than on the cathodic (HER) side.

Assuming a gas diffusion electrode with a diffusion length of 200 µm, an average porosity of 50%, and a gas-phase H_2 diffusion coefficient of 0.5 cm^2/s, a limiting current density of the order of 100 Acm^2_{Geo} has been estimated.[19] It is clear that a hydrogen pumping cell should exhibit no gas phase mass transport resistances in the current density range of the measurements.

The origin of this limiting current density has been suggested to be due to the adsorption of hydrogen adatoms on the Pt surface i.e. the Tafel step, which is a completely potential independent process. It is seen that both the HER and HOR branches of the Tafel plots follow the Butler-Volmer equation at low overpotentials. In the HER branch, the kinetic data follow the Butler-Volmer fits over the entire measured potential range, indicating that the associative desorption of hydrogen from the catalyst surface is faster than the proton reduction step. In the HOR branch, however, the overpotential deviates from a simple Butler-Volmer relationship already at rather low overpotentials. This is more obvious from the measurements with higher H_2 partial pressures.[41] On the negative voltage side i.e. under HER conditions, however, the current exhibits a nearly linear increase with the voltage, i.e. with little limitation of mass transport for the HER kinetics.

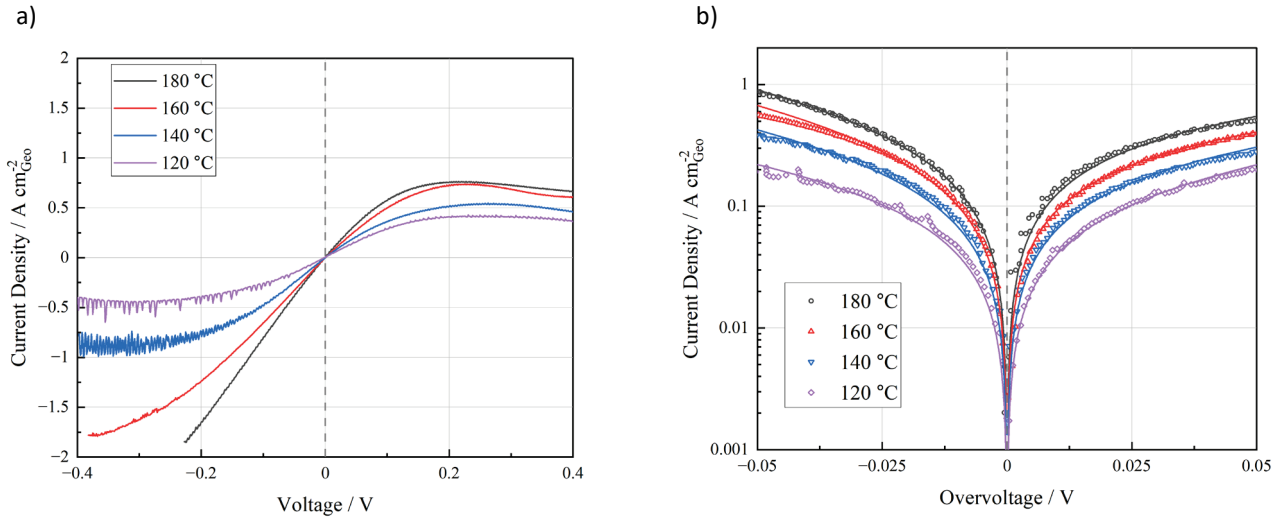

Figure 3. a) HOR and HER polarization curves for electrodes with 6.5 µmg$_{Pt}$/cm$^2_{Geo}$ at 120-180°C; b) Tafel plots of the same sets of data and their fit to the Butler–Volmer equation (lines).

3.1.5 Exchange current densities (i^0) and transfer coefficients (α)

In order to minimize the effect of limiting current densities on the kinetic analysis in the following, only data points with current densities of less than 10% of the corresponding limiting current density were used for fitting. In cases where the limiting current density cannot be determined a small voltage range from 0 to 30 mV was used.

To describe the HOR/HER kinetics and to estimate the kinetic voltage loss for gas diffusion electrodes, a Butler–Volmer equation was used

$$i = i^o_{Geo} \cdot \left(\exp\frac{\alpha_a F\eta}{RT} - \exp\frac{\alpha_c F\eta}{RT}\right) \quad (9)$$

where i^o is the exchange current density based on geometric electrode surface area in A/cm^2_{Geo}, α_a and α_c are the anodic and cathodic transfer coefficients, respectively. The Tafel slope, b, is defined as b = 2,303RT/αF. A constraint for $\alpha_a+\alpha_c$ =1 is applied for the fitting, hinting an assumption that the Tafel-Volmer mechanism is predominant. By fitting the iR-corrected polarization data using the Butler-Volmer equation (9), the exchange current density i^o_{Geo} was obtained.

Figure 3a shows a set of voltammograms obtained for electrodes with a Pt loading of 6.5 µgPt/cm^2 at temperatures from 120 to 180 °C. The same set of data is transposed into Tafel plots in Figure 3b. The HER/HOR polarization curves are nearly symmetric (as to be discussed below) in the potential range.

Attempt was also made to focus on a micropolarization region close to the HOR/HER equilibrium potential (η = ±10 mV), where the overall influence of any mass transport limitations are negligible. Within the region for small overpotentials, the linearized form of the Butler-Volmer equation was used:

$$i = i^o_{Geo} \cdot \frac{(\alpha_a+\alpha_c)F\eta}{RT} \quad (10)$$

Here, the exchange current density can be obtained from the slope in the current-potential plots when the sum of transfer coefficients is assumed to be 1 in the present work.

3.1.6 Arrhenius plot and activation energy

Figure 4 shows the Arrhenius plots of the exhange current density i^0 versus (1/T) for two electrodes of low Pt loadings. As seen from the figures the data follow straight lines in the Arrhenius plot, based on which the activation energy, E_a was estimated over the temperatures range from 120 to 180oC using the flowing equation:

$$\frac{\partial \log(i^o)}{\partial(1/T)} = -\frac{E_a}{2.303R} \quad (11)$$

Table 1 summarizes the results. Previous studies have determined the HOR/HER kinetics by the same H_2-pump approach [15.19.41], however, with PFSA membranes at typical temperatures of up to 80°C. It can be seen that the obtained i^0 value varied from 200 to 500 mA/cm^2Pt. In this comparison the results presented in this paper are slightly lower. A possible reason might be due to the electrolyte. Polymeric electrolytes based on perfluorosulfonic acid e.g. Nafion are super strong acids with pK_a of ca. -14 while phosphoric acid is mild acid with a pK_a of 2.16, The significant difference in the proton activity may affect the HOR/HER kinetics. Water vapor pressure or the atmospheric humidity in the test cell may also play a role when hydrogen is fully (100%) humidified for the low temperatures cell test while in the present work only hydrogen on the count/reference electrode side was humidified to a water vapor partial pressure of 0.16 atm, corresponding to a relative humidity of 3 at 160°C.

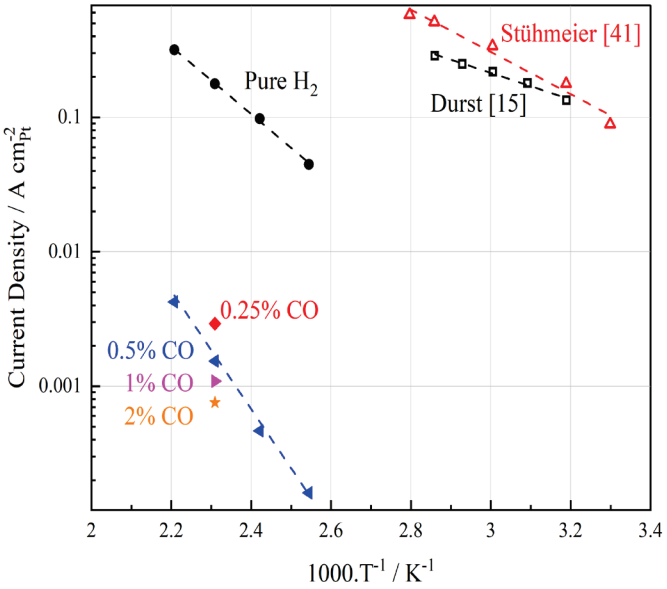

Figure 4. Arrhenius plots for HOR/HER exchange current densities in the absence and presence of carbon monoxide. Data were obtained in high temperature polymer electrolyte cells operating under the hydrogen pumping mode. Two sets of data from literature for pure hydrogen in the low temperature region are presented for comparison.

3.2 HOR/HER kinetics in the presence of CO

Figure 5a shows the HER/HOR polarization curves for pure hydrogen and hydrogen containing CO from 0.25 to 2.0 % at 160°C. For pure hydrogen the polarization curves is slightly asymmetric, with an increased limiting current density for HER. In the present work the mass transport effect has not been compensated, which may lead to additional polarizations at high current densities. For HER reactions, the shielding effect of the catalyst sites by the hydrogen evolution reactions have been considered for the asymmetric behavior of the HOR/HER polarization. This might be an issue in liquid electrolytes but, as pointed out by Durst et al. [20], probably not the case in polymer electrolytes. In the present work at temperatures of above 100°C, this can hardly be a major reason. The most likely explanation is the change of the electrode reaction mechanism i.e. a rate limitation imposed by the Tafel reaction.

As shown by Stühmeier et al. [41] increase in the partial pressure of hydrogen from 100 to 450 kPa leads to significant improvement of the HOR kinetics while the HER kinetics improves only slightly. As a result, the Tafel plots for HER/HOR become much more symmetrical. These observations are in good agreement with the assumption of a Tafel-limitation at high overpotentials. Increase in the hydrogen partial pressure improves the dissociative adsorption of hydrogen, i.e. the Tafel step (1).

Table 1. Summary of exchange currents densities and Tafel slopes as well as activation energy of the present study.

Temperature oC	Fuel (H_2/CO)	Exchange current density i^o (mA/cm^{2}Pt)	Tafel slope (mV/dec)		Activation energy E_a (kJ/mol)	Ref.
			b_{HOR}	b_{HER}		
120°C	100/0	44.6	70	65		
140°C	100/0	97.8	209	43		
160°C	100/0	177.4	186	46	49.6	
180°C	100/0	317.4	-	40		This work
160°C	99.75/0.25	2.9	1381	38		
160°C	99.5/0.5	1.5	340	42		
160°C	99.0/1.0	1.1	207	45	-	
160°C	98.0/2.0	0.76	233	44		
80°C	100 (Nafion)	200-600	-	-	-	[19]
80°C	100 (Nafion)	240	-	-	16	[15]
80°C	100 (Nafion)	520	-	-	20	[41]

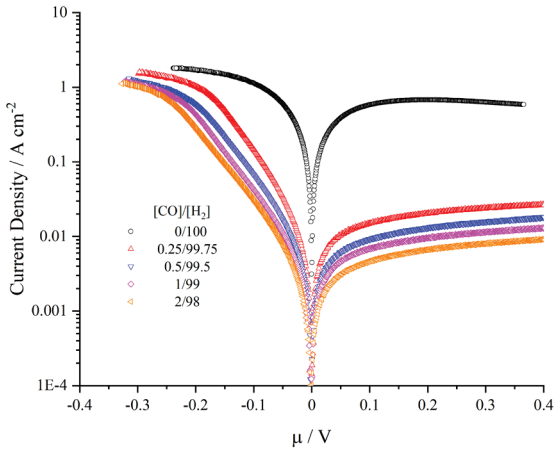

Fig. 5. I-V curves for HOR and HER at 160°C in the presence of CO. The CO/H_2 ratios are indicated in the figure where 0/100 was for pure hydrogen. The working electrode loading was of 6.5 μgPt cm^{-2}.

In the presence of CO, the strong adsorption of CO on the surface of Pt catalysts hinders the HOR kinetics due to the limitation of slow dissociative hydrogen adsorption (Tafel step), while the associative hydrogen desorption does not seem to limit the HER in the studied potential range.

The presence of CO in the hydrogen stream results in a significant decrease in the HOR current. At an overpotential of 0.1 V, the HOR kinetic current density was decreased from 600 mA/cm^2 for pure hydrogen to 2.9 mA/cm^2 at the CO concentration of 0.25%, and further down to 1.5, 1.1 and 0.76 mA/cm^2 for 0.5, 1.0 and 2.0%CO, respectively. In term of exchange current densities of HOR the presence of CO at a concentration of 0.25-2.0% results in a decrease of i^o by about 2 orders of magnitude, as seen from Figure 4.

4. Conclusions

The hydrogen oxidation and evolution reaction behavior on Pt/C electrodes was studied in phosphoric acid doped polybenzimidazole membrane electrolytes in a temperature region from 120 to 180 °C without and with the presence of carbon monoxide. The study was conducted in a hydrogen pumping cell mode using gas diffusion electrodes with a platinum loading of 1.5-6.5 μgPt/cm$^2_{Geo}$. By this method that mass transport contribution to the electrode polarization is minimized and the ohmic resistance was eliminated from electrochemical impedance measurements. Fitting of the polarization data into the Butler–Volmer equation obtains kinetic parameters including exchange current density, transfer coefficient and activation energies. The results show that the HOR, but not HER, rate is limited by the Tafel step. In the presence of CO the Tafel plots for HER/HOR become severely asymmetric. The strong adsorption of CO on the Pt surface hinders the HOR kinetics due to the limitation of slow dissociative hydrogen adsorption (the Tafel step), while the associative hydrogen desorption does not seem to limit the HER in the studied potential range. At CO concentrations of 0.25-2.0% at 160°C 2 orders of magnitude decrease in the HOR exchange current density.

Acknowledgement

This work was financially supported by Energy Technology Development and Demonstration (EUDP) Program (COBRA-Drive, 64018-0118), Denmark.

References

1. J. Durst, A. Siebel, C. Simon, F. Hasche, J. Herranz, and H. A. Gasteiger, Energy Environ. Sci., **7**, 2255 (2014).

2. H. A. Gasteiger, J. E. Panels, and S. G. Yan, *J. Power Sources*, **127**, 162 (2004).

3. S. Martin, J.O. Jensen, Q. Li, P.L. Garcia-Ybarra and J.L. Castillo, Inter. J. Hydrogen Energy, **44** (2019) 28273-28282

4. B. Conway and J. M. Bockris, J. Chem. Phys., **26**, 532 (1957)

5. J. M. Bockris and E. Potter, J. Chem. Phys., **20**, 614 (1952)

6. J. M. Bockris, J. McBreen, and L. Nanis, J. Electrochem. Soc., **112**, 1025 (1965).

7. W. Vogel, L. Lundquist, P. Ross, and P. Stonehart, Electrochim. Acta, **20**, 79 (1975).

8. N. M. Marković, B. N. Grgur, and P. N. Ross, J. Phys. Chem. B, **101**, 5405 (1997).

9. B. E. Conway and G. Jerkiewicz, Electrochim. Acta, **45**, 4075 (2000)

10. M. R. Gennero de Chialvo and A. C. Chialvo, Phys. Chem. Chem. Phys., **6**, 4009 (2004).

11. J. Greeley, T. F. Jaramillo, J. Bonde, I. Chorkendorff, and J. K. Nørskov, Nat. Mater., **5**, 909 (2006).

12. E. Skúlason, V. Tripkovic, M. E. Björketun, S. Gudmundsdóttir, G. Karlberg, J. Rossmeisl, T. Bligaard, H. Jónsson, and J. K. Nørskov, J. Phys. Chem. C, **114**, 18182 (2010).

13. J. A. Santana, J. J. Saavedra-Arias, and Y. Ishikawa, Electrocatalysis, **6**, 534 (2015).

14. W. Sheng, H. A. Gasteiger, and Y. Shao-Horn, J. Electrochem. Soc., **157**, B1529 (2010).

15. J. Durst, C. Simon, F. Hasché, and H. A. Gasteiger, J. Electrochem. Soc., **162**, F190 (2015).

16. W. Sheng, Z. Zhuang, M. Gao, J. Zheng, J. G. Chen, and Y. Yan, Nat. Commun., **6**, 5848 (2015).

17. H.A. Gasteiger, J.E. Panels, S.G. Yan, J. Power Sources 127 (2004) 162

18. C.J. Song, Y.H. Tang, J.L. Zhang, J.J. Zhang, H.J. Wang, J. Shen, S. McDermid, J. Li, P. Kozak, Electrochim. Acta **52** 2552, (2007)

19. K.C. Neyerlin, W.B. Gu, J. Jorne, H.A. Gasteiger, J. Electrochem. Soc. **154,** B631, (2007).

20. Durst, J., Simon, C., Hasché, F., & Gasteiger, H. A. J. Electrochem. Soc. **162**, F190–F203 (2015).

21. T. Reier, M. Oezaslan and P. Strasser, ACS Catal., **2**, 1765–1772 (2012).

22. C. M. Zalitis, D. Kramer, and A. R. Kucernak, Phys. Chem. Chem. Phys., **15**, 4329 (2013).

23. M. Wesselmark, B. Wickman, C. Lagergren and G. Lindbergh, Electrochem. Commun. **12**, 1585-1588 (2010)

24. X. Wang, R. Ahluwalia and A. Steinbach, J. Electrochem. Soc., 160, F251–F261 (2013).

25. V.F. Valdés-López, T. Mason, P.R. Shearing and D.L. Brett, Progress in Energy and Combustion Science **79,** 100842 (2020)

26. H.A. Gasteiger, N.M.Markovic, P.N. Ross, J Phys Chem **99**, 16757–67 (1995).

27. D. Aili et al. D. Aili, D. Henkensmeier, S. Martin, B. Singh, Y. Hu, J. O. Jensen, L. N. Cleemann and Q. Li, Electrochemical Energy Reviews **3**, 793–845 (2020).

28. Li QF, He RH, Gao JA, Jensen JO, Bjerrum NJ. The CO poisoning effect in PEMFCs operational at temperatures up to 200°C. J Electrochem Soc **150**, A1599-1605 (2003).

29. H. A. Hjuler, K. Azizi, N. Seselj, S. Martinez Alfaro, H. R. Garcia, D. Gromadskyi, L. Hromadska, S. Primdahl, J. O. Jensen, Q. Li, S. Celenk and L. Cleemann, ECS Trans **104**, 403–413 (2021).

30. P. Krishnan, J. Park, C. Kim, J. Power Sources **159**, 817–823 (2006).

31. M. Boaventura, H. Sander, K.A. Friedrich et al. Electrochim. Acta **56**, 9467–9475 (2011).

32. C.Z. Zhang, W.J. Zhou, M.M. Ehteshami et al. Energy Convers. Manag. **105**, 433–441 (2015).

33. C.Y. Chen, K.P. Huang, J. Appl. Electrochem. **48**, 911–921 (2018)

34. Y. Devrim, A. Albostan, H. Devrim, Int. J. Hydrog. Energy **43**, 18672–18681 (2018).

35. C.Y. Chen, W.H. Lai, Y.K. Chen et al. Int. J. Hydrog. Energy **39**, 13757–13762 (2014)

36. F.J. Pinar, M. Rastedt, N. Pilinski, et al. Int. J. Hydrog. Energy **42**, 13860–13875 (2017).

37. F. Zhou, S.J. Andreasen, S.K. Kær, et al. Int. J. Hydrogen Energy **40**, 14932–14941 (2015).

38. S. Martin, P.L. Garcia-Ybarra, J.L. Castillo, Electrochem. Commun. **93**, 57–61 (2018).

39. S. Martin, Q. Li, T. Steenberg, et al. J. Power Sources **272**, 559–566 (2014).

40. T. Engl, K.E. Waltar, L. Gubler, et al. J. Electrochem. Soc. **161**, F500–F505 (2014).

41. B. M. Stühmeier, M. R. Pietsch, J. N. Schwämmlein and H. A. Gasteiger, J. Electrochem. Soc., **168** 064516 (2021)

MANUSCRIPT 3

Potential Cycling Test of High Temperature PEMFC Based on Acid Doped Polybenzimidazole Membranes

Sanser Celenk, Lars N. Cleemann, Jens Oluf Jensen and Qingfeng Li

Received 00th January 20xx,
Accepted 00th January 20xx

DOI: 10.1039/x0xx00000x

Potential Cycling Test of High Temperature PEMFC Based on Acid Doped Polybenzimidazole Membranes

Sanser Celenk,[a] Lars N. Cleemann,[b] Jens Oluf Jensen,[a] and Qingfeng Li*,[a]

Abstract

The performance degradation of HT-PEMFC is studied by potential cycling at 160°C. The membrane-electrode-assemblies are made of acid-doped polybenzimidazole membranes and $PtCo_x$ catalysts on the cathode. While the upper potential limit is fixed at 0.95 V the degradation is stressed by varying the low-end potential from 0.8 to 0.65 V and hold duration from 5 to 60 sec. During the cycling tests, little degradation of the membrane, in terms of ohmic resistance and open circuit voltage is observed but a significant performance loss is attributable to the mass transport due to the degradation of the electrode hydrophobicity. A major catalyst degradation mechanism is the platinum particle growth via the electrochemical Ostwald ripening. No evidence of the cathode dealloying was detected during the potential cycling. The dissolution of platinum or the surface oxides of platinum during the upper potential hold at 0.95 V seems limited by the available acid in the electrolyte membrane. The low-end potential and the hold duration seem critical where the reduction and re-deposition of platinum occur, leading to formation of larger particles and hence loss of the active surface area.

1. Introduction

Hydrogen and fuel cells have reached a maturity to provide practical power for automobiles and stationary as well as portable applications. Polyme electrolyte membrane fuel cells (PEMFC) are a major type for automobile applications.[1] The technology based on perfluorosulfonic acid (PFSA) type membranes e.g., Nafion® is often referred to as the low temperature PEMFC (LT-PEMFC) as it is limited to operation at temperatures up to around 80 °C. Challenges due to the low operating temperatures include system complexities for water and thermal management as well as establishment of a hydrogen infrastructure because of high sensitivty of the catalysts toward fuel impurities.[2]

Phosphoric acid (PA) doped polybenzimidazole (e.g. poly-(2,2´-(*m*-phenylene)-5,5´-bibenzimidazole or PBI) membranes are an alternative materials to achieve high temperature e.g. 150-160 °C operation.[3] PBI is a class of thermally resistant heterocyclic thermoplastics [4] while PA is the dopant with combined intrinsic proton conductivity, thermal stability and low volatility.[5] The HT-PEMFC technolgy can tolerate up to 3 % CO [6] and hence enable utilization of hydrogen-rich fuels from e.g. methanol erforming. Other operating features include little humidification and easy cooling.

The durability has been recognized as the most critical issue to be addressed before widespread commercialization of the technology. Major mechanisms of degradation if fuel compoents include the loss of doping phosphoric acid, polymer oxidation and membrane thinning and platinum nanoparticle growth and hence active surface area decrease, as recently reviewed.[7]

The acid loss is, to a great extent, mobile through the membrane drived by capillary force and electrochemical migration [8,9]. The acid loss is primarily via the evaporation mechanism and therefore impacted by operating temperatures, gas stoichiometries and current densities.[10] Under a steady state operation at a current density of 0.2 A/cm^2, the rate of acid loss is about 3-5 µg m^{-2} s^{-1} or 1-2 µg cm^{-2} h^{-1}. [11] Based on this rate, the acid inventory of MEAs was estimated to be sufficient for a lifetime over 20,000 hours. Polymer oxidation and the resulted membrane thinning are an issue also for the long-term applications. Using modified polymers by crosslinking or thermal curing, operation over 10,000 hours has been achieved by several groups. [11-14]

Catalyst degradation, on the other hand, is due to the steady loss of the active surface area by physical and electrochemical Ostwald ripening of platinum nanocatalyst particles.[15] The

a. Department of Energy Storage and Conversion, Technical University of Denmark, Fysikvej B310, 2800 Lyngby, Denmark.
b. Blue World Technologies, Egeskovvej 6C, 3490 Kvistgård, Denmark.

** Correspondance: kaz@blue.world; qfli@dtu.dk*

electrochemical dissolution of Pt in acidic electrolytes can be a direct dissolution of the metal:

$$Pt \rightleftarrows Pt^{2+} + 2e^- \quad E(V) = 1.19\ V + 0.029\ V \cdot \log[Pt^{2+}] \qquad (1)$$

or via formation of the surface oxide [16]

$$Pt + H_2O \rightleftarrows PtO + 2H^+ + 2e^- \quad E(V) = 0.98\ V - 0.59\ V \cdot pH \qquad (2)$$

$$PtO + H_2O \rightleftarrows PtO_2 + 2H^+ + 2e^- \quad E(V) = 1.05\ V - 0.59V \cdot pH \qquad (3)$$

Followed by chemical or electrochemical dissolution:

$$PtO + 2H^+ \rightleftarrows Pt^{2+} + H_2O \quad \log[Pt^{2+}] = -7.06 - 2pH \qquad (4)$$

$$PtO_2 + 4H^+ + 2e^- \rightleftarrows Pt^{2+} + H_2O$$

$$E(V) = 0.834\ V - 0.118\ V \cdot pH - 0.029V \cdot \log[Pt^{2+}] \qquad (5)$$

The solubility of Pt changes with a number of factors such as the electrode potential, type and pH of electrolytes, and temperature. The dissolved Pt ions may be reduced hydrogen permeated from the anode [17] resulting in the formation of the so called Pt band.[18]

In concentrated phosphoric acid at elevated temperatures, a strong dependence of the platinum surface area loss on the electrode potential, especially above 0.70 V, was observed,[19] likely via combined mechanism of agglomeration/sintering and Ostwald ripening[20]. It has been reported that the Pt solubility increased by three orders of magnitude as the electrode potential is lifted from 0.8 to 1.0 V vs RHE [21] while the Pt dissolution rate increased by 9 orders of magnitude when the potential was swept from 0.6 to 1.0 V vs. RHE.[22] For PBI cells, the PA content in the membrane is limited. Using the PA inventory numbers of 20-40 mgcm^{-2} it is estimated that the dissolution of the platinum catalyst under OCV can be up to 2-5% of the total catalysts with the loading of 0.5-1.0 mg$_{Pt}$ cm^{-2} in a cathode.[23] This number may have significant impacts on the catalyst degradation particularly under the potential cycling mode.

It is well known that the carbon support of catalysts is susceptible to corrosion at potentials above 0.207 V: [24]

$$C + 2H_2O \rightleftarrows CO_2 + 4H^+ + 4e^- \quad E^0 = 0.207\ V\ vs\ RHE \qquad (6)$$

leading to detachment and triggering further agglomeration of Pt particles. A side effect of carbon corrosion is the formation of surface oxides, causing a decrease in hydrophobicity of the catalyst layer and possibly PA flooding. Any operation modes involving exposure of electrodes to high potentials near the OCV will cause significant carbon corrosion. A critical issue is the start-stop of a fuel cell, during which the transition of the H_2/air to an air/air mode generates a reverse current resulting in electrode potentials higher than the OCV [25,26] and instigate rapid carbon corrosion and catalyst degradation. Operation under dynamic modes i.e. with load or start-stop cycling involves exposure of the cathode to high potentials. Similar phenomena can be observed during the fuel starvation of a fuel cell. Figure 1 illustrates the potential profile of anode and cathode during the cell start, stop, idle and fuel starvation.

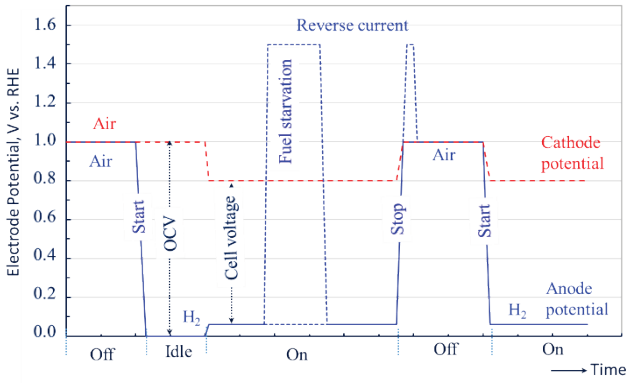

Figure 1. Representation of the anode and cathode potential changes during the cell start, stop, idle as well as fuel starvation.

Load cycling studies in lietrature can be divided into low load (0-0.4 A cm^{-2}) and high load (0.4-1.0 A cm^{-2}) levels. The high load cycling involves cell operation in the low voltage range, without exposure of the cell to OCV.[27] The main mechanism for the performance degradation under this mode is the PA loss, which eventually results in membrane degradation e.g., decreased proton conductivity. The membrane degradation, as characterized by the hydrogen crossover or OCV observation, is, however, not always detectable during the short timeframe of the load cycling test.

The low load cycling, on the other hand, involves high cell voltages. The major degradation mechanism is the catalyst or electrode degradation. At zero current, i.e. during idling of a fuel cell, the cell is exposed to OCV, where severe carbon corrosion and platinum nanoparticle aggregation occur.[28,29] Platinum catalyst dissolution, more precisely, the formation and dissolution of the metal surface oxide, is intensified during the low load cycling.

The OCV hold is the most destructive stressor of the operating conditions. An exposure of a fuel cell to OCV was reported to exhibit a voltage degradation of over 400 μV h^{-1}, showing significant increases in both the activation and mass transport resistance as well as a reduction of the cathode elctrochemically active surface area (ECSA).[30,31] Compared to the fresh electrode, a significant increase of the Pt nanoparticle size of the cathode after OCV exposure was reported.[30, 32] To avoid exposure to OCV (0 A cm^{-2}) some potential cycling studies were conducted to apply a small current density e.g., 0.04 A cm^{-2} [33] or 0.05 A cm^{-2} [34] where the exact cell voltage at the high end is unknown.

The present work is devoted to a study of the low load cycling, with well controlled yet systematically tailored voltage range. It is noted that for the low load or high potential cycling at near OCV, there is little water formation inside the fuel cell. For prolonged tests, the effect of atmospheric humidity on the PA dehydration should be taken into account.

2. Experimental

2.1. MEA, cell assembling and test rig

The MEAs tested in this study were state-of-the-art commercial products supplied by Blue World Technologies. Although the exact properties of the MEAs were not disclosed by the supplier, it is noteworthy that the cathode catalyst layer was composed of PtCo/C (Tanaka) and the anode was made of Pt/C. The MEAs had an active area of 21 cm^2 and were hot-pressed beforehand.

The single cell was formed using custom-made graphite flow plates with a 5 cm x 5 cm serpentine flow field, gold coated copper current collectors and aluminum end plates. To prevent over-compression of the MEAs, 150 µm PTFE gaskets were used on both sides. The cell was assembled using 12 pieces of M-8 steel bolts. The bolts were gradually tensioned by applying torque in seven steps, with a final applied torque of 1.2 Nm.

The temperature of the cells was controlled using resistive steel rods mounted in the Al endplates, and the temperature was monitored with K-type thermocouples. The temperature was regulated using CAL3300 controllers. The cells were gradually heated to 160 °C at a rate of 5 °C per minute after cell assembly. Once the temperature reached 160 °C, the cell was fed with H_2 and air, and the MEAs were subjected to a galvanostatic break-in.

The MEAs were tested using an in-house built multi-channel experimental rig. Laboratory made resistive electronic loads were used to control either current or the cell voltage. The flow rate of gases was regulated using Brooks GF40 thermal mass flow controllers. Since the mass flow controllers were calibrated for N_2 by the manufacturer, further calibration was done for H_2 with a digital calibration device (MesaLabs DryCal Definer 220 Primary Flow Calibrator). A customized Labview application was utilized for monitoring and controlling the cells. Furthermore, the test rig was equipped with a digital oscilloscope (ROHDE&SCHWARZ RTB2004), a digital multi-meter (Keithley 2700 Integra) and a four-probe shunt resistor (PCN RXM50) to ensure the controlled voltage or current.

2.2. Break-in

The MEAs were activated prior to the potential cycling by applying a constant current density of 0.4 A cm^{-2} with a stoichiometry of 1.5 for H_2 and 2.5 for air, while maintaining a temperature of 160 °C for a specific duration. Some MEAs underwent preliminary short break-in tests for up to 48 hours, while others underwent a break-in period of 300 hours. After the break-in period, the BOL performance was evaluated by recording a polarization curve.

2.3. Polarization curves

The I-V curves were obtained through stepwise reduction of the current, starting from 0.9 A cm^{-2} and decreasing to open circuit voltage with a stabilization period of 2 minutes for each step. Stoichiometry of the gases were kept constant at 1.5 for H_2 and 2.5 for air until 200 mA cm^{-2}. For current densities less than 200 mA cm^{-2}, constant flow rates of 45 NmL min^{-1} for H_2 and 180 NmL min^{-1} for air were supplied to the anode and cathode respectively.

2.4. Potential cycling

Figure 2 shows the cell voltage profile i.e. square waves applied to the corresponding MEAs during potential cycling tests. These tests were conducted while maintaining a constant temperature of 160 °C, flow rate of gases, and an upper potential value of 0.95 V. MEAs M08-05, M07-05, and M65-05 were subjected to an investigated lower potential value of 0.8 V, 0.7 V, and 0.65 V, respectively. The cycling for these MEAs was conducted with a 5-seconds upper potential and a 5-seconds lower potential. The effect of cycling duration was studied with MEAs M07-30 and M07-60, where the lower potential limit was set to 0.7 V. The duration at potential limits was varied from 30 seconds to 1 minute.

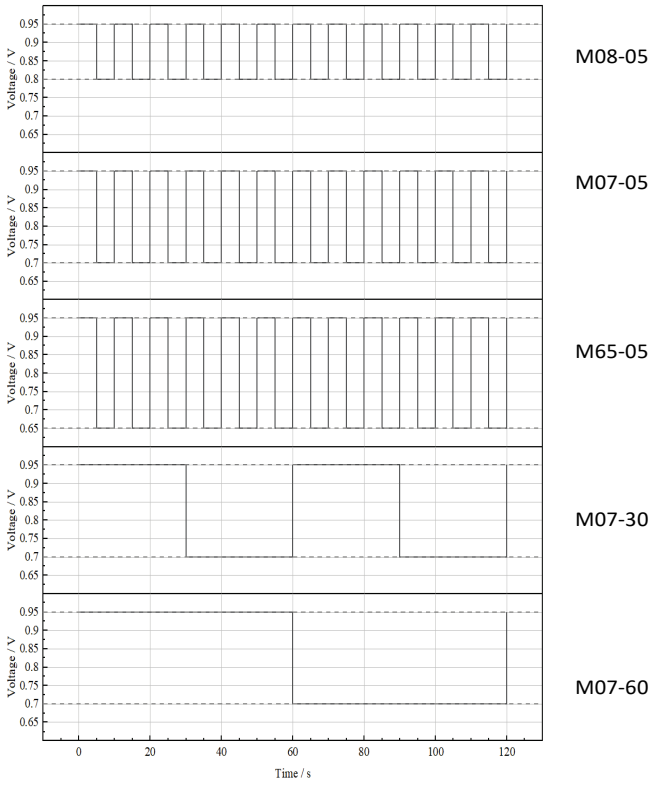

Figure 2 Voltage profiles for the potential cycling test with MEAs named to the right.

MEAs M08-05, M07-05, and M65-05 underwent a total of 30,000 potential cycles, divided into four parts at 5,000, 10,000, 20,000, and 30,000 cycles, while MEA M07-30 underwent a total of 10,000 potential cycles, split into

two parts at 5,000 and 10,000 cycles. MEA M07-60, on the other hand, underwent only one part consisting of 5,000 cycles. After each part, the MEAs were relaxed at 0.4 A cm^{-2} for an hour before recording a polarization curve. This procedure resulted in a total of 5 polarization curves for M08-05, M07-05, and M65-05, 3 polarization curves for M07-30, and 2 polarization curves for M07-60, including the BOL polarization curves. Moreover, the electrochemical impedance spectroscopy was performed on the MEAs after the each polarization curve.

2.5. Electrochemical impedance spectroscopy

A Princeton VersaSTAT 3 potentiostat was utilized to perform the Electrochemical impedance spectroscopy (EIS), coupled with the electronic load to enable impedance measurement at high currents. Potentiostatic impedance measurement was carried out while the cell was operating at 400 mA cm^{-2}. Although the full spectra was captured, we only used the high frequency resistance (HFR) to estimate and track the membrane resistance during cycling.

2.6. SEM and XRD

Scanning electron microscopy (SEM) imaging was carried out using a Zeiss EVO MA10 scanning electron microscope equipped with an Oxford X-Max 80 mm2 INCA EDS system. MEA cross sections for SEM imaging were prepared by cutting with a scalpel followed by mounting onto a sample holder and subsequent ion milling using a Hitachi E-3500.

X-ray powder diffraction patterns of the cycled PtCo/C cathode catalyst were collected on a Rigaku Smartlab X-ray diffractometer (Cu-Ka radiation (45 kV 200 mA) with a step size using transmission geometry (focusing optics). Catalyst samples were collected by scraping off material from the polymer electrode interface onto a piece of tape.

3. Results and Discussion

3.1. Break-in test under potential cycling

HT-PEMFCs need an activation time at the beginning of operation, during which a stable cell performance is reached to ensure the reproducibility and comparability of the cell performance [35]. The main mechanism is associated with the phosphoric acid distribution. The acid originates from the acid doping polymer membranes and is driven into the catalyst layers of the electrodes [36, 37] by the capillary forces, which is dependent on the microporous structure of the carbon support, the hydrophobicity of the catalytic layer. Another mechanism is the parasitic movement of phosphoric acid through the vehicular mechanism of conductivity. As reported by Becker et al. [38] the acid anion ($H_2PO_4^-$) has a transference number of ca. 4% in PBI cells. This, in combination with the back acid diffusion coefficient of 10^{-10} m^2 s^{-1}, determines the redistribution of the acid during the break-in process. Under a constant current density of 0.2 A/cm^2 this process takes at least 300 hours, as shown in Figure 3.

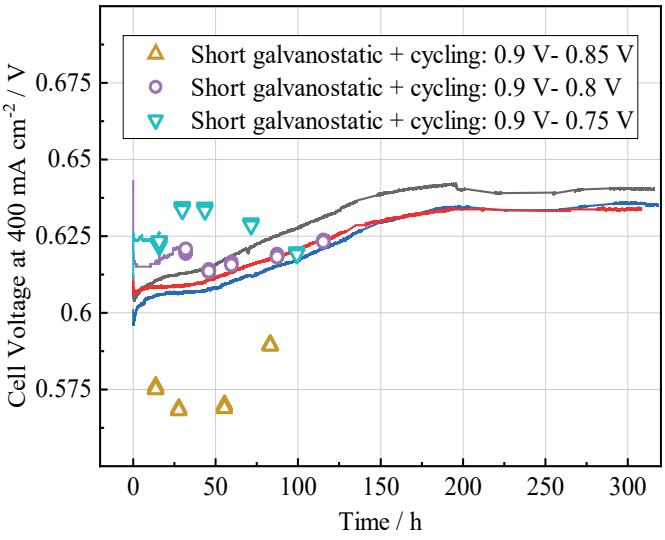

Figure 3 Cell voltage change during the break-in period at 160 °C with hydrogen and air of stoichiometries of 0.12 and 2.0, respectively. Black and red curves: under constant current (0.2 A/cm^2). Open circles: from I-V curves after potential cycling between 0.9 V (5s) and 0.8 V (5s) for 5,000, 100,000 cycles.

Preliminary tests were carried out by a short activation time of 16-48 hours, followed by potential cycling between 0.9 and 0.8 V with step time of 5 sec each. It is seen that, after a small decrease, the cell voltage was kept increasing during the period with potential cycling. It is seen that the potential cycling does not seem promoting the break-in process. In fact cycling seemed resulting in less acid redistribution due to the smaller current compared to a standard break-in procedure at a constant current density of 0.2 A/cm^2. In the following test, a full break-in was achieved for a period of 300 hours at 0.2 A/cm^2 before the potential cycling started.

3.2. Analysis of I-V curves and iR correction

The typical performance of the MEAs at the beginning of life (BoL) is shown in Figure 3a, showing a good reproducibility within a voltage range of 0.7 ± 0.002 V at 0.2 A/cm^2 and 0.53 ± 0.003 V at 0.8 A/cm^2, respectively.

The following equation is often used to fit experimentally obtained polarization curves for fuel cells:

$$E_{Cell} = E_{rev} - h_{ORR} - iR - h_{mt} \quad (7)$$

Here E_{rev} is the reversible cell voltage, R is the total ohmic resistance, η_{ORR} the cathode activation loss and η_{mt} the mass transport loss.

The reversible cell voltage is a function of temperature and pressures of hydrogen and oxygen and can be expressed as

$$E_{rev} = 1.23 - 9 \cdot 10^{-4}(T - 298) + \frac{2.303\,RT}{4F} \times \log\left[P_{H_2}^2 P_{O_2}\right] \quad (8)$$

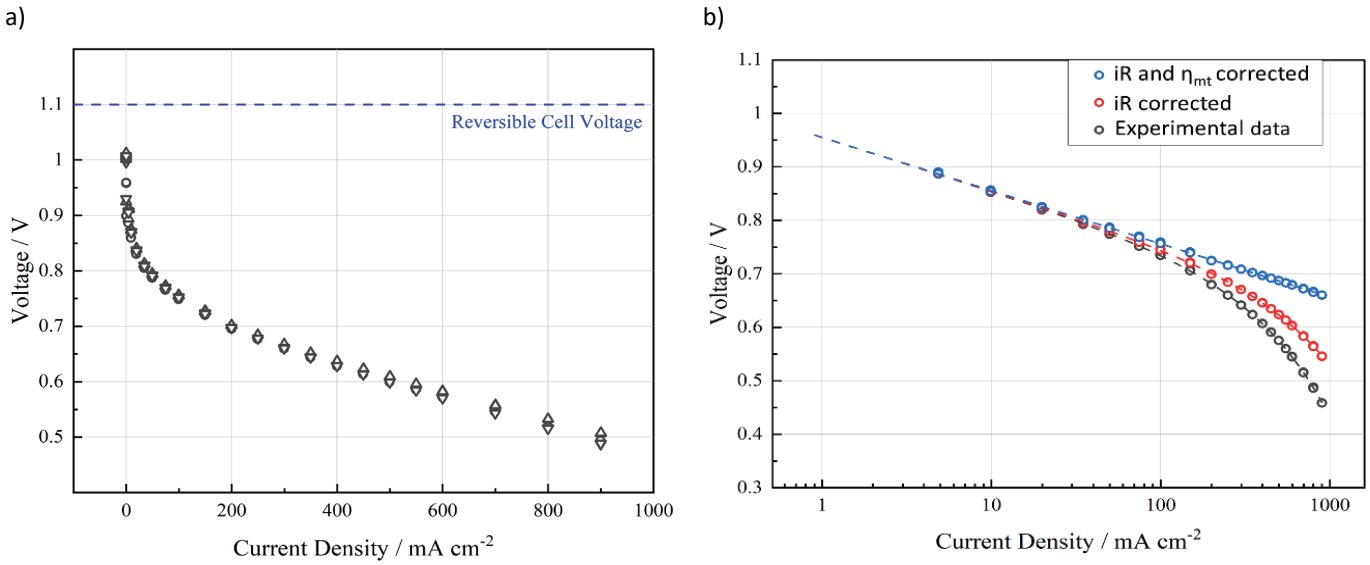

Figure 4. a) Polarization curves of typical BoL performances at 160 °C operating with dry hydrogen and air under ambient pressure and stoichiometries of λ_{H2} = 1.5 and λ_{Air} = 2.0, respectively. b) Tafel plot of as measured, iR- as well as iR & η_{mt} corrected data.

where $P^*_{H_2} = P^*_{O_2}$ = 1 bar are the reference pressure of hydrogen and oxygen. In HT-PEMFC no humidification is applied for either hydrogen or air. At the anode side P_{H_2} = 1 bar is assumed by neglecting any water diffused from the cathode chamber. At an air stoichiometry of λ_{Air} = 2.0, the water generation in the cathode chamber corresponds to a water vapor pressure of ca. 0.19 bar, which gives an oxygen partial pressure of ca. 0.17 bar. Based on these numbers and using equation (8) the reversible cell voltage of an HT-PEMFC at 160 °C is estimated to be E_{rev} = 1.1 V, as indicated in Figure 3a.

The cathode overpotential can expressed by the Tafel equation:

$$h_{ORR} = b \log\left(i/i_0\right) = a + b\log(i) \quad (9)$$

where *b* is the Tafel slope and i^0 the exchange current density. The concentration or mass transport overpotential is often written as

$$h_{mt} = c \log(1 - i/i_L) \quad (10)$$

where i_L is the limiting current density. As seen from Figure 3a the measured I-V curves are in the linear region, which indicates that the mass transport overpotential, if any, has a ohmic behaviour. In the following fit it is assumed that the mass transport overpotential is included in the Ohmic term and the following simple equation is used:

$$E_{Cell} = E_{rev} - h_{ORR} - i \cdot \text{å}R \quad (11)$$

Figure 3b shows the fitting results for MEA M07-05. Based on the high frequency resistance (HFR) from electrochemical impedance spectroscopic (EIS) measurements the iR-corrected I-V curve still shows deviation from the Tafel linearity at current densities above, say, 50 mA/cm^2. A significant contribution of the mass transport loss, though appearing ohmic, is obtained from the fitting. The mass transport loss is sensitive to the limiting current density, which is always poorly defined compared to the kinetic (logarithmic) and ohmic terms. It is therefore often practically determined by subtraction of the ohmic (HFR) and kinetic losses from the as measured i-V curves. As seen from Figure 4b, the contribution of the mass transport term is of the value as the ohmic loss in the low to intermediate current range and becomes significantly larger at higher current densities.

Some of the experimental and fitting results are summarized in Table 1. First of all MEAs exhibit high BoL OCVs and after 30 k cycles no changes in the OCV were observed, indicating little membrane degradation has occurred. The ohmic loss term in the table was estimated from the HFR, which, in fact, has changed to a very limited extent (3-5%) during the cycling test, confirming the observed little membrane degradation. It should be noted that, during the potential cycling, the cell suffered from the membrane drying due to the fact that the very low operating current densities led to little water formation. It is therefore that, after a certain period the potential cycling was stopped at cycle numbers of 5, 10, 20 and 30 k, after which the cell was operating at a constant load (400 mA/cm^2) for an hour in order to restore the membrane performance. All the EIS measurements were conducted after the membrane wetting restoration.

Also in the Table lists the mass transport loss from fitting. During the cycling period, a significant increase in the mass transport loss was observed at the EoL. Apparently the potential cycling has resulted in significant carbon corrosion

or/and degradation in the electrode hydrophobicity, as to be discussed below.

The cell performance in term of kinetic loss, i.e. the cell voltage after both iR and mass transport correction, is listed in the last column of the table. In the following discussion of the catalyst degradation, cell voltage data after the ohmic and mass transport correction are used.

Table 1 Summary of the potential cycling tests

MEAs	Cycling mode E(V)/Time (s)	OCV (V) BoL/EoL*	Ohmic loss (HFR, mOhm cm^2) Bol/EoL*	Fitting mass transport loss (mOhm cm^2) Bol/EoL*	Cell performance** E(V) @ (0.2 A/cm^2) Bol/EoL*
M08-05	0,95/5 + 0.8/5	1.01/1.020	96.2/98.9	108.8/241	0.738/721
M07-05	0,95/5 + 0.7/5	0.96/0.94	101.4/106.2	105.6/160.8	0.736/714
M65-05	0,95/5 + 0.65/5	1.01/1.03	98.1/102.1	83.9/125.9	0.738/708
M07-30	0,95/30 + 0.7/30	0.99/0.97	106.3/-	-/-	0.696/0.67
M07-60	0,95/60 + 0.7/60	1.03/1.01	99 /-	-/-	0.694/0.629

* BoL is defined as the time when break-in was completed while the EoL was after 30 k cycles.

** The cell performance was based on data after the iR and mass transport correction

3.3. Degradation in varied potential cycling range

Three MEAs were studied by varying the potential range of cycling from 0.9-0.8 V (M08-05), 0.9-0.7 V (M07-05) and 0.9-0.65 V (M65-05) at a fixing time frame of 5 s up and 65 s down. The cycling was stopped at 5, 10, 20 and 30 K cycles and I-V curves were recorded. After the iR and mass transport correction, the polarization curves at the Bol and Eol (30 K cycles) are shown in Figure 5a. A steady decrease in the cell performance was observed and the decrease was in the order of low end potentials from 0.8 to 0.65 V. Specific cell voltages at current densities of 0.2 and 0.6 A/cm^2 were collected and plotted as a function of the cycling numbers, as shown in Figure 5b. In the figure the points at cycle number of zero are the performance at the Bol. The steady decrease in the cell voltage was better seen. During the first 5 K cycle the cell voltage decrease at 0.2 A/cm^2 was observed of 12 mV for M08-05, 14 mV for M07-05 and 38 mV for M65-05, which were increased to 17, 24 and 29 mV at the end of 30 K cycles, respectively. These results will be discussed in the next section.

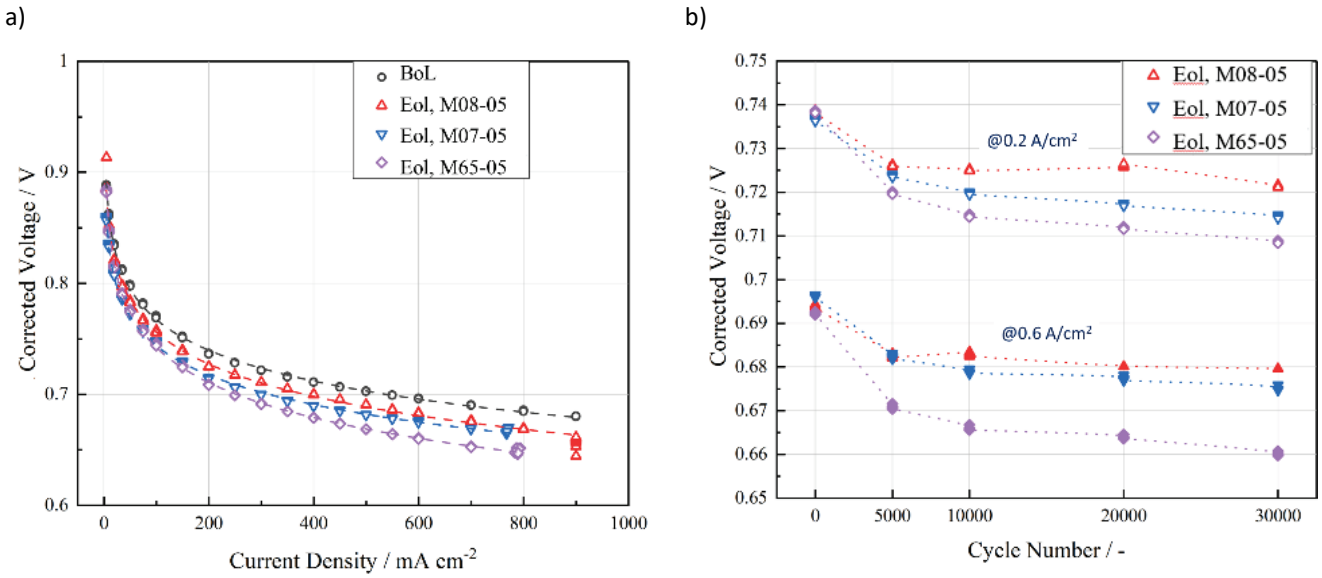

Figure 5. Polarization curves (a) and cell voltage at 0.2 and 0.6 A/cm^2 (b) after the ohmic and mass transport correction for three cycling range of the potential as indicated in the figure.

3.4. Degradation in varied potential hold

Another test was made by fixing the potential scan range from 0.9 to 0.7 V but varying the hold during at each potential, from 5/5 (M07-05) to 30/30 (Mo7-30) to 60/60 (M07-60) sec. The

ohmic and mass transport corrected cell voltages of the three MEAs are expressed in relation to their BoI performance and plotted against the cycle number and total operation time in Figure 6.

Of the three MEAs M07-05 has been subjected to 30 K cycles while M07-30 to 10 K cycles and M07-60 to 5 K cycles. In term of the total time, M07-05 has been subjected to an operation for 80 hours while M07-30 and Mo7-60 for 160 hours.

As seen from Figure 6a, in term of cycle numbers, the extended duration at each potential hold step led to increased performance degradation, i.e. in the order M07-60, M07-30 and M07-05. It is also seen that a sharp decrease in the cell performance (ca. 2%) in the first 5 K cycles, followed by a flat plot, particularly for M07-05.

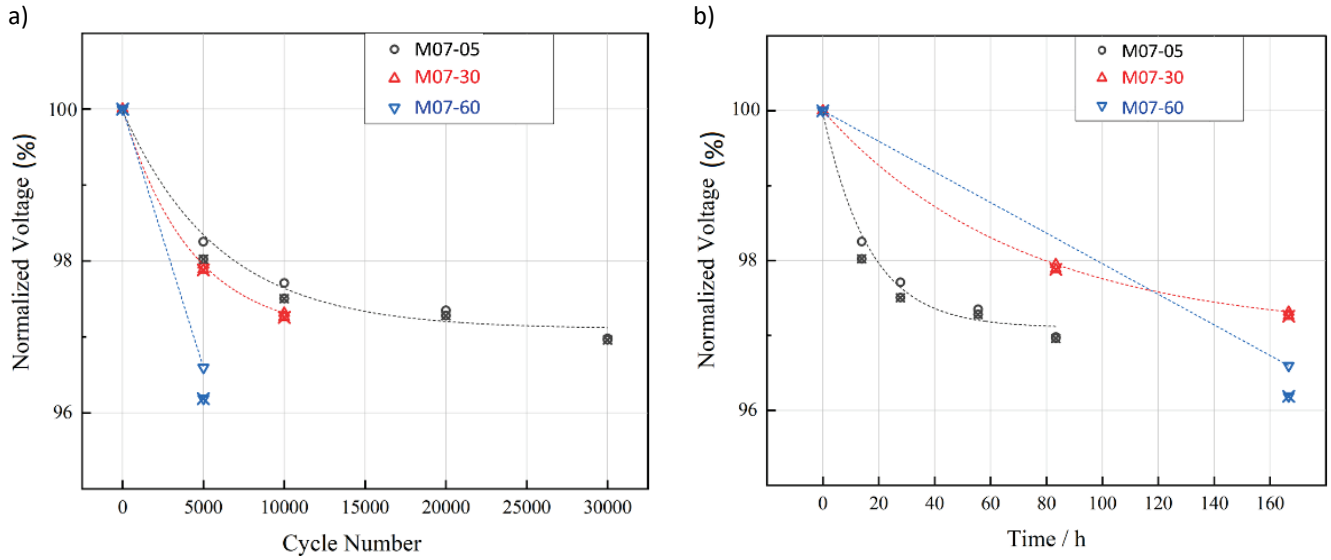

Figure 6. Normolized cell voltage relative to the BoL performance as a function of cycle number (a) and of operation time (b) at current density of xxx A/cm$^{2.}$ The voltage was corrected after the ohmic and mass transport losses. The three MEAs were subjected to potential cycling between 0.9 and 0.7 V for hold duration of 5/5 (Mo7-05), 30/30 (M07-30) and 60/60 (M07-60) sec.

In term of the operation time (Figure 6b), a severe degradation was observed for M07-05 in the first 15-30 hours, which was followed by slow degradation afterwards. For M07-30 to M07-60, the slower degradation rate was observed.

3.5. Catalyst degradation mechanisms

The cycling studies of the present work has a fixed high potential end hold at 0.9 V. At this potential, carbon corrosion and platinum oxidation would occur in a similar way for the five MEAs. Carbon corrosion in concentrated phosphoric acid has been a subject of studies in connection to phosphoric acid fuel cells [39]. The work by Oh et al. [40] focused on PBI cells, showing limited carbon corrosion at cell potentials below 1.1 V for short terms. Long-term durability test for up to 18,000 hr at 150°C and 0.2 A/cm^2, on the other hand, has observed significant thinning of the catalyst layer [41]. The SEM images of cross sections of fresh and three MEAs after 30 K cycles (Figure 7) show no visible thinning of the catalyst layers. On the other hand, a significant increase in the mass transport loss was observed for all the testing cells, which was therefore attributed to the degradation of the hydrophobicity of the catalyst layers.

At potentials close to OCV, an oxide layer will be formed on the Pt surface, which undergoes dissolution into the electrolytes. A close dependency of the metal dissolution, including the solubility and dissolution rate, was found on the electrode potential, particularly in the high potential range. By increasing the potential from 0.8 to 0.95 V vs. RHE, the solubility of Pt was found to increase by ~ 500 times, from1.5 × 10^{-7} to 7.5 × 10^{-5} mol L^{-1} in 96% PA at 176 °C [42]. The dissolution rate of Pt in concentrated PA at 160 °C was further estimated to increase by nine orders of magnitude if the potential was swept from 0.6 to 1.0 V.[43]

Phosphoric acid is present in the MEAs, the amount of which can be estimated from the membrane doping level (ca. 10 mol H_3PO_4 per mole polymer repeat unit) and found to be about 20 mg H_3PO_4/cm^2.[44] It is estimated that the high potential hold at 0.9 V leads to the dissolution of ca. 2-5% of platinum catalysts, which is limited by the Pt solubility in the acid.

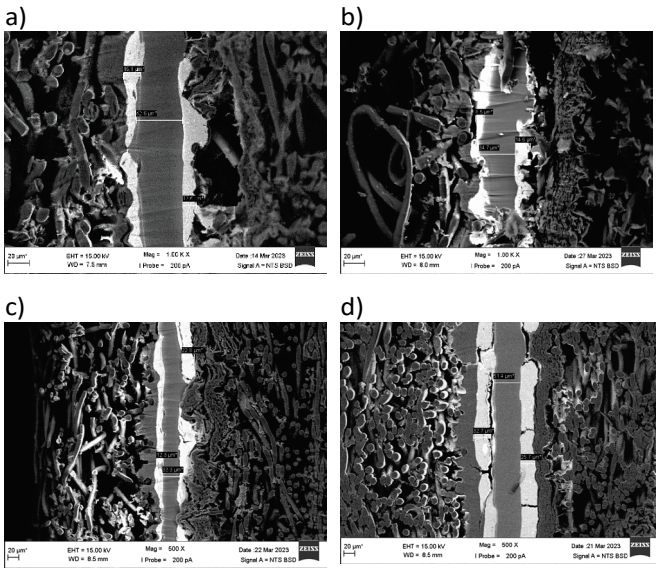

Figure 7. SEM images of cross sections of a) fresh MEA and b) M08-05, c) M07-05 and d) M65-05 at the EoL after 30 K cycles.

The difference is made from the low potential (0.8, 0.7 and 0.65 V) end hold where the reduction and deposition of platinum occurs. During the cycling, the growth of large Pt particles occur at the expense of smaller ones, which are progressively dissolved. Physically the surface energy of the platinum particles is proportional to the inverse of their size, small particles are more prone to dissolution while platinum ion deposition preferably occurs at the larger particles. As the process involves electron and ion transport, it is hence called the electrochemical Ostwald ripening mechanism.[45] The reduction and deposition of the dissolved Pt are enhanced in the low potential region below 0.7 V, which will stimulate the particle growth.

It seems that, in PBI cells where only limited phosphoric acid is present in the membrane compared to phosphoric acid fuel cells, the longer hold time at high potential has limited effect as long as the solubility of platinum in the acid is reached. When an electrode was subjected to cycling at low potentials , say below 0.7 V, the reduction and deposition of dissolved Pt takes place, resulting in the particle growth. As a result, the low potential hold increases the performance degradation (Figure 5).

In addition, the cycling number of the test has a more pronounced effect, than the duration of the potential hold, on the performance degradation. This is especially true for the initial period of the test, as seen from Figure 6b, while the stern degradation for M07-60 at low cycling numbers was apparently due to the extended test time.

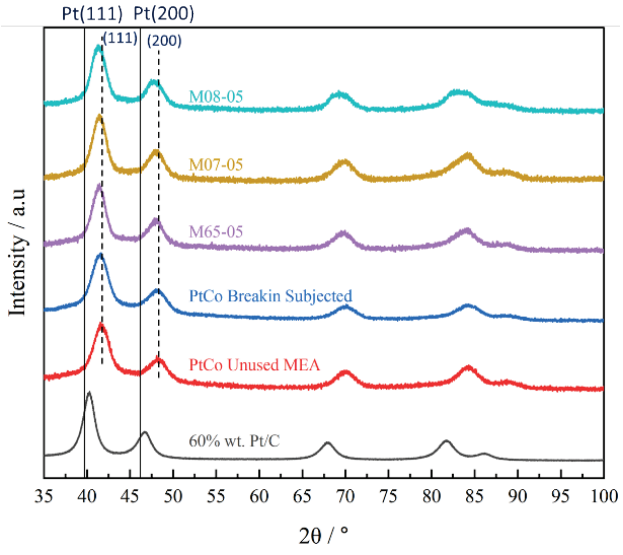

Figure 8. X-ray diffraction patterns of unused $PtCo_x$/C and catalysts collected from fresh MEA as well as EoL MEAs. Fotr comparison, the commercial Pt/C catalyst is also included. The two vertical solid tines

After the cycling test the catalysts were collected from the EoL MEAs and evaluated by X-ray diffraction analysis. The diffractograms are shown in Figure 8. Compared to standard face-centred cubic (fcc) platinum, the dominant (111) and (200) plane peaks (denoted by the two solid lines (PDF(Pt)#00-004-0802) are shifted to higher 2θ values, indicating a substantial lattice contraction due to the formation of the $PtCo_x$ alloys. These are approximately in agreement with d-spacings of $PtCo_x$ alloys reported in the literature.[46] After the potential cycling test, no dealloying of the catalysts was found from the XRD patterns. On the other hand, the particle growth was notable from the particle size analysis, which shows an average particle size of 3.9-4.0 nm for the unused/fresh catalysts to 4.4 nm (M08-05), 4.5 nm (M07-05) and 4.8 nm (M65-05) (See Supporting Information), verifying the discussion above.

Conclusions

A study of the HT-PEMFC performance degradation stressed by potential cycling has been carried out with fixed upper potential limit (0.95 V) but varied low end potentials (from 0.8 to 0.65 V) and hold durations (from 5 to 60 sec). In all tested cells, little degradation of the membrane, in terms of ohmic resistance and open circuit voltage (related to the gas crossover), was observed, apparently due to the overall short time of the fuel cell operation. A significant performance loss was concluded due to the mass transport loss. As limited carbon corrosion was observed, as evidenced by the little change of the catalyst layer thickness by SEM, the increased

mass transport losses can be attributed to the hydrophobicity of the electrodes.

A major catalyst degradation mechanism is the platinum particle growth via the electrochemical Ostwald ripening. The dissolution of Pt and surface oxides during the upper potential hold (0.95 V) is governed by the solubility in the limited amount of doping acid of the electrolyte membrane. The ripening is proposed to be limited by the low-end potentials and the hold duration (from 5 to 60 sec) where the reduction and re-deposition of platinum onto larger particles occur. Further studies by *in situ* determination of the electrochemical surface area of Pt catalysts is desired.

Acknowledgements

This work was financially supported by Energy Technology Development and Demonstration (EUDP) Program (COBRA-Drive, 64018-0118), Denmark.

References

1. B. G. Pollet, S. S. Kocha and I. Staffell, Curr Opin Electrochem, 2019, **16**, 90–95.
2. Y. Wang, D. F. Ruiz Diaz, K. S. Chen, Z. Wang and X. C. Adroher, Materials Today, 2020, **32**, 178–203.
3. J. S. Wainright, J. -T. Wang, D. Weng, R. F. Savinell and M. Litt, J Electrochem Soc, 1995, **142**, L121–L123.
4. D. Aili, J. Yang, K. Jankova, D. Henkensmeier and Q. Li, J Mater Chem A, 2020, **8**, 12854–12886.
5. L. Vilčiauskas, M. E. Tuckerman, G. Bester, S. J. Paddison and K. D. Kreuer, Nat Chem, 2012, **4**, 461–466.
6. Li, Q., He, R., Gao, J.-A., Jensen, J.O. Bjerrum, N. J., J. Electrochem. Soc., 2003, **150,** A1599-A1605
7 N. Seselj, D. Aili, S. Celenk, L. N. Cleemann, H. A. Hjuler, J.O. Jensen, K. Azizi and Q. Li, CSR review, in press (2023)
8 H. Becker, U. Reimer, D. Aili, L. N. Cleemann, J. O. Jensen, W. Lehnert and Q. Li, *J Electrochem Soc*, 2018, **165**, F863–F869.
9 D. Aili, H. Becker, U. Reimer, J. W. Andreasen, L. N. Cleemann, J. O. Jensen, C. Pan, X. Wang, W. Lehnert and Q. Li, *J Electrochem Soc*, 2020, **167**, 134507.
10. T. Søndergaard, L. N. Cleemann, H. Becker, T. Steenberg, H. A. Hjuler, L. Seerup, Q. Li and J. O. Jensen, J Electrochem Soc, 2018, **165**, F3053–F3062.
11. D. Aili, D. Henkensmeier, S. Martin, B. Singh, Y. Hu, J. O. Jensen, L. N. Cleemann and Q. Li, Electrochemical Energy Reviews 2020, **3**, 793–845.
12. Y. Oono, A. Sounai and M. Hori, J Power Sources, 2013, **241**, 87–93.
13. T. Søndergaard, L. N. Cleemann, H. Becker, D. Aili, T. Steenberg, H. A. Hjuler, L. Seerup, Q. Li and J. O. Jensen, J Power Sources, 2017, **342**, 570–578.
14. A. T. Pingitore, F. Huang, G. Qian and B. C. Benicewicz, ACS Appl Energy Mater, 2019, **2**, 1720–1726.
15. F. Ruiz-Zepeda, M. Gatalo, A. Pavlišič, G. Dražić, P. Jovanovič, M. Bele, M. Gaberšček and N. Hodnik, Nano Lett, 2019, **19**, 4919–4927.
16. S. Cherevko, N. Kulyk and K. J. J. Mayrhofer, Nano Energy, 2016, **29**, 275–298.
17. P. Schneider, C. Sadeler, A.-C. Scherzer, N. Zamel and D. Gerteisen, J Electrochem Soc, 2019, **166**, F322–F333.
18. M. Rau, A. Niedergesäß, C. Cremers, S. Alfaro, T. Steenberg and H. A. Hjuler, Fuel Cells, 2016, **16**, 577–583.
19. A. Honji, T. Mori, K. Tamura and Y. Hishinuma, J Electrochem Soc, 1988, **135**, 355–359.
20. M. Prokop, T. Bystron, P. Belsky, O. Tucek, R. Kodym, M. Paidar and K. Bouzek, Electrochim Acta, 2020, **363**, 137165.
21. P. Bindra, S. J. Clouser and E. Yeager, J Electrochem Soc, 1979, **126**, 1631–1632.
22. J. Aragane, H. Urushibata and T. Murahashi, J Appl Electrochem, 1996, **26**, 147–152.
23. M. T. D. Jakobsen, J. O. Jensen, L. N. Cleemann and Q. Li. In High Temperature Polymer Electrolyte Membrane Fuel Cells- Approaches, Status and Perspectives. Eds. Q. Li, D. Aili, H. A. Hjuler and J. O. Jensen. Springer International Publishing Switzerland 2016.
24. F. Maillard, W. O. Silva, L. Castanheira, L. Dubau and F. H. B. Lima, ChemPhysChem, 2019, **20**, 3106–3111.
25. C. A. Reiser, L. Bregoli, T. W. Patterson, J. S. Yi, J. D. Yang, M. L. Perry and T. D. Jarvi, Electrochemical and Solid-State Letters, 2005, **8**, A273.
26. W. Gu, R. N. Carter, P. T. Yu and H. A. Gasteiger, ECS Trans, 2007, **11**, 963–973.
27. J. Büsselmann, M. Rastedt, V. Tullius, K. Yezerska, A. Dyck and P. Wagner, *Int J Hydrogen Energy*, 2019, **4**, 19384–19394.
28. M. Rastedt, F. J. Pinar, N. Pilinski, A. Dyck and P. Wagner, *ECS Trans*, 2016, **75**, 455–469.
29. R. Kerr, H. R. García, M. Rastedt, P. Wagner, S. M. Alfaro, M. T. Romero, C. Terkelsen, T. Steenberg and H. A. Hjuler, *Int J Hydrogen Energy*, 2015, **40**, 16860–16866.
30. Z. Qi and S. Buelte, *J Power Sources*, 2006, **161**, 1126–1132.
31. T. Chinese, F. Ustolin, B. Marmiroli, H. Amenitsch and R. Taccani, *Energies (Basel)*, 2021, **14**, 6737.

32. F. J. Pinar, N. Pilinski and P. Wagner, *AIChE Journal*, 2016, **62**, 217–227.

33. J. Li, L. Yang, Z. Wang, H. Sun and G. Sun, *Int J Hydrogen Energy*, 2021, **46**, 24353–24365.

34. S. Liu, M. Rasinski, Y. Rahim, S. Zhang, K. Wippermann, U. Reimer and W. Lehnert, *J Power Sources*, 2019, **439**, 227090.

35. S. Thomas, S. S. Araya, J. R. Vang, and S. K. Kær, Inter. J. Hydrogen Energy, 2018, **43**, 14691–14700

36. C. Wannek, I. Konradi, J. Mergel, et al. Int. J. Hydrog. Energy 2009, **34**, 9479–9485.

37. M. Boaventura, A. Mendes, Int. J. Hydrog. Energy 201, **35**, 11649–11660.

38. H. Becker, U. Reimer, D. Aili, et al. J. Electrochem. Soc. 2018, **165**, F863–F869.

39. K. Kinoshita, J. Bett, Carbon 1973, **11**, 237-247.

40. H.S. Oh, J.H. Lee, H. Kim, Inter. J. Hydrogen Energy 2012, **37,** 10844-10849

41. Y. Oono, A. Sounai, M. Hori, J Power Sources 2012, **210,** 366-373

42. J. Aragane, T. Murahashi, T. Odaka, J. Electrochem. Soc. 1988, **135**, 844-850

43. J. Aragane, H. Urushibata, T. Murahashi, J Appl Electrochem 1996, **26**, 147-152

44. Y. Chen, K. Azizi, W. Zhang et al., Inter. J. Hydrogen Energy, 2022, **47**, 28615-28625

45. T. Jahnke, G.A. Futter, A. Baricci et al. J. Electrochem. Soc., 2020, **167,** 013523

46. P. Yu, M. Pemberton, P. Plasse, J. Power Sources 2005, **144**, 11-20

Potential Cycling Test of High Temperature PEMFC Based on Acid Doped Polybenzimidazole Membranes

Sanser Clenk,[a] Lars N. Cleemann,[b] Jens Oluf Jensen,[a] and Qingfeng Li*[,a]

a. Department of Energy Storage and Conversion, Technical University of Denmark, Fysikvej B310, 2800 Lyngby, Denmark.

b. Blue World Technologies, Egeskovvej 6C, 3490 Kvistgård, Denmark.

* Correspondance: qfli@dtu.dk

Supporting information

Table S1. Open circuit voltage (OCV) changes from Bol to Eol

		Open circuit voltage (OCV, V)				
MEAs	E/time cycles	BOL	5K	10K	20K	30K (EoL)
M08-05	0,95/5 + 0.8/5	1.007	1.022	1.023	1.022	1.020
M07-05	0,95/5 + 0.7/5	0.959	0.955	0.950	0.947	0.936
M65-05	0,95/5 + 0.65/5	1.013	1.027	1.027	1.028	1.029
M07-30	0.95/30+0.7/30	0.985	0.969	0.961	-	-
M07-60	0.95/30+0.7/60	1.025	1.005	-	-	-

Table S2. High frequency resistance changes from EIS (mOhm cm^2)

		High frequency resistance (HFR, mOhmcm^2)				
MEAs	E/time cycles	BOL	5K	10K	20K	30K
M08-05	0,95/5 + 0.8/5	96.18	96.94	98.60	98.78	98.91
M07-05	0,95/5 + 0.7/5	101.39	104.03	104.93	105.68	106.2
M65-05	0,95/5 + 0.65/5	98.07	n/A	101.09	101.72	102.13
M07-30	0.95/30+0.7/30	102.9	-	-	-	-
M07-60	0.95/30+0.7/60	98.07	-	-	-	-

Table S3. Total resistance after fitting (mOhm cm^2)

MEAs	E/time cycles	Total resistance after fitting (mOhm cm^2)				
		BOL	5K	10K	20K	30K
M08-05	0,95/5 + 0.8/5	205.x	260.x	290.x*	370.x *	340.x *
M07-05	0,95/5 + 0.7/5	207.x	222.x	237.x	253.x	267.x
M65-05	0,95/5 + 0.65/5	182.x	199.x	210.x	223.x	228.x
M07-30	0.95/30+0.7/30	244	269	277	279***	
M07-60	0.95/30+0.7/60	249	443	476**		

** AFTER 10000+ **450** CYCLES =15 HOURS

*** AFTER 5000+ **900** CYCLES = 15 HOURS. THOSE ARE NOT INCLUDED IN THE MANUSCRIPT IT IS ONLY FOR YOUR INFORMATION.

*After a cycling period there was 1 hour of relaxation at 400 mA cm-2 to wet the membrane. However, for the yellow lined parts, the control software only applied 2 minutes of relaxation.

Table S4. Cell voltage at 200 mA cm^{-2} after the iR and mass transport correct for BoL and EoL (30 K cycles)

MEAs	E/time cycles	Cell voltage after correction at 200 mA cm^{-2}				
		BOL	5K	10K	20K	30K
M08-05	0,95/5 + 0.8/5	0.738	0.726	0.725	0.7256	0.721
M07-05	0,95/5 + 0.7/5	0.736	0.723	0.719	0.717	0.714
M65-05	0,95/5 + 0.65/5	0.738	0.719	0.714	0.711	0.708
M07-30	0.95/30+0.7/30					
M07-60	0.95/30+0.7/60					

Table S5 XRD analysis results of catalysts before and after the cycling test

	2-theta	d	Estimated particle size (nm)
40% wt. Pt/C	40.287	3.492	4.07
60% wt. Pt/C	40.304	2.236	5.27
Fresh MEA	41.701	2.164	3.93
After break-in*	41.587	2.17	3.88
0.65	41.453	2.176	4.77
0.7	41.61	2.168	4.47
0.8	41.472	2.177	4.36